UNIVERSITY OF OKLAHOMA

GRADUATE COLLEGE

# DYNAMIC SHEAR RUPTURE ALONG FAULTS: EXPERIMENTS AND SIMULATIONS

A DISSERTATION

SUBMITTED TO THE GRADUATE FACULTY

in partial fulfillment of the requirements for the

Degree of

DOCTOR OF PHILOSOPHY

By

ZONGHU LIAO
Norman, Oklahoma
2013

Downloaded from SHAREOK. Persistent Handle URL: https://hdl.handle.net/11244/7687

DYNAMIC SHEAR RUPTURE ALONG FAULTS: EXPERIMENTS AND SIMULATIONS

A DISSERTATION APPROVED FOR THE
CONOCOPHILLIPS SCHOOL OF GEOLOGY AND GEOPHYSICS

BY

_____
Dr. Ze'ev Reches, Chair

_____
Dr. Kurt J. Marfurt

_____
Dr. G. Randy Keller

_____
Dr. Xingru Wu

_____
Dr. Yehuda Ben-Zion

© Copyright by ZONGHU LIAO 2013
All Rights Reserved.

Dedicated to C.

## Acknowledgements

My dissertation research focuses on earthquake physics, and it was supervised by Dr. Ze'ev Reches, who guided me in all aspects of the study. I am indebted to him for the continuous advice, support, and education of how to become a scientist. I value these years as the best of my life, academically, psychologically, and philosophically with "Weakening first, and then strengthening". Thank Ze'ev.

I have been lucky to meet Dr. Kurt J. Marfurt and have him serving on both my MS and PhD committees. Dr. Marfurt provided me a wonderful opportunity to study oil exploration practices that will help me greatly in my future career. Many thanks the other members of the PhD committee: Dr. Xingru Wu, Dr. G. Randy Keller, Dr. Yehuda Ben-Zion, and Dr. Katie Keranen, for their involvement and support that helped me pursuing the research. Dr. Wu expands my understanding of rock mechanics, especially in the field of petroleum engineering. I learn a lot during Dr. Keller's seminar, and am thankful to his generosity for providing learning opportunity. As to Dr. Ben-Zion, he has fed me with nutritious comments and ideas during conversations from Los Angeles to Salt Lake City, ideas that eventually helped the development of part of the dissertation chapters. Dr. Keranen always made sure that I was well taken care of in her classes and any research conversations with her. I owe you all.

Many thanks to Dr. Roger M. Slatt, Dr. Matthew J. Pranter, and Dr. John D. Pigott for their excellent and inspiring courses and conversations. My friends in the ROGA group, Jefferson Chang, Xiaofeng Chen, and Boneh Yuval, deserve sincere gratitude for so many contributions to my research and for being supporting friends in OU and during the wild trip down to Colorado River Grand Canyon.

I thank Dr. Nadia Lapusta and Dr. Jean-Paul Ampuero, Mr. Junle Jiang, Ms. Yihe Huang and Dr. Shiqing Xu for hosting me in CalTech and USC. They offered many suggestions that greatly improved the current work. A special thanks to Dr. Hiroo Kanamori, who generously discussed my work with me during the AGU 2012 meeting.

I want to convey my sincere thanks to the great team at the ConocoPhillips School of Geology and Geophysics, Dr. R. Douglas Elmore, Mrs. Donna S. Mullins, Mrs. Nancy Leonard, Mrs. Teresa Hackney, Mrs. Adrianne Fox, Mrs. Jocelyn Cook, Mrs. Devon Harr, Mrs. Wei Wang and Mr. Robert Turner for the support during the these years. A special thanks to all the students and many friends in Sarkeys and OU. Some discussion with Xiaochun is helpful. I greatly appreciate the support from the Majiang group and those who witnessed the grand seven pairs: Li Pan, Chen Chen, Shiguang Guo, Tengfei Lin, Li Liu.

Last but not least, my deep thanks to Beishida, and I dedicate this work to my dear family, Dexing Liao, Xiuzhi Cao, Minghua Liao, Yan Chen, Xuezhen Liao, Wenxin Wen, for their sacrifice and everlasting support. I am glad to see the coming of the third generation, Haoxiang Wen, Rachel Liao, and Raynie Liao towards this degree. You are everything of my life.

The present research was financially supported by NSF Geosciences, Equipment and Facilities, award 0732715, NSF, Geosciences awards 0732715 and 1045414, and NEHRP2011 award G11AP20008. Chesapeake Energy and CGG-Veritas provided licenses to their data for Ch. 6.

# Table of Contents

**Acknowledgements** ..... **iv**

**List of Tables** ..... **x**

**List of Figures** ..... **xi**

**Abstract** ..... **xvii**

**Chapter 1: Motivation and Approach** ..... **1**

Research focus and general objectives ..... 1

High-velocity experimental observations ..... 2

Proposed application of the rupture with a new friction law ..... 3

Dissertation organization ..... 5

**Chapter 2: Review of Earthquake Physics Processes** ..... **7**

Introduction ..... 7

Earthquake mechanics ..... 8

Fracturing modes ..... 8

Rupture propagation of fractures and earthquakes ..... 10

Theoretical relations ..... 10

Experimental studies of shear rupture propagation ..... 12

Growth of crack and rupture speed ..... 15

Failure features associated with dynamic rupture ..... 17

Earthquake rupture propagation: observations and concepts ..... 19

Slip distribution during earthquakes ..... 20

Crack mode of earthquake rupture ..... 23

Pulse propagation mode ..... 23

Mechanisms of rock friction during earthquake slip ..... 25
Experimental observations ..... 25
Rate- and state- friction law ..... 27
Slip weakening ..... 29
Foam rubber experiments ..... 31
Frictional strength at high slip-velocity experiments ..... 31
Earthquake-like-slip-event ..... 35
Mechanisms of dynamic weakening ..... 36
Flash melting ..... 37
Pore fluid pressurization ..... 38
Thermal decomposition and degassing ..... 40
Elastohydrodynamic lubrication ..... 41
Nano-powder lubication ..... 42
Slip smoothing ..... 44
Evaluation of experimental friction analysis ..... 45
**Chapter 3: High-Velocity Friction Experiments ..... 49**
Introduction ..... 49
Steady-state experiments at the University of Oklahoma ..... 50
Experiment setup ..... 50
Results 52
Is steady-state data relevant to earthquake slip behavior? ..... 61
Background ..... 61
Testing the impact loading hypothesis ..... 65

Conclusions ..... 68

**Chapter 4: Mechanics of Dynamic Shear Rupture ..... 70**

Formulation of dynamic shear fracture ..... 70

Friction models for rupture simulations ..... 73

Simulation results ..... 75

Slip-weakening model ..... 75

Rate-based models ..... 78

Wrinkle pulse ..... 80

Other pulse mechanisms ..... 82

Evaluations of rupture simulations ..... 83

**Chapter 5: Shear rupture along a fault with an experimentally- determined frictional strength ..... 85**

Introduction ..... 86

Friction models ..... 88

Numerical calculations ..... 91

Results 94

Case 1: Short critical slip distance ..... 95

Case 2: Long critical slip distance ..... 97

Summary of the results ..... 99

Discussion ..... 100

Crack or pulse ..... 100

Discretization and stability ..... 102

Conclusions ..... 102

**Chapter 6: Seismic and experimental analyses of fault structure and associated fractures, Anadarko basin, Oklahoma ..... 104**

Introduction ..... 105

Study area ..... 106

Strike-slip fault in clay experiments ..... 108

Attribute-based Seismic analyses ..... 111

Fault damage zone ..... 113

Conclusions ..... 115

**References ..... 117**

# List of Tables

**Chapter 2:**

Table 1. A summary of friction experiments and related friction model for rupture modeling ..... 46

**Chapter 5:**

Table 1. Stress and friction parameters for two test problems ..... 93

# List of Figures

**Chapter 2:**

Figure 1. Schematic figures showing three modes of cracks: Mode I, mode II, and mode III ..... 9
Figure 2. Stress field for mode III before (dash line) and after (solid line) crack formation. The inset shows the crack geometry (adapted from Kanamori and Brodsky, 2004). ..... 11
Figure 3 a) Sample configuration with strain gages on top of the fault and b) a vertical section shows the locations of semiconductor strain gages (adapted from Ohnaka et al., 1987). ..... 13
Figure 4. Breakdown-zone interpretation of slip-weakening process. (a) The stress field near the crack tip as a function of slip distance. (b) The shear stress on a point as a function of slip velocity. (c) The slip velocity as a function of slip distance. (d) The acceleration as a function of slip distance. (after Ohnaka and Yamashita, 1989). ..... 14
Figure 5 A schematic diagram of the experimental apparatus. a), A normal force, $F_N$, is applied to the base and an increasing shear force, $F_S$, is applied at the trailing edge of the slider until motion ensues in the x direction; b), a laser sheet incident at an angle beyond the critical angle for total internal reflection, is solely transmitted at the net contact points along the rough interface (inset) between the base and slider. Thus, the light intensity transmitted across the interface at any location is proportional to the net contact area at that location. The transmitted light is imaged by a fast camera (see Rubinstein et al. (2004) for details). ..... 16
Figure 6. a) An (x,t) plot of relative intensity measurements of a typical experiment. Hot (cold) colours reflect increased (decreased) net contact area. The four different fronts (labelled within the graph) are clearly evident and present the dynamics of slip before overall sliding (after Rubinstein et al, 2004); b) rupture mode depends on friction coefficient, which roughly indicates three regimes with Slow, Sub-Rayleigh, and Supershear rupture modes (after Ben-David et al., 2010). .. 17
Figure 7. Predicted pattern of off-fault fractures for mode II (conjugate black bars with thick and thin for right-lateral and the left-lateral shear fractures, respectively) for cracks expanding with an elastic medium. Vr is the rupture speed at the time of snapshot and Ψ is the maximum background compressive stress (normalized results, after Xu et al., 2012a). ..... 19
Figure 8 Characteristics of the Landers earthquake. (a) Map view of surficial fault ruptures of the Landers earthquake. (b) Map view of seismicity recorded by the Southern California Seismographic Network from 28 June 1992 to 18 August 1992. (c) Vertical cross section of earthquakes in (b), projected onto the horizontal axes of the maps in (a) and (b). (d) Distribution of dextral surficial slip along the faults. abbreviations: CRn, Camp Rock north; CRs, Camp Rock south; E, Emerson; HVn, Homestead Valley north; HVs, Homestead Valley south; L, Landers; JV, Johnson Valley; BM, Burnt Mountain; and EP, Eureka Peak. (e) Slip distribution along the fault zone calculated from TERRA scope record at Pasadena (Seih, 1993). ..... 20

Figure 9 Schematic diagram showing two modes of rupture: (a) crack-like; (b) pulse-like ..... 22
Figure 10. a) Rupture pattern for the 1995 Kobe earthquake (M=6.8), Japan. California, earthquake determined with inversion of seismic data (Wald and Heaton 1994), b) crack-like propagation by numerical simulation. ..... 23
Figure 11. a) Slip distribution for the M=6.2 1984 Morgan Hill,California, earthquake derived by Hartzell and Heaton (1986) from the inversion of strong motion waveform data. b) Idealized model of a self-healing rupture pulse propagating at velocity Vr in the x direction. The fracture initiates when the stress exceeds the static strength of the fault at the crack tip and then drops to a steady-state friction of a low value. The particle velocity increases fast and then decrease away from the rupture front. Then the friction increases and the strength of the fault return to a high level immediately and the fault heals itself (after Heaton 1990). ..... 24
Figure 12. Schematic of the forcing block (left) and sketch of the bi-axial apparatus (right; Samuelson et al., 2009); b) tri-axial testing machines from the Rock Mechanics Laboratory (U.S. Geological Survey); c) ROGA system sample blocks after experiment (Left, UB: upper block; LB: lower block; EG: ejected gouge) and rotary machine for fault experiment (right; Reches and Lockner, 2010). ..... 27
Figure 13. Coefficient of friction versus displacement at velocities indicated above the experimental curve (after Dieterich, 1979). ..... 29
Figure 14. a) An example of slip weakening by experimental 223; b) The best fit solution (red curve) for slip distance weakening in ten experiments (normalized results). SWG 222, 223, 224 were run at velocity 0.024 m/s; SWG 226-232 were run at 0.072 m/s; $\tau n$ = 1.1 MPa. The solution is $\mu$= 0.2663(±0.1)•exp (-D) +0.4061(±0.15). The constants can be adjusted for specific case. ..... 30
Figure 15. The time histories of particle velocities along the interface for a stick-slip event are shown above. Frames in the left column correspond to the particle velocities in the soft block (low velocity); frames in the right column correspond to the particle velocities in the stiff block (high velocity) (after Anooshehpoor and Brune, 1999). ..... 32
Figure 16. a) Dependence of friction on slip distance for samples slid at 30, 100 mm/s; b) and dependence of steady-state friction on slip velocity (after Di Toro et al., 2004). ..... 33
Figure 17. Granite friction coefficients vs velocity reported by (a) Reches and Lockner (2010) and (b) Kuwano and Hatano (2011). ..... 34
Figure 18. a) The evolution of frictional strength in ELSE experiments (#2782) with respect to slip distance; b) the friction vs velocity for ELSE experiments (after Chang et al., 2012); and (c) the friction vs velocity for the steady-state experiments (after Reches and Lockner, 2010). ..... 36
Figure 19. Friction coefficient vs. sliding velocity on several high rates tests on the same quartzite sample (after Goldsby and Tullis, 2011). CVV: Continuously various velocity; VS: Velocity stepping. ..... 38
Figure 20. The increase in pressure P with temperature at constant density for water under upper crustal conditions. Dashed line shows conditions for a geothermal

gradient of 30 ℃/km and for fluid pressure in an unconfined water column with unite specific gravity (after Lachenbruch, 1980) ..... 40
Figure 21. Monitoring of friction coefficient and $CO_2$ gas emission against time. Sensor 1 is a quick –response sensor for detecting the onset of $CO_2$ emission, and sensor 2 is a slow response sensor for monitoring the amount of emitted $CO_2$. 41
Figure 22 The Stribeck curve schematically shows the variation of the coefficient of friction m with the dimensionless Sommerfeld number, S. In the region labeled "boundary lubrication", solid-solid friction predominates. Between the dashed lines is the mixed regime where solid-solid friction is reduced by the lubrication pressure. In the "hydrodynamic lubrication" region, solid-solid friction is eliminated, and the friction is determined by the viscous stress. (After Brodsky and Kanamori, 2001) ..... 42
Figure 23. The friction coefficient as a function of slip velocity for Sierra White granite at normal stress of 1-7 MPa. Four deformation regimes are identified by the schematic diagrams that indicate the physical conditions in each regime (after Sammis et al, 2011). ..... 43
Figure 24 (a) Experimental fault surface of Kasota dolomite (KD; Minnesota, United States) after run KD-1516 of present study. (b) Roughness-friction relation at micron scale. Shown are room-dry FC and the AFM roughness of KDand Sierra White granite (SWG; California, United States) surfaces (roughness as RMS [root mean square] for 1 μm segments), diamond sample A (Hayward et al., 1992), and Westerly granite from Rhode Island, United States (Byerlee, 1967) (roughness as Ra [mean height differences from a center line]). The relations (solid lines) have the form: FC = a ln roughness) + b, where (a, b) are (0.13, 0.99) for KD-SWG combined, (0.13, 0.67) for diamond A, and (0.16, 0.29) for Westerly granite. (after Chen et al., 2013). ..... 44

**Chapter 3:**

Figure 1. a)The Rotary Shear Apparatus with builder Joel Young. b) The numerical model of the shearing samples for temperature simulation and c) The sample block assembled in the loading frame (after Reches and Lockner (2010)Experimental observations..... 51
Figure 2. Experimental friction-velocity relations in (a) Sierra White granite (after Reches and Lockner, 2010) and (b) Westerly ganite (after Kuwano and Hatano, 2011). ..... 53
Figure 3. Friction-velocity relations in shear experiements of Blue quartzite (a), St. Cloud diorite (b), Fredricksburg syenite (c), and Karoo gabbro (d). Connected lines indicated data from step-velocities experiments. Unconnected dots indicate single velocity experiments.Note velocity-weakening and velocity-strengthening stages (marked by red arrows) in (a)-(c) and no velocity-strengthening in (d).. 55
Figure 4. The selected solution (red curve) for dynamic-weakening of kinetic friction coefficient of SWG for V = 0.0003-0.03m/s by Eureqa. Data for V < 0.003 m/s are from Reches and Lockner (2010) and Kuwano and Hatano (2011). ..... 57

Figure 5. a) The selected solution (red curve) for dynamic-strengthening of SWG for V = 0.03-0.3m/s by Eureqa. Data for V > 0.003 m/s are from Reches and Lockner (2010) and Kuwano and Hatano (2011). ..... 58
Figure 6. a) The best fit solution (red curve) for slip distance weakening in ten experiments. SWG 222, 223, 224 were run at velocity 0.024 m/s; SWG 226-232 were run at 0.072 m/s; $\sigma_N$ = 1.1 MPa. The solution is $\mu$= 0.2663(±0.1) exp (-D) +0.4061(±0.15). The constants can be adjusted for specific case. ..... 59
Figure 7. WEST model simulation and experimental results for a) SWG 531, $\sigma_N$ = 1.1 MPa, and b) SWG 616, $\sigma_N$ =5.0 MPa. Friction coefficient is shown for a full-velocity continuously in sliding distance together with a best fit modeling result. ..... 61
Figure 8. Friction, acceleration and velocity during experimental attempt to simulate fault behavior during high-velocity slip. a). Stick-slip event along an experimental granite fault; b). Frictional strength vs slip velocity on the same granite samples under impact loading and c) steady-state loading; note the fundamental difference for earthquake velocity > 0.1 m/s. d). Strength and velocity during the slip acceleration stage along a gabbro sample (Niemeijer et al., 2010). ..... 64
Figure 9. Frictional strength and slip velocity on a fault patch of granite under three different loading modes. (a) Three loading modes for earthquake experiments, including steady-state, quake loading, and ramp loading. (b) Friction-velocity relations under aforementioned loading modes; note re-strengthening at ~0.02 m/s after weakening in steady-state, fast weakening at V>0.1 m/s with friction drop of 0.1 to 0.3 per 0.1 m/s for SWG samples under quake loading, and the strengthening of syenite at 0.5-1.0 m/s at ramp loading. ..... 66
Figure 10. Earthquake models during fault slipping at a specific point on the fault. (A) Shear stress and slip velocity and slip during a pulse-like earthquake event (adapted from Heaton, 1990). (B) The evolution of frictional stress, slip velocity, and displacement in ELSE experiments under quake loading. (C) New friction law generalized from experiments, ELSE-based Slip and linear slip weakening (LSW). ..... 68

**Chapter 4:**

Figure 1. A schematic presentation of a) planar rupture in Cartesian coordinates and b) anti-plane rupture. ..... 71
Figure 2. A flow-chart shows the procedures for solving rupture propagation by spectral method. ..... 73
Figure 3. a) In the slip weakening friction model, friction drops from $\mu_s$ to $\mu_k$ instantly after a slip $D_C$; b) Change in friction due to a sudden increase in sliding velocity in rate- and state- friction model. ..... 74
Figure 4. Profile of stress setting for simulated antiplane fault. The green dash line represents an approximately defined stress above which slip will initiate. ..... 77

Figure 5. a) Slip velocity vs slip time at 6 km away from the nucleation center in the antiplane direction; b) cohesive zone along antiplane (adapted from Day and Dalguer, 2005). ..... 78
Figure 6. a) Relative position of the radiation damping line $\tau = \tau_0^b - \frac{\mu}{2c}V$ and the steady-state friction $\tau = \tau_{ss}(V)$ for the understressing condition, $\tau_0^b \leq \tau_{pulse}$. b) Relative position for $\tau_0^b > \tau_{pulse}$ (after Zheng and Rice, 1997). ..... 79
Figure 7. a) Example of time histories of slip velocity and b) normal traction at x=6 on the fault from the regularized calculation of self-sustaining wrinkle pulse (after Andrews and Ben-Zion, 1997). Dots mark phase arrivals of faster P, slower P, faster S, slower S from an arbitrary chosen point within the initiation region; time histories of particle slip velocity observed in c) slow medium and d) fast medium for a stick-slip event in the foam rubber experiments (after Anooshehpoor and Brune, 1999). ..... 81

**Chapter 5:**

Figure 1. The evolution of frictional strength in ELSE experiments with respect to slip distance a) experiment #711; b) experiment #712; c) experiment #742; d) the selected experiment #733 for rupture simulation with a black dash fitting line. Note all are in log plot. ..... 89
Figure 2. A schematic presentation of linear slip-weakening (black) and ELSE-based Slip model (red). ..... 90
Figure 3. A homogeneous and infinite elastic medium for anti-plane faulting (after Ampuero et al., 2000) and a 2-D fault model for testing spontaneous rupture propagation with monitoring points marked as red stars. ..... 94
Figure 4. Time histories of slip velocity, slip distance, and shear stress at the fault plane (6.0 km). Solutions are for SBIEM by a) Linear Slip-weakening and b) ELSE-based Slip, case 1. ..... 96
Figure 5. Time series of slip velocities at various points at the fault plane. a), Solutions by Linear Slip-weakening compared with b) ELSE-based Slip results, case 1.. 96
Figure 6. Time histories of slip velocity, slip distance, and shear stress at the fault plane (6.0 km). Solutions are for SBIEM by a) Linear Slip-weakening and b)ELSE-based Slip, case 2. ..... 98
Figure 7. Time series of slip velocities at various points at the fault plane. a), Solutions by linear slip-weakening compared with b) ELSE-based Slip results, case 2.... 99
Figure 8. Slip histories of a) peak slip distance and b) peak velocity along a fault under a uniform setting with short critical slip distance for Linear Slip-weakening; Slip histories of c) peak slip distance and d) peak velocity along a fault under a uniform setting with short critical slip distance for ELSE-based Slip. ..... 101

**Chapter 6:**

Figure 1. Geological map and study area (red star) within the Anadarko basin, Oklahoma (Credit: OGS). ..... 107

Figure 2. (a)Time structure of top Woodford co-rendered with horizon slice through coherence. Red lines represent major faults. (b)Vertical slice along AA' through the seismic amplitude volume showing a north-south trending fault zone (in red lines). ..... 108
Figure 3. Mechanical basis for faults/folds/fractures associated with a major strike-slip fault: (a) R and R' faults that developed as Coulomb slip planes; (b) folds along the strike slip fault, which could also be (c) the potential thrust faults; (d) Normal faults developed from Riedel shears (adapted from Naylor et al., 1996; and Reches 1988). ..... 109
Figure 4. a) Vertical view of the strike-slip clay experiment. Circles on the undeformed model provide a means of mapping movement and strain. (b) Photograph after 12 min demonstrating initial Riedel shear faults on the top during right-lateral strike-slip with digitized image. (c) Photograph at 24 min demonstrating fault Riedel shears (black lines), splay shears (green lines) and P shears (red lines) on top of the deformed clay. ..... 110
Figure 5. (a) Photograph from experiment and (b) A display of coherence co-rendered with seismic amplitude on the top Woodford Shale. Black lines indicate potential Riedel faults, the green lines splay faults and red lines P shears. ..... 112
Figure 6. Dip-azimuth map of the top Woodford. Note the bands of same color within dashed line boxes, indicating same dip-azimuth, revealing potential fracture zones that I interpret to be P shear zones with compressed folds. ..... 113
Figure 7. (a) A schematic diagram showing an anticline folds with fracture systems (after Sterns, 1978) and (b) Curvature on the top of Woodford Shale. Areas with strong curvature (brighter red and blue) correspond to strong flexures, folds, and densely fractures. ..... 114
Figure 8. Schematic representation of the fault model that explains (a) heterogeneous stress field over a scaling region (Dieterich and Smith, 2009; Powers and Jordan, 2010) and (b) damage zone. (c) The illustration of damage zone from the coherence slices perpendicular to the north-south strike slip fault. The zone of high coherence values above background coherence indicates the damage zone. ..... 115

# Abstract

Earthquakes are events of unstable shear rupture that propagate along fault-zones in the crust. Earthquake rupture processes have been the focus of experimental analyses and numerical simulations, yet many details are still enigmatic (Ch.1). One of the central questions of earthquake physics is the intensity of fault dynamic weakening, and the realistic simulation of earthquake rupture at in-situ conditions. My main focus in rupture simulations is the dependence of the simulations on the friction law of the fault interface that is based on experimental observations.

In recent years, experimental results of high-velocity shear provided a promising opportunity to implement experimental friction model to dynamic rupturing on earthquake scale. The main issues related to earthquake processes at seismic and aseismic rates are reviewed in Ch. 2, with emphasis on friction strength data from rotary shear apparatus and its potential application to the rupture numerical simulation.

Then, I present my experimental results for siliceous igneous rocks at high slip velocity (up to ~1.0 m/s) and at normal stress of ~1-7MPa. The evaluation of these and others steady-state experiments suggests that this data may be irrelevant to fault friction during earthquakes, simply because earthquake slip does not occur as a steady-state process. To avoid the limitation of controlled velocity in steady-state experiments, I tested the earthquake-like loading experiments. It presents the fast-accelerated and slow-decelerated behavior of slip velocity, and the weakening-strengthening of shear stress, which better captures the character of earthquake rupture models and comply with the earthquake models (Ch. 3).

Based on the formulations of dynamic shear rupturing for earthquake simulations (Ch. 4), I simulate the dynamic shear rupture along a vertical, strike-slip fault in an elastic half-space (Ch. 5). The fault has the frictional strength properties that were determined experimentally on Sierra White granite samples at impact loading. The friction-distance relations of these experiments were used to form an empirical slip-dependent friction model, referred to as 'Earthquake-like-slip-even' ELSE-model (Chang et al., 2012). For the dynamic rupture simulation, I used a 2D spectral boundary integral element method that was designed for anti-plane (mode III) shear fracture problems (Ampuero, 2002). To facilitate comparison of ELSE-model results with published models, the calculations were conducted for a crust with mechanical properties and stress state of Version 3 benchmark of SCEC (Harris et al., 2004).

The rupture simulations with a fault of ELSE-model friction law revealed a few significant properties: (1) Rupture propagation in a slip-pulse style in which the slip velocity with the cessation of slip behind the slip-pulse; (2) Systematic decrease of slip distance away from the nucleation zone; and (3) Spontaneous arrest of the dynamic rupture without requiring artificial insertion of a barrier. These properties suggest a rupture of a self-healing slip-pulse mode in contrast to the rupture model calculated for linear slip-weakening friction (Rojas et al., 2008) that generates a crack-like rupture with no spontaneous arrest. I deduce that the slip-pulse in our simulation results from the fast recovery of shear strength as observed in ELSE experiments, and argue that incorporating this experimental-based friction model to rupture modeling produces realistic propagation of earthquake rupture.

Finally, I also investigate a structural problem of identification of a strike-slip fault at the subsurface (Ch. 6). I used wet clay experiments to analyze the evolution of the associated structures with a strike-slip fault in the Woodford Shale unit, Anadarko basin, Oklahoma. The geometry of Riedel shears, splay shears and P shears from the lab are used as proxies for the 20 mi long, north-south strike slip fault in the 3D seismic survey volume. I applied three seismic attributes (coherence, dip-azimuth, and curvature) to illuminate the fault system, and identify two types of associated structures with high intensity of fractures for potential horizontal drilling: (1) fault systems that are similar to the clay experiments that were revealed in coherence maps; and (2) anticlinal folds that were detected in curvature maps. I conclude that combining attribute analysis and experimental observations strengthens the identification of this striking slip fault-zone in Woodford Shale.

# Chapter 1: Motivation and Approach

## Research focus and general objectives

Earthquakes are events of unstable shear rupture that propagate along fault-zones in the crust. Earthquake rupture processes have been the focus of experimental analyses and numerical simulations, yet many details are still enigmatic. Probably the most outstanding open questions are related to the character of dynamic weakening of frictional faults and the realistic simulation of earthquake rupture at in-situ conditions. My main focus in rupture simulations is the dependence of the simulations on the friction law of the fault interface that is usually based on experimental observations that are relevant to field conditions.

Agreat effort has been initiated by Geubelle and Rice (1995) and widely followed by, e.g., Lapusta et al. (2000), Ampuero et al. (2002), and Xu and Ben-Zion (2012ab) to address different problems of the fault rupture simulation. However, there are significant practical difficulties in determining the friction on faults during earthquake. For example, slip-weakening models do not incorporate slip-rate effects and other state variables, and the empirical Rate- and State- Friction (RSF, Dieterich, 1979) law was derived for slip velocities and displacements that are orders of magnitudes below typical large earthquakes.

As the frictional slip resistance is critical for the understanding of earthquake rupture, it becomes a challenge to analyze the experimental friction evolution at earthquake conditions, and to implement high-velocity results to aseismic dynamic rupturing. My main objective is to set up a new friction model using the experimental

observations of dynamic friction that were conducted in rotary shear apparatus at slip velocity (up to 1.0 m/s) and normal stresses of up to 30 MPa (Reches and Lockner, 2010; Chang et al., 2012). I intend to apply this experimentally-based friction model to simulate the earthquake dynamic rupture that were more relevant to the real earthquake in terms of slip acceleration, velocity and distance etc. To determine a physically friction law at seismic rates is the main emphasis of the present work.

## High-velocity experimental observations

The high-velocity and long slip-distance experiments conducted on rotary shear machines provide a promising friction data for simulators to study fault rupture with frictions at seismic conditions (Beeler et al., 1994; Tsutsumi and Shimamoto, 1997; Di Toro et al., 2004; Reches and Lockner, 2010; Goldsby and Tullis, 2011). The main motivation of this work is to apply experimental based friction law at seismic rates to the rupture simulation. It is proposed to use realistic parameters of friction laws based on high-velocity experiments.

Most rock friction experiments are conducted at controlled-velocity mode during which the slip velocity is controlled by the apparatus at a constant or stepping values. However, this approach does not necessarily capture the full complexity of earthquake rupture. Sone and Shimamoto (2009) sheared an experimental fault by loading it with acceleration and deceleration stages and indicated the necessary to incorporate (e.g., velocity-controlled) physical processes activated at seismic slip rates (Sone and Shimamoto, 2009; Fukuyama and Mizoguchi, 2009; Goldsby and Tullis, 2011; Niemeijer et al., 2011; Tisato et al., 2012). This point was emphasize by Chang et

al. (2012) who compared the friction-velocity relations of the granite loaded either at constant/stepping velocity or at flywheel impacting, finite energy experiments. The impact loading induces high strain-rates of ~104 s-1 that significantly increase rock brittleness and rheology, and by doing so would activate weakening mechanisms that do no operate at classical loading experiment. As both sets of experiments were conducted on the same rock samples, the dissimilarity is attributed solely to the different loading mode, as already suggested by Sone and Shimamoto (2009).

I think that the earthquake-like loading experiments (Sone and Shimamoto, 2009; Fukuyama and Mizoguchi, 2010; Yuan and Prakash, 2008; Chang et al., 2012) better capture the character of earthquake rupture process than constant velocity experiments. This type of friction results is likely to provide realistic earthquake rupture.

**Proposed application of the rupture with a new friction law**

In this dissertation, I present simulations of the dynamic shear rupture along a vertical, strike-slip fault in an elastic half-space. The fault has the frictional strength properties which were determined in high-velocity, rotary shear apparatus. The experimental fault was made of Sierra-White granite blocks that were abruptly loaded by a massive flywheel. This loading style is assumed to simulate the loading of a fault patch during an earthquake, and it was termed Earthquake-Like-Slip Event (ELSE) by Chang et al. (2012). These experiments revealed systematic alteration between slip-weakening and slip-strengthening. Based on slip distances, Chang et al. (2012) considered their experimental results as proxies of fault-patch behavior during earthquakes of magnitude M = 4 - 8. I used the friction-distance relations of these

experiments to form an empirical slip-dependent friction model, referred to as ELSE-model.

For the dynamic rupture simulation, I use the program of Ampuero et al. (2002) (2D spectral boundary integral elements) that was designed for anti-plane (mode III) shear fracture problems. To facilitate comparison with published simulations, the calculations were conducted for a crust with mechanical properties and stress state of Version 3 benchmark of SCEC (Harris et al., 2004). The preliminary rupture calculations with a fault of ELSE-model friction law revealed a few significant features: (1) Rupture propagation in a slip-pulse style with the cessation of slip velocity behind the slip-pulse; (2) Systematic decrease of slip distance away from the nucleation zone; and (3) Spontaneous arrest of the dynamic rupture without requiring artificial insertion of a barrier. These features together suggest a rupture of a self-healing slip-pulse mode. These results reveal differences from the rupture model calculated for a fault with linear slip-weakening friction (Rojas et al., 2008) that generates a crack-like rupture that does not arrest spontaneously. I deduce that the slip-pulse in our simulation results from the fast recovery of shear strength as observed in ELSE experiments, and argue that incorporating this experimentally-based friction model to rupture modeling produces realistic propagation style of earthquake rupture.

In the implementation of the new friction law into earthquake numeric simulations, I use a simplified SPBIEM method (Rice, 2005; Fukuyama and Madariaga, 1995; Fukuyama and Mizoguchi, 2009). The simulation results suggest a rupture of a self-healing slip-pulse mode with taking neither contrast materials nor heterogeneous stress settings. The slip-pulse in the present simulations results from the fast recovery of

shear strength as observed in ELSE experiments. I finally argue that incorporating this experimentally-based friction model to rupture modeling produces realistic propagation style of earthquake rupture.

## Dissertation organization

This dissertation consists of six chapters that will be revised for publication. As preparation for publication, I try to keep the chapters independent of each other, and I apologize to the reader for some repetitions between the chapters.

**Chapter 1** presents the motivation and main objective for the study and also the framework of this dissertation.

**Chapter 2** reviews earthquake processes. This chapter introduces the theory of earthquake mechanics and experimental studies. I also select to cover the essential question of dynamic weakening during earthquakes. Many of the major mechanisms for explaining dynamic weakening have been briefed corresponding to the experimental observations.

**Chapter 3** provides our recent experimental studies that revealed profound fault weakening during high velocity slip. Steady-state experiments with silica-rich igneous rocks (granite, syenite and diorite) revealed dynamic-weakening under slip velocities below ~ 0.03 m/s and dynamic-strengthening as the slip velocity approaches seismic values of ~ 1 m/s. I analyze then the problems of steady-state frictions when applying them as proxies of earthquake to the rupture modeling. I think that the earthquake-like loading experiments capture the character of earthquake rupture models.

**Chapter 4** outline the formulations of dynamic rupturing that were derived and used for earthquake simulations, the previous results, and the present approach.

**Chapter 5** presents the rupture modeling using a constitutive law that fits the observations of earthquake-like loading experiments. The emphasis is to use frictions laws that were derived at high-velocity experiments and particularly, the ELSE experiments (Chapter 3).The rupture simulations revealed a few significant features.

**Chapter 6** studies secondary structures of a strike-slip fault in subsurface. I used wet clay experiments to identify and analyze the evolution of the associated structures with a strike slip fault, and applied three attributes (coherence, dip-azimuth, and curvature) to illuminate the fault system, and identified two types of associated structures with high intensity of fractures for potential horizontal drilling in oil industry.

# Chapter 2:

# Review of Earthquake Physics Processes

## Introduction

Earthquakes are events of unstable shear rupture that propagate along fault-zones in the crust. Earthquake rupture processes have been the focus of many theoretical studies, numerical simulations, and experimental analyses, yet many details are still enigmatic. Probably the most outstanding open questions are related to the character of dynamic weakening of frictional faults and the realistic simulation of earthquake rupture at in-situ conditions. In the present study, I attempt to contribute to these questions.

The framework of dynamic rupture simulation has been well constructed and continuously improved using numerical methods including finite difference, finite element and boundary integral methods (Andrews, 1976; Geubelle and Rice, 1995; Morrissey and Geubelle, 1997; Huang and Ampuero, 2011; Ampuero and Ben-Zion, 2008; Xu and Ben-Zion, 2013). In most cases, the rupture simulations implement the fault modeling on an interface that is governed by a friction law. Since it is impossible to determine fault friction with seismological methods (Kanamori and Brodsky, 2004), the study of fault friction and earthquake weakening has been usually addressed with laboratory experiments (Dieterich, 1979) and theoretical models (Ohnaka and Yamashita, 1989). In recent years, many new experimental results of fault friction were obtained by advancing from early low velocity to high shearing velocity (Di Toro et al., 2004; Reches and Lockner, 2010; Kuwano and Hatano, 2011), and these results provide

important opportunity and challenge to analyze the experimental friction evolution at aseismic rates, and to implement high-velocity friction model to dynamic rupturing on earthquake scale. In this introduction, I review the main issues related to shear rupture modeling at seismic and aseismic rates. I highlight the friction strength data from rotary shear apparatus and its potential application to the rupture numerical simulation.

## Earthquake mechanics

### *Fracturing modes*

Faulting and fracturing in the Earth may be viewed in terms of the basic fracture modes and their equivalent dislocations. Each mode (Fig. 1) is represented by a planar discontinuity in an elastic solid that terminates at a line which is the fracture tip (Lawn, 1993). The three basic modes differ in the sense of displacement with respect to the planar surfaces and the tip line. The displacements are defined in two-dimensions.

*Mode I*: the tensile mode in which the fracture surfaces move apart normal the surface either by extension (e.g., joints) or by internal pressure (e.g., dikes). This mode displays symmetric stress distribution respecting to the planes perpendicular to the y-z axis;

*Mode II (equivalent geometry of edge dislocation)*: the in-plane shear mode in which the two fracture sides slide with respect to each other in x direction (Fig. 1b), normal to the tip line. The deformation is symmetric with respect to the plane perpendicular to the z axial and anti-symmetric to the plane perpendicular to the y axis;

*Mode III (equivalent geometry of screw dislocation)*: the anti-plane shear mode in which the two fracture sides slide with respect to each other in the y direction (Fig.

1c), parallel to the tip line. The fracture surfaces slide over each other in the z direction under shear forces parallel to the crack front, with deformations skew-symmetric respecting to the plane perpendicular to the z-y axis.

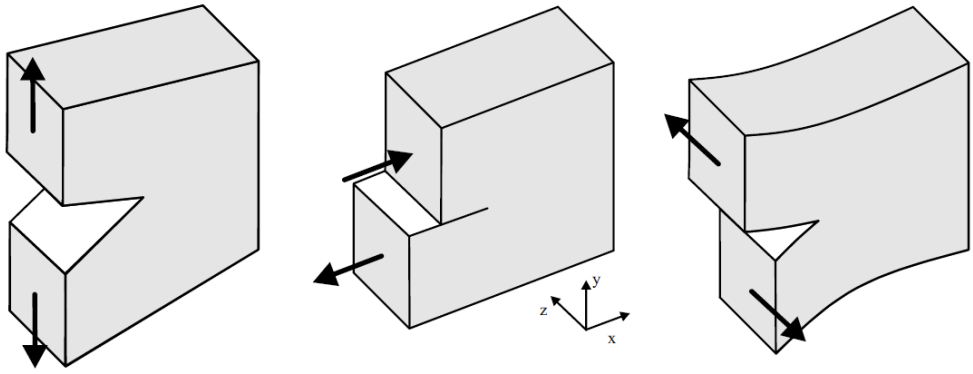


**Figure 1. Schematic figures showing three modes of cracks: Mode I, mode II, and mode III**

In application to natural cases in the field, dilational structures like joints and dikes are assumed to be represented by mode I, and very long strike-slip faults by mode III. Normal and reverse faults may be represented as mode II fractures. However, as these modes were defined in 2D geometry, slip along a natural fault that is embedded in a three-dimensional space requires a combination of a set at least four of mode II and mode III cases. In this proposed work, I focus on the mode III fracture.

## Rupture propagation of fractures and earthquakes

*Theoretical relations*

Considering a mode III fault in homogeneous medium with half-length, a, the theoretical stress distribution, $\sigma_{zy}$, (Fig. 2) along the plane is (after Kanamori and Brodsky, 2004),

$$\sigma_{zy} = (\sigma_0 - \sigma_f)\frac{x}{\sqrt{(x^2 - a^2)}} + \sigma_f, x \geq a$$

In which the $\sigma_0$ is the uniform initial shear stress, $\sigma_f$ is the steady friction after weakening. $(\sigma_0 - \sigma_f)$ is the stress drop during unstable slip along a fault of 2a length. The displacement within the slip surface, $w$, is,

$$w = \left(\frac{\sigma_0 - \sigma_f}{\mu}\right)\sqrt{a^2 - x^2}\,, x \leq a$$

In which $\mu$ is the shear modulus determined by the rock properties. If considering a small distance $\varepsilon$ from the crack tip, $x = a + \varepsilon$, $\sigma_{zy}$ is expressed as,

$$\sigma_{zy} = \frac{K}{\sqrt{2\pi}}\frac{1}{\sqrt{\varepsilon}} + \sigma_f$$

In which K is stress intensity factor and detailed expressions for different modes of crack could refer to Dmowska and Rice (1986). In this case, it is determined as,

$$K = \sqrt{2\pi a}(\sigma_0 - \sigma_f)$$

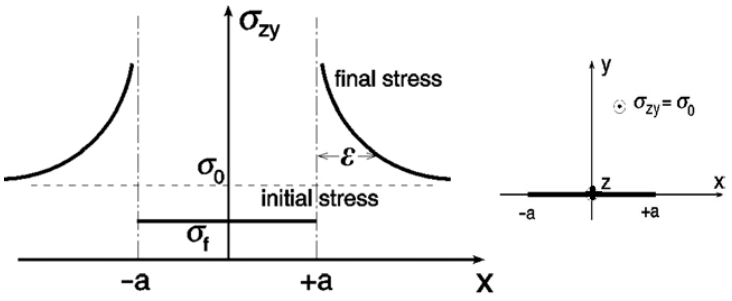


**Figure 2. Stress field for mode III before (dash line) and after (solid line) crack formation. The inset shows the crack geometry (adapted from Kanamori and Brodsky, 2004).**

The energy release per unit slip distance, D, which is average offset of the fault, in z direction is expressed as,

$$\Delta W = \frac{(\sigma_0 + \sigma_f)D \cdot 2a}{2} = \Delta W_0 + \sigma_f D \cdot 2a$$

In which $\Delta W_0$is the portion of the strain energy change that is not dissipated in the friction process, which is expressed as,

$$\Delta W_0 = \frac{(\sigma_0 - \sigma_f)D \cdot 2a}{2} = \frac{\pi a^2(\sigma_0 - \sigma_f)^2}{2\mu}$$

Griffith theory sought the configuration that minimizes the total energy of the system. In case of static crack, the static energy release rate or crack extension force, $G^*$, is termed as (Kanamori and Brodsky, 2004),

$$G^* = \frac{\pi a(\sigma_0 - \sigma_f)^2}{2\mu} = \frac{K^2}{2\mu}$$

Note that this crack extension force is not a constant, and $G^*$ increases as the crack propagates. G* defines the surface energy that is necessary to create the new crack surface as $\gamma$, and consider each side of the crack, the energy release rate is equal to twice the surface energy of the material crack tip,

$$G^* = G_c^* = 2\gamma$$

If $G^*$ exceeds $G_c^*$ , where $G_c^*$ is termed as critical specific fracture energy. In case of seismic faulting, the Griffith theory often generalize $\gamma$ to includes the damaged zone. In case of $G^* > G_c^*$, there is extra inertial energy, $E_R$,

$$E_R = G^* - G_c^* > 0$$

Thus the rupture mode turns from steady to dynamic propagation and the $E_R$ appears as a means for dissipating the excess energy, e.g., radiated seismic waves (Lawn, 1993; Kanamori and Brodsky, 2004). The dynamic energy release rate could be noted as G. Both $G^*$ and K are the important parameters for crack simulations, where $G^*$ of mode III slightly differs from those of mode I and II. The attentions of this review focus on the dynamic propagation only.

## *Experimental studies of shear rupture propagation*

### *Ohnaka experiments and model of breakdown zone*

Ohnaka et al. (1986, 1987) performed experiments on 28cm×28cm×5cm Tsukaba granite (Fig. 3a) which were cut along the diagonal to produce stick-slip failure along the precut fault. The fault length is ~40 cm that is 8-10 times larger than the observed size of the local breakdown zone. The fault is long enough compared with the breakdown zone to observe the behaviors around the crack tip. The sample has a shear wave velocity of 2.9 km/s, rigidity of $2\times10^4$ MPa, and a Poisson's ratio of 0.12. Dynamic shear stresses were derived from the strains monitored along the fault (Fig. 3b). Shear stress, slip displacement, slip velocity and slip acceleration near the crack tip were carefully analyzed to characterize the breakdown processes.

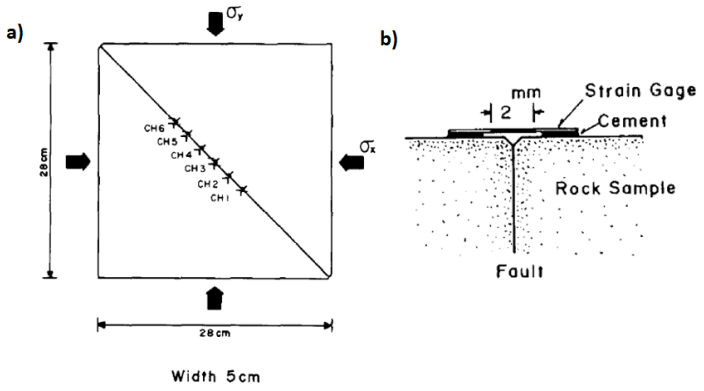


**Figure 3 a) Sample configuration with strain gages on top of the fault and b) a vertical section shows the locations of semiconductor strain gages (adapted from Ohnaka et al., 1987).**

Fig. 4 presents the Ohnaka's model of dynamic propagating during unstable slip failure. The representative constitutive relations have been generalized near the propagating tip of the slipping zone during the breakdown process. The temporal evolution of the shear stress (Fig. 4a) at a point shows that the shear stress decreases from its peak value to a dynamic friction stress level along with increasing slip distance (Ohnaka and Yamashita, 1989). This is a typical slip weakening commonly observed during different types of fault, both in seismic observations and experimental studies (Heaton, 1990; Ohnaka et al., 1986). The shear stress is also presented as a relation with slip velocity (Fig. 4b). It shows an initial hardening effect when the velocity increase, and then there is a dynamic weakening until the velocity reaches the peak value. The stress is maintained at a low value lever when the slip velocity decelerated. The slip failure occurs through the whole velocity phase of acceleration-deceleration. Overall, Fig. 4 present the basic features that have been observed and confirmed near the dynamically propagating tip of the slipping zone. Several parameters remain in the focus of earthquake studies, primarily the critical slip distance (Dc), pattern of the slip

velocity (Fig. 4cd; loading status), and breakdown zone size (Xc) defined as the distance along rupture plane from the crack tip to the point with dynamic low friction.

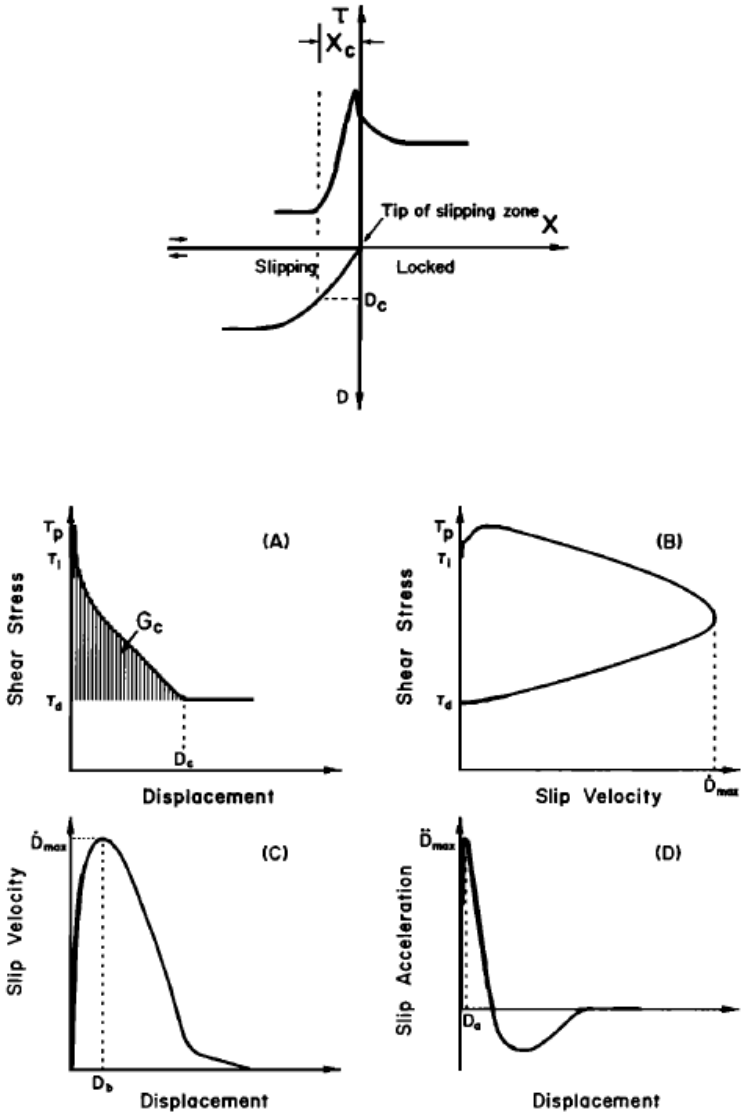


**Figure 4. Breakdown-zone interpretation of slip-weakening process. (a) The stress field near the crack tip as a function of slip distance. (b) The shear stress on a point as a function of slip velocity. (c) The slip velocity as a function of slip distance. (d) The acceleration as a function of slip distance. (after Ohnaka and Yamashita, 1989).**

*Growth of crack and rupture speed*

The rupture fronts of a shear failure are fast, on the order of shear wave velocity, and difficult to be detected. Rubinstein et al. (2004) succeeded to monitor this dynamics of the rupture between two acrylic (PMMA) blocks separated by a rough interface, which is considered as an analog of a fault plane (Fig. 5). This system allows the light to pass through the interface only at the actual points of contact while all other points are without light transmitted. The light intensity is thus related to the local contact area, which is used to visualize instantaneous changes of area and further study of the friction. During the experiment, a force, $F_N$, is applied normal to the interface and a shear force, $F_S$, is applied at the trailing edge in a direction parallel to the interface plane. The slip initiates by increasing $F_S$ at a constant rate.

The monitoring of the change in the contact area is used to reflect the different rupture fronts and derive the rupture speed. Fig. 6a presents the four types of fronts in a typical experiment for $F_N$ = 3,470 N, shear loading rate 40 N/s and driving velocity of 10 μm/s before the onset of slip and a 100,000 frames /s sampling rate. These rapid processes, e.g, Sub-Rayleigh and Slow, record the rupture history of the two blocks experimentally. The rupture speed, V, could be related to the dynamic energy release rate, G, given by

$$G = G^* g(V)$$

Where g(V) is a universal function of V and there are different expressions for modes of rupture. It suggests that the Slow fronts nearly always occur in the isolated events or partially in the combination with rapid mode. More systematically, Fig. 6b presents the rupture velocity in relation with friction coefficient (Ben-David et al.,

2010). These results demonstrate the complexity of dynamic frictional behavior of fault instability. Jay Finberg and his group show that a even slower front is the dominant mechanism for the rupture interface. Only when either of the slower two fronts traverses the entire interface, the sliding of the blocks occurs.

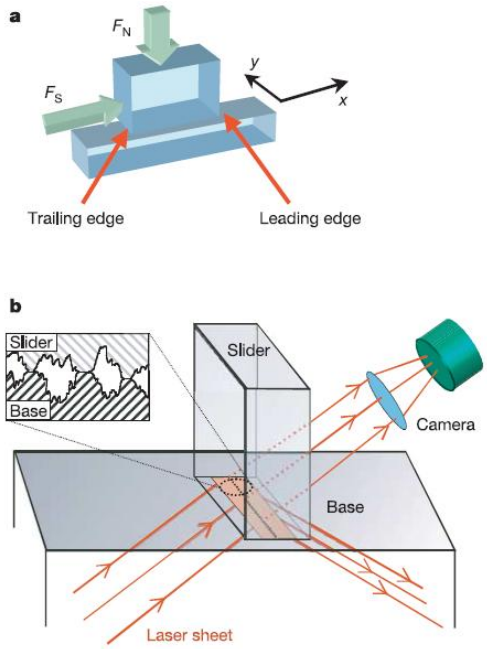


**Figure 5 A schematic diagram of the experimental apparatus. a), A normal force, $F_N$, is applied to the base and an increasing shear force, $F_S$, is applied at the trailing edge of the slider until motion ensues in the x direction; b), a laser sheet incident at an angle beyond the critical angle for total internal reflection, is solely transmitted at the net contact points along the rough interface (inset) between the base and slider. Thus, the light intensity transmitted across the interface at any location is proportional to the net contact area at that location. The transmitted light is imaged by a fast camera (see Rubinstein et al. (2004) for details).**

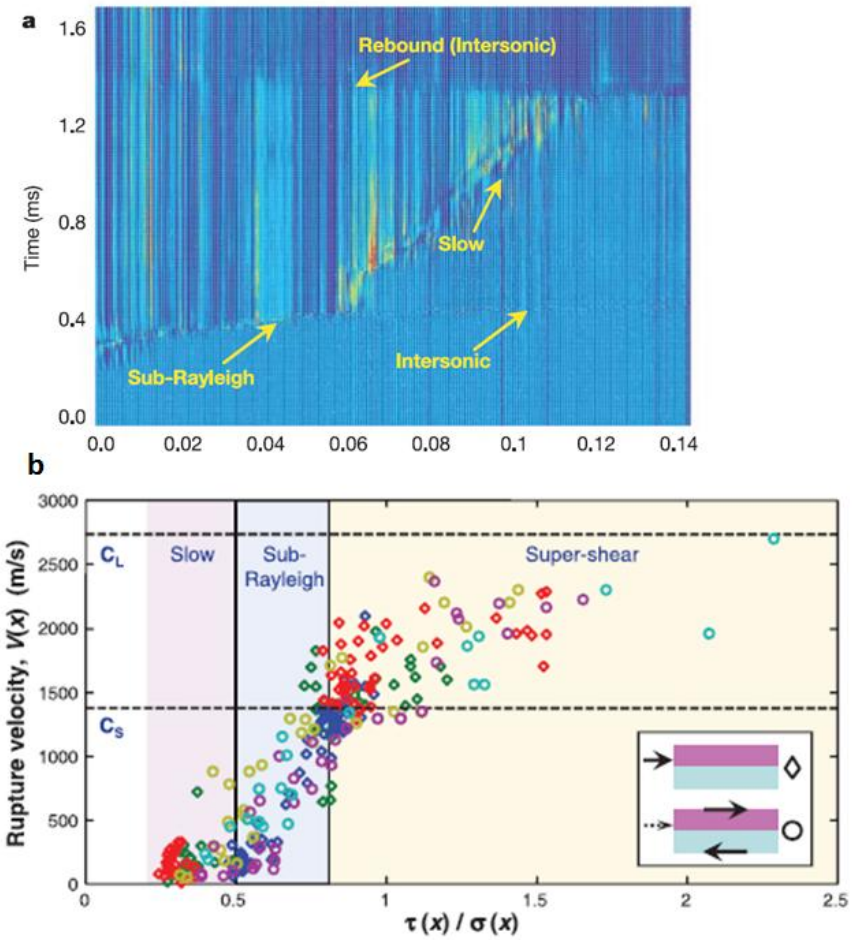


**Figure 6. a) An (x,t) plot of relative intensity measurements of a typical experiment. Hot (cold) colours reflect increased (decreased) net contact area. The four different fronts (labelled within the graph) are clearly evident and present the dynamics of slip before overall sliding (after Rubinstein et al, 2004); b) rupture mode depends on friction coefficient, which roughly indicates three regimes with Slow, Sub-Rayleigh, and Supershear rupture modes (after Ben-David et al., 2010).**

### Failure features associated with dynamic rupture

The dynamic propagation problem could become even more complex than above (Fig. 7) because of the complex stress field and the strain energy flux near the crack tip. In faults observed in the fields, the damage zones are usually found with significant fracture density over meter to hundreds of meter (Chester, 2004). Thus the characterization of the damage zone could provide important information for

understanding the stress conditions in addition to the fault core. Reches and Dewers (2005) calculated the deformation conditions of dynamic shear fracture propagating close to the Rayleigh wave velocity. The mechanism of rock pulverization with the tip region is proposed by an analytical solution for an in-plane propagating (Freund, 1990). Rice et al. (2005) constructed rupture models by balancing the stress intensity factor over a finite zone near the tip. The results examined the properties of Mohr-Coulomb criterion and found a number of dependence for spatial pattern of yielding zone, including rupture speed, ratio of residual to peak stress, patch size and mode of the rupture.

The systematic characterization of yielding zones around propagating faults generated spontaneously by dynamic rupture were done by Xu et al. (2012ab) and Xu and Ben-Zion (2013). The works consider the friction responses, initial stress conditions, rock properties, geometries of the fault, and even material contrast. Fig. 7 presents simulation results of potential off-fault secondary fractures under rupture modes of crack and pulse. The initial settings and parameter inputs are the same for the modeling and the results shows that the yielding zones is larger for the crack than for the slip as consequence of the different stress concentrations. The study shows that the location and shape of the off-yielding zones depend strongly on the angle of the background maximum compressive stress fields (Xu et al., 2012a). During the propagation, the rate of energy components (including off-fault dissipation) linearly increases for crack with time, and reaching a steady level for pulse-mode of ruptures.

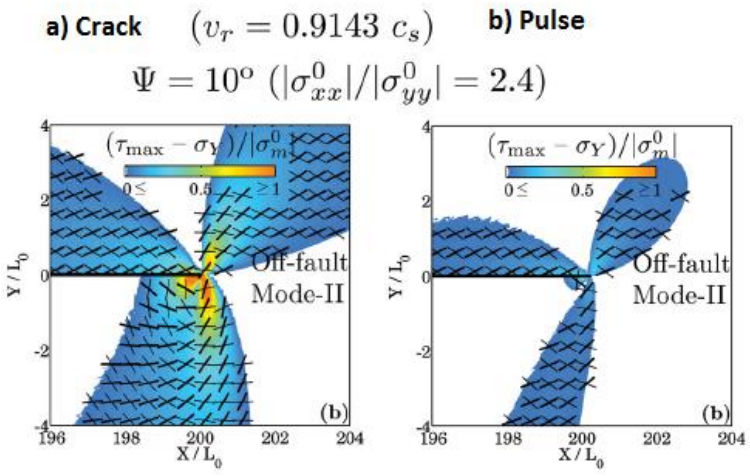


**Figure 7. Predicted pattern of off-fault fractures for mode II (conjugate black bars with thick and thin for right-lateral and the left-lateral shear fractures, respectively) for cracks expanding with an elastic medium. Vr is the rupture speed at the time of snapshot and Ψ is the maximum background compressive stress (normalized results, after Xu et al., 2012a).**

## Earthquake rupture propagation: observations and concepts

Earthquake rupture is usually studied by inverting the observed seismic waveforms while assuming a friction model for the fault-zone. The wave amplitude and frequencies generated by the sudden slip on a fault plane are assumed to be related to the slip physical properties, and the surrounding medium is usually assumed as elastic. The slip distribution on the fault-zone is one of the main objectives for waveforms inversion. In general, there are two end members of rupture pattern: the crack and the pulse modes.

*Slip distribution during earthquakes*

The M=7.3, 1992 Landers earthquake is one of the better documented earthquake in terms of slip pattern. During this event, the slip occurred along a few segments of a

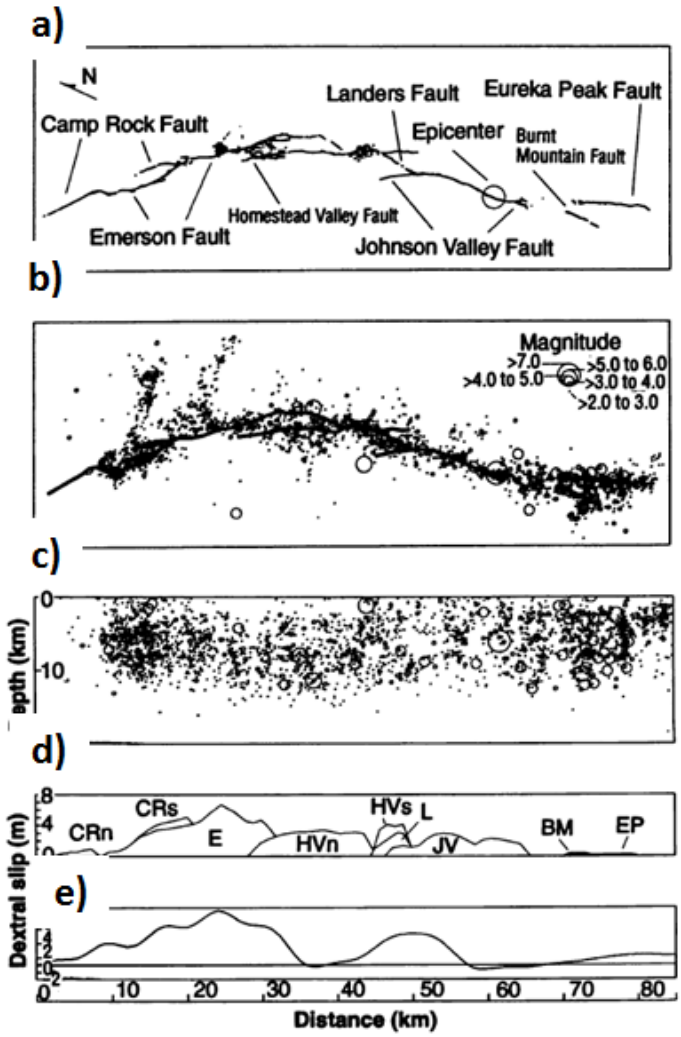


**Figure 8 Characteristics of the Landers earthquake. (a) Map view of surficial fault ruptures of the Landers earthquake. (b) Map view of seismicity recorded by the Southern California Seismographic Network from 28 June 1992 to 18 August 1992. (c) Vertical cross section of earthquakes in (b), projected onto the horizontal axes of the maps in (a) and (b). (d) Distribution of dextral surficial slip along the faults. abbreviations: CRn, Camp Rock north; CRs, Camp Rock south; E, Emerson; HVn, Homestead Valley north; HVs, Homestead Valley south; L, Landers; JV, Johnson Valley; BM, Burnt Mountain; and EP, Eureka Peak. (e) Slip distribution along the fault zone calculated from TERRA scope record at Pasadena (Seih, 1993).**

large fault of 80-km length of the southern end of the eastern California shear zone, which is part of the greater San Andreas system. Fig. 8a is an overview of the en echelon geometry of the principal right-lateral ruptures of the earthquake. The aftershock seismic activity (28/06/1992-18/08/1992) is shown in a map view (Fig. 8) and a vertical cross section normal to the faults (Fig. 8). The measured surface slip is plotted in Figs. 8de. The hypocenter was on Johnson Valley (JV) fault, and the Homeland, Johnson Valley and Lander segments slipped more than 2 meter local offsets while central Homeland and Emerson segments displayed offsets > 3 m. The maximum observed slip of ~6 m was along Emerson fault.

The observed slip values show highest values along each segment that systematically decreases towards both ends of the segment (Fig. 8d). This slip distribution fits, in general, the theoretical prediction of elliptical slip distribution, *w*, along a mode II fracture of length 2*a* for a constant stress drop, as shown by equation (Pollard and Segall, 1987),

$$w = \left(\frac{\sigma_0 - \sigma_f}{\mu}\right)\sqrt{a^2 - x^2}\,, x \leq a$$

However, this surface slip distribution that is the finite earthquake slip and provide no information on the slip and velocity evolution during the rupture. It is generally viewed that the finite slip distribution can evolve in two end members known as the crack mode and pulse mode (Fig. 9).

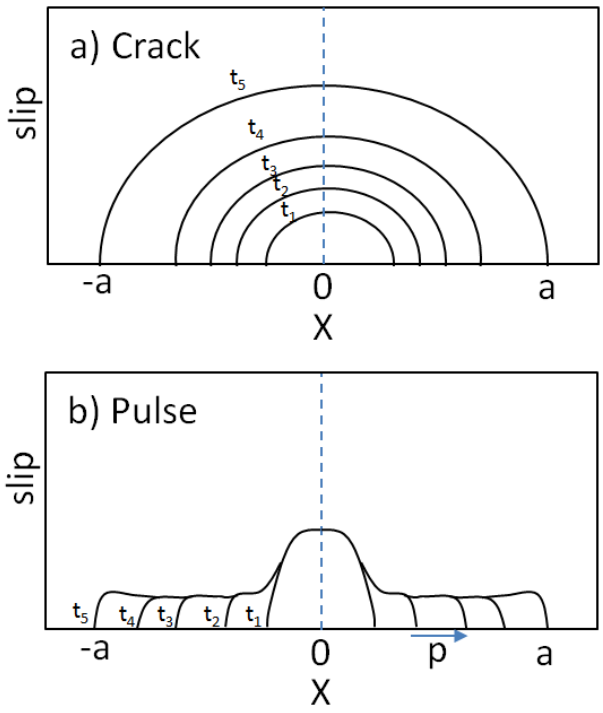


**Figure 9 Schematic diagram showing two modes of rupture: (a) crack-like; (b) pulse-like**

Fig. 9 displays time steps in idealized crack and pulse modes that lead to the same finite slip, but in different evolution. In the crack model, slipping initiates along the entire finite earthquake length, 2a, and increases simultaneously at all points, x. The time cumulative slip at point x is $w_x$ predicted by the above equation. In the pulse mode, slip initiates at a given location and propagates as a pulse of length 2p along the entire fault, where $2p < 2a$. While moving, the pulse generates at every point, x, slip magnitude $w_x$, that equals the finite slip expected by the above equation. The recognition of the earthquake slip evolution is not revealed by the finite slip distribution, and can be determined by the inversion of strong ground motion (Heaton, 1990) as discussed below.

*Crack mode of earthquake rupture*

In a typical crack-like rupture pattern on the fault, the slip at a given point continues until the rupture has stopped propagation. This type of rupture is the most observed type of earthquake propagation and well accepted, although many realistic slip distributions are too complex to be explained with a simple model. As shown for the 1995 Kobe (M=6.8), Japan (Fig. 10, Zhao and Negishi, 1998), I hypothesis it a crack-like propagation, with high heterogeneous in space and time. Since it is hard to determine the crack nature of the propagation, crack-like is more commonly studied by numerical simulation. Fig. 10b presents a rupture propagation pattern with non-stopping slip.

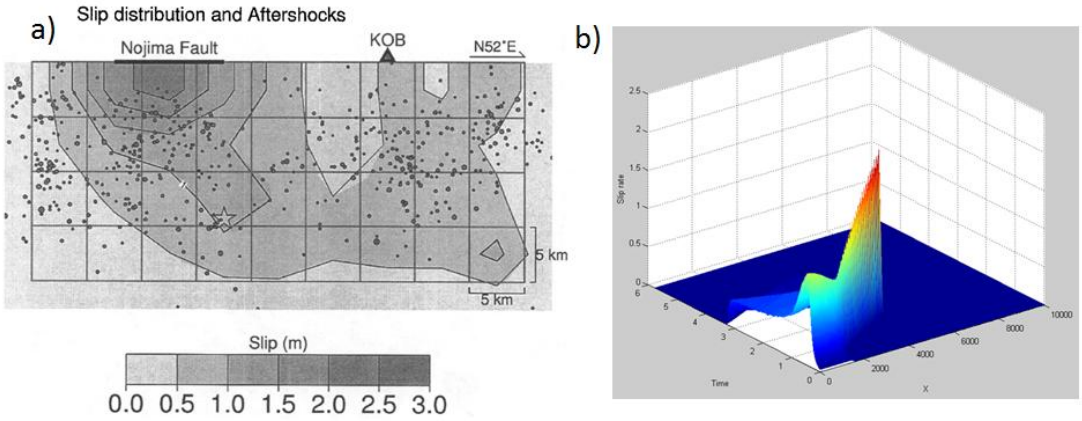


**Figure 10. a) Rupture pattern for the 1995 Kobe earthquake (M=6.8), Japan. California, earthquake determined with inversion of seismic data (Wald and Heaton 1994), b) crack-like propagation by numerical simulation.**

*Pulse propagation mode*

Heaton (1990) inspected the velocity and slip evolution deduced from strong ground motion data of earthquakes, and found that the observations are inconsistent with standard crack-like rupture model. He found that the duration of slip (rise-time) at

a given point can be significantly shorter than the time required for rupturing the entire fault surface. The local slip duration, which is the rise-time, is about 15% of the total slip duration of a crack-like rupture. For example, Fig. 11a presents the slip distribution of M=6.2, earthquake in Morgan Hill, derived by modeling of strong motion and teleseismic waveform data. The rise-time of the slip is 0.3 s compared with the total rupture time of 3 s. More events, e.g., Michoacan of Mexico (M=8.1), Imperial Valley

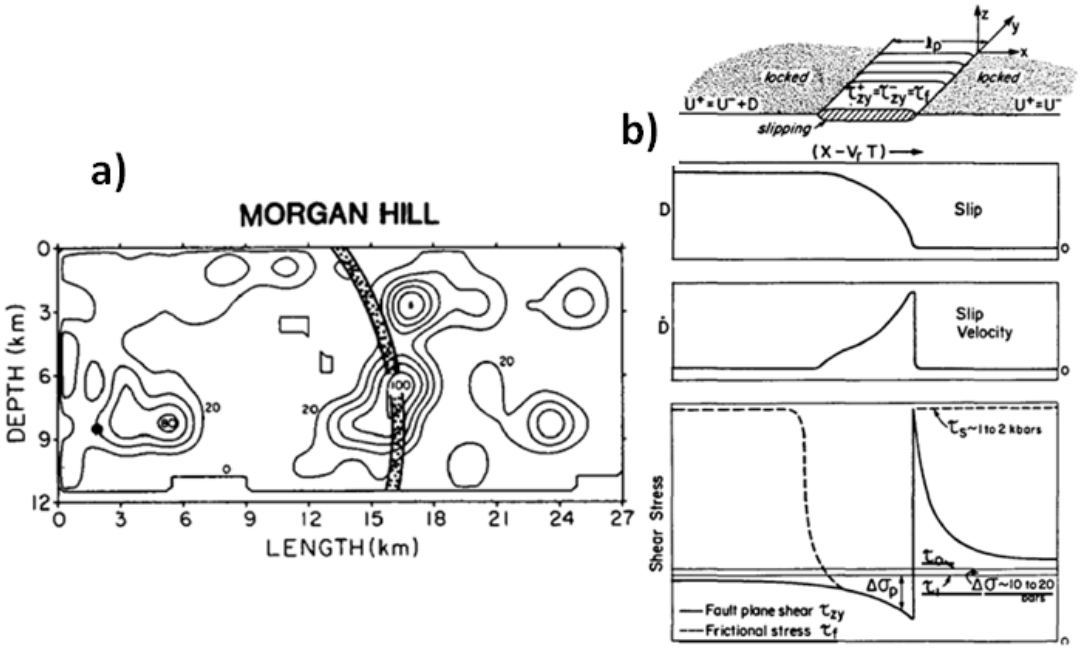


**Figure 11. a) Slip distribution for the M=6.2 1984 Morgan Hill,California, earthquake derived by Hartzell and Heaton (1986) from the inversion of strong motion waveform data. b) Idealized model of a self-healing rupture pulse propagating at velocity Vr in the x direction. The fracture initiates when the stress exceeds the static strength of the fault at the crack tip and then drops to a steady-state friction of a low value. The particle velocity increases fast and then decrease away from the rupture front. Then the friction increases and the strength of the fault return to a high level immediately and the fault heals itself (after Heaton 1990).**

(M=6.5), and North Palm Springs (M=6.0) show similar features. This rupture dynamics led to the mechanism of **self-healing slip-pulse** (Fig. 11b). Self-healing pulse

is a dynamic fault friction that decreases with increasing slip velocity, and then recovers to initial value as the slip velocity decreases, thus producing slip-pulse at the rupture front with ceased slip behind.

## Mechanisms of rock friction during earthquake slip

### *Experimental observations*

Fault frictional resistance is a central component for the understanding of earthquakes. A very weak fault-zone, e.g., the creeping zone of the San Andreas fault (Lockner et al., 2011), which is strain-hardening or of constant strength, will not produce the unstable slip of an earthquake. Such faults will creep (Moore and Rymer, 2010) and move in slow-earthquake that do not radiate seismic waves, or with reduced seismic radiation like the 1960 Chile earthquake, which was considered as a "thermal event" (Brodsky and Kanamori, 2001). The main source for the mechanisms of fault strength evolution (weakening, strengthening, and healing) is from rock friction experiments, and thus significant effort has been devoted to the experimental analysis of dynamic weakening and earthquake instability. Several experimental configurations have been used, each with its advantages and disadvantages: bi-axial direct shear (Fig. 12a; Dieterich, 1979; Samuelson et al, 2009), tri-axial confined shear (Fig. 12b; Lockner and Beeler, 2003), and rotary shear apparatus (Fig. 12c; Tsutsumi and Shimamoto, 1997; Goldsby and Tullis, 2002; Di Toro et al., 2004; Reches and Lockner, 2010). The direct shear apparatus allows high normal stress and controlled pore water pressure (up to ~200 MPa) with limited slip velocity (up to 0.01 m/s) and limited slip distance (~10 mm) (Shimamoto and Logan, 1984). Although the results from direct

shear are consistent with many seismological observations (Marone, 1998), the slip velocities and displacements in these experiments are orders of magnitude smaller than typical earthquakes (0.1-10 m/s and up to 5 m, respectively).

In order to study high velocity and long slip distance, experiments have been conducted in rotary shear machines in the past 20 years (Fig. 12c; Reches and Lockner, 2010; Di Toro et al., 2010). This system is restricted to relatively low normal stress (<10 MPa), and complicated usage of pore fluid pressure.

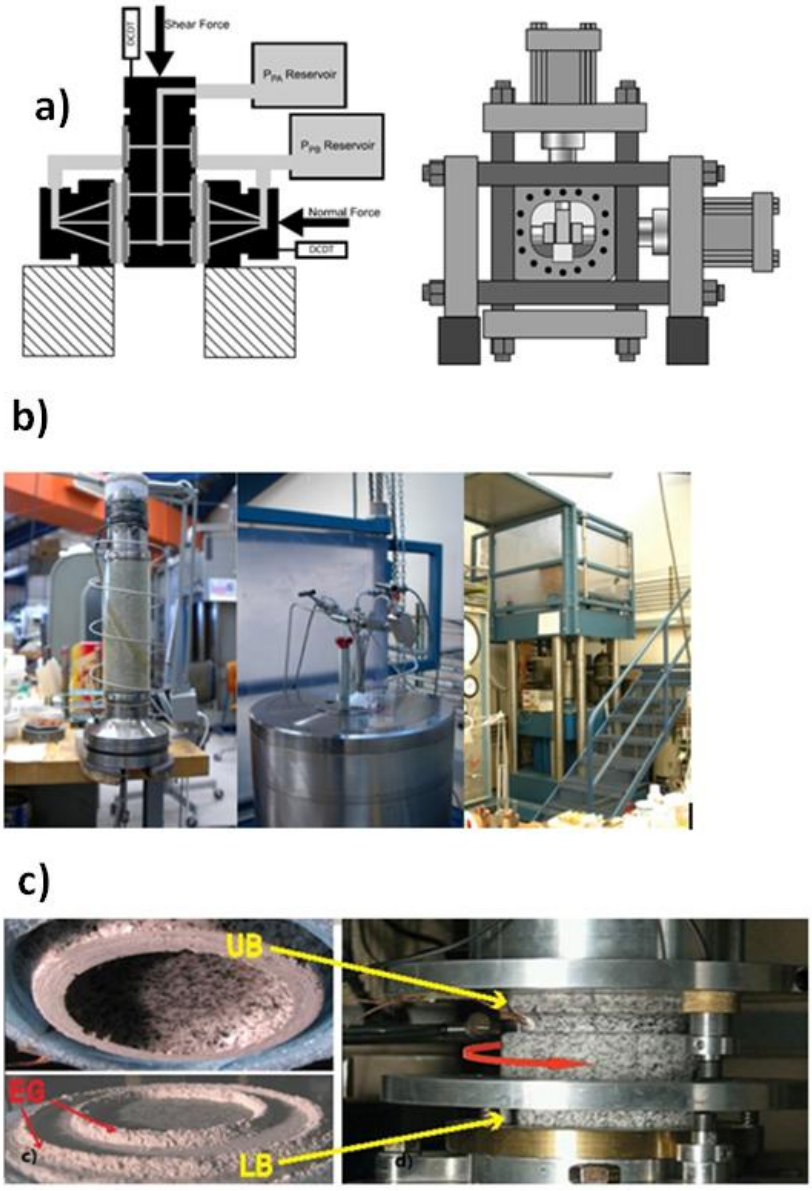


**Figure 12. Schematic of the forcing block (left) and sketch of the bi-axial apparatus (right; Samuelson et al., 2009); b) tri-axial testing machines from the Rock Mechanics Laboratory (U.S. Geological Survey); c) ROGA system sample blocks after experiment (Left, UB: upper block; LB: lower block; EG: ejected gouge) and rotary machine for fault experiment (right; Reches and Lockner, 2010).**

*Rate- and state- friction law*

The rate- and state friction (RSF), which was derived from experimental observations, is the most commonly used friction model in earthquake analyses

(Lapusta et al., 2000). Dieterich (1979) measured rock friction in biaxial shear apparatus as function of slip velocity and hold time. As an example, I present his results of a granodiorite experimental fault sheared at $\sigma_n$ = 6 MPa and steady velocities that in the range of 0.01μm/s to 1.0 mm/s. Fig. 13 shows two of these experiments with the coefficient of friction versus slip displacement in experiments of steps of rising slip velocity. Dieterich found that as: 1) Dc is at scale of micro-meter scale, ~20 μm in Fig. 13; 2) Dc is attributed to the height and size of contacting asperities or the particle size and thickness in a gouge layer; 3) Slip weakening and consequently the potential for unstable slip occur during each rising slip velocity; 4) The transient increase in friction when slip velocity increases.

Dieterich and his followers (Ruina, 1983; Dieterich 1992) derived Constitutive relations that incorporated the slip distance, slip velocity, and hold time. It is argued that this friction style is applicable to earthquake instability. The model was further improved by integrating a state variable as will be discussed in later section.

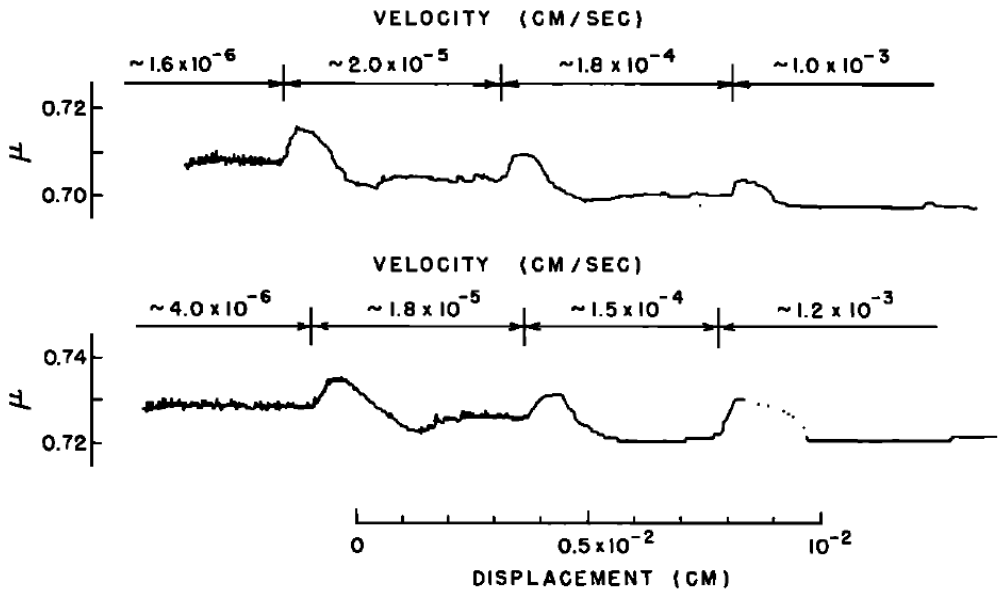


**Figure 13. Coefficient of friction versus displacement at velocities indicated above the experimental curve (after Dieterich, 1979).**

*Slip weakening*

Another widely used friction model is linear slip-weakening model. Here it is assumed that during breakdown process of the fault zone, the friction drops from a static value at the initiation of slip to a kinetic value after the slip displacement exceeds a critical value (Ida, 1972; Andrews, 1976; Day and Dalguer, 2005). The slip weakening was widely observed in slow and high velocity experiments. (Dieterich, 1979; Ohnaka and Yamashita, 1989; Tsutsumi and Shimamoto, 1997; Di Toro et al., 2004; Reches and Lockner, 2010; Goldsby and Tullis, 2011). For example, a typical experiment in OU laboratory, a Sierra White granite sample was loaded at normal stress of 5.0 MPa and slipped at constant velocity of 0.025 m/s (Fig. 14a). The initial, static friction coefficient of 0.69 dropped to ~0.4 after slip of ~2.6 m. This slip-weakening at constant slip velocity is commonly observed in experiments, e.g., Liao and Reches (2012) determined the scale of Dc to be meter by implementing 10 Sierra White granite

experiments (Fig. 14b). Niejmeyer et al (2010) showed that the weakening distance, Dc, strongly depends on the normal stress.

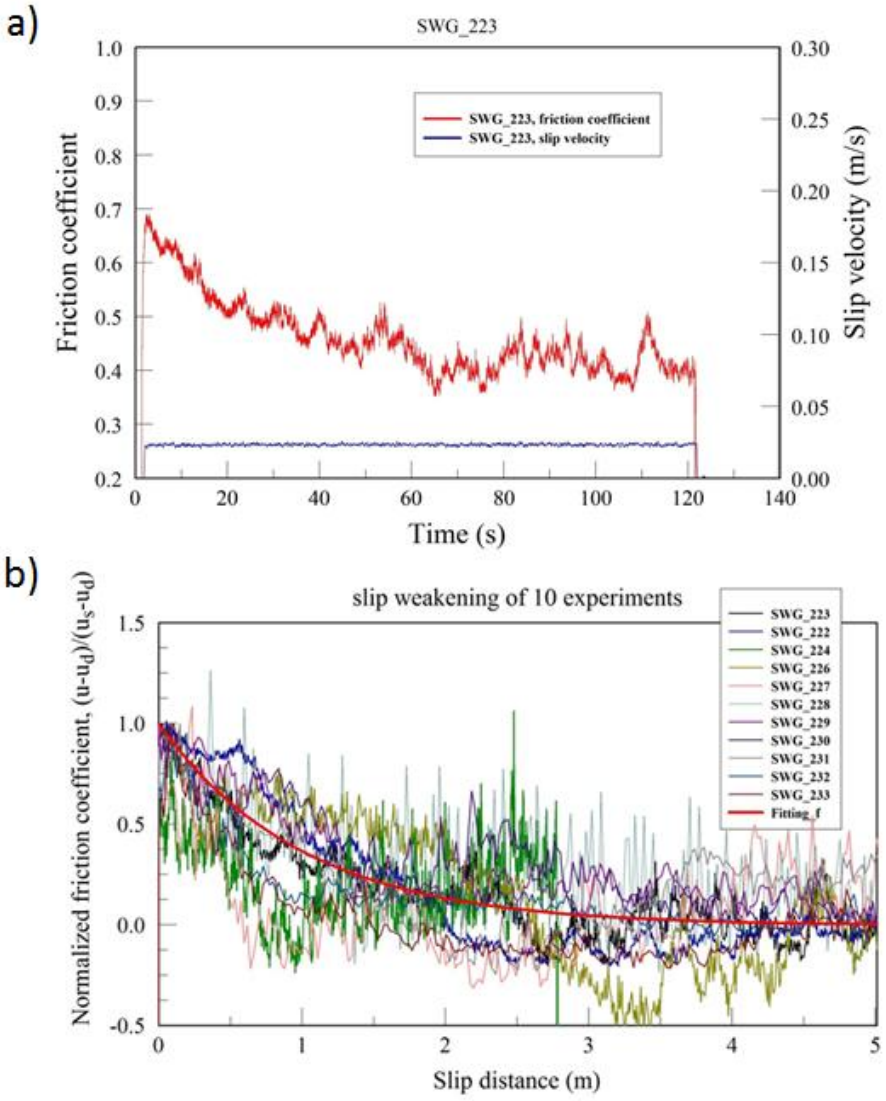


**Figure 14. a) An example of slip weakening by experimental 223; b) The best fit solution (red curve) for slip distance weakening in ten experiments (normalized results). SWG 222, 223, 224 were run at velocity 0.024 m/s; SWG 226-232 were run at 0.072 m/s; $\tau n$ = 1.1 MPa. The solution is $\mu$= 0.2663(±0.1)•exp (-D) +0.4061(±0.15). The constants can be adjusted for specific case.**

*Foam rubber experiments*

Blocks of foam rubber have been used to verify the existence of self-sustaining wrinkle-like Weertman velocity pulses between two dissimilar bodies (Weertman, 1980; Andrews and Ben-Zion, 1997). During the experiments (Anooshehpoor and Brune, 1999), the slip along large (a few meters) blocks were monitored with multiple sensors. The FN and FP curves in Fig. 10 correspond to the fault-normal and fault-parallel slip velocity components, respectively. These plots show multiple events of stick-slip motion along with velocity time histories that fit the winkle-like pulses predicted by Andrews and Ben-Zion (1997). Results also indicate that the particle motion is much larger in the direction perpendicular to the fault in the slower medium.

*Frictional strength at high slip-velocity experiments*

The frictional strength at high slip velocities (0.1-2 m/s) and for long slip displacements (0-10 m), which are typical to seismic events, were achieved by rotary apparatuses the experiments on simulated faults at aseismic rates (Tsutsumi and shimamoto, 1997; Di Toro et al., 2004; Han et al., 2007; Reches and Lockner, 2010; Di Toro et al., 2011). Here I present a few examples of the results. Di Toro et al. (2004) conducted rapid-slip shear along annular surfaces of experimental faults samples of Arkansas novaculite (quarzitze). The ring-shaped samples have inner and outer radii of 22.2 and 26.97 mm, and were pre-roughened and slide under normal stress of 5 MPa allowing a slip of up to 4.7 m and a velocity of up to 0.1 m/s. The results indicate: 1) Friction coefficient drops from 0.8 to 0.2 with slip weakening distance of Dc=~1 m at 0.03m/s and 0.1 m/s; 2) Temporary reduction and strength recovery (Fig. 16a) that are

attributed to possible flash melting; 3) strong velocity dependence dynamic weakening (Fig. 16b).

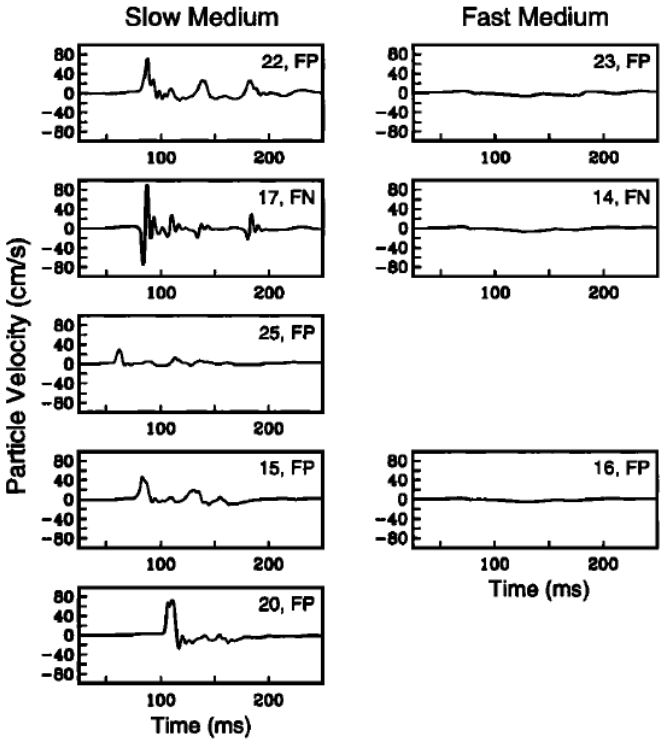


**Figure 15. The time histories of particle velocities along the interface for a stick-slip event are shown above. Frames in the left column correspond to the particle velocities in the soft block (low velocity); frames in the right column correspond to the particle velocities in the stiff block (high velocity) (after Anooshehpoor and Brune, 1999).**

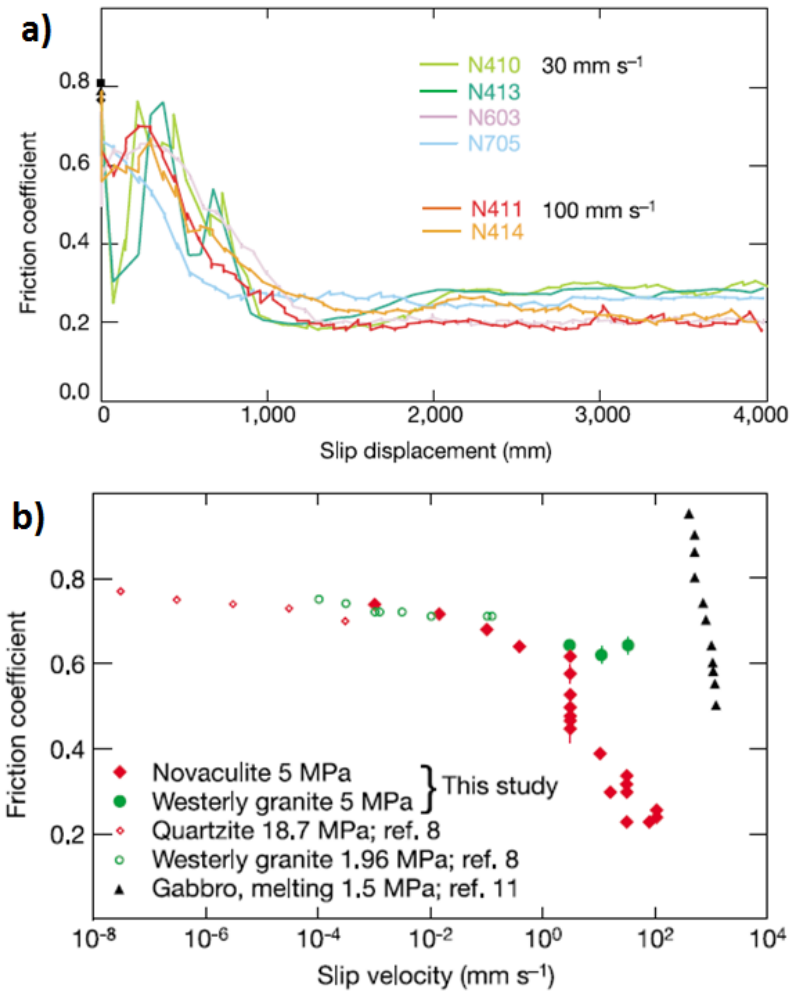


**Figure 16. a) Dependence of friction on slip distance for samples slid at 30, 100 mm/s; b) and dependence of steady-state friction on slip velocity (after Di Toro et al., 2004).**

Reches and Lockner (2010) and Liao and Reches (2012) analyzed the results of experimental faults made of siliceous rock including granite, syenite, diorite, and quartzite and sheared on 'Rotary Gouge Apparatus' (ROGA) (Reches and Lockner, 2010). The experimental faults are comprised of two solid cylindrical blocks with a raised-ring contact of 7 cm diameter and 1 cm width. These experiments revealed three general regimes of strength-velocity relations (Fig. 17a): (I) Dynamic weakening (drop

of 20-60% of static strength) as slip velocity increased from ~0.0003 m/s (lowest possible experimental velocity) to a critical velocity, Vc=0.05-0.16 m/s; (II) Abrupt transition to dynamic strengthening regime during which the fault strength almost regains its static strength; and (III) Quasi-constant strength with further possible drops as velocity approaches ~1 m/s. The critical velocity depends on the sample lithology: Vc is ~0.06 m/s for granite, ~0.008 m/s for syenite, ~0.01 m/s for diorite, and ~0.16 m/s for quartzite. The strengthening stage is associated with temperature increase, wear-rate increase, and the occurrence of intense, high frequency stick-slip events (Reches & Lockner, 2010).

Similar velocity dependence (Fig. 17b) was observed by Kuwano and Hatano (2011). Reches and Lockner (2010) and Sammis et al. (2011) attributed the strengthening at high velocity to dehydration of the thin water layer that covers the gouge particles as the temperature increases. On the other hand, it is noted that dolomite samples (non-siliceous), which were deformed under similar conditions, did not exhibit the velocity strengthening.

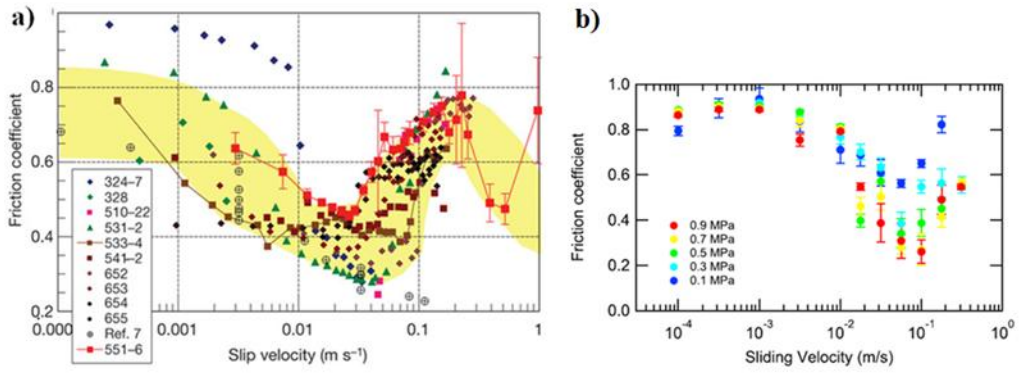


**Figure 17. Granite friction coefficients vs velocity reported by (a) Reches and Lockner (2010) and (b) Kuwano and Hatano (2011).**

*Earthquake-like-slip-event*

Chang et al. (2012) used a different loading approach for high-velocity shear experiments that they termed "earthquake-like slip event" (ELSE). The idea is to abruptly deliver a finite amount of energy to the fault patch that spontaneously dissipates the energy without operator intervention. The finite amount of energy is carried by the spinning a 225-kg disk-shaped flywheel and then a fast-acting clutch engage the sample-half that is forced to rotate until all the kinetic energy is dissipated. These ELSE experiments were thus under impact loading, which is likely to be analogous to the loading of a fault patch during a natural earthquake (Chang et al., 2012). All were implemented at slip velocity (up to 1.0 m/s) and normal stresses of up to 30 MPa. The experimental observations revealed a systematic dynamic-weakening (Fig. 18b) that was attributed to powder lubrication (Chang et al., 2012). For example, in the typical run #2782 (Fig. 18a), there is a briefly drop of patch strength from 0.8 to a minimum value of ~0.25, and then a strength recovery after a slip distance of 0.25 m. Similar patterns of strength evolution were observed for other ELSE-based experiments (Chang et al., 2012).

The significant features of ELSE experiments are: (1) short slip weakening with Dc = 1-5 cm; (2) the initial friction drop was followed by strengthening; and (3) a striking different with respect to constant velocity experiments in the dependency between friction coefficient and slip-velocity (Fig. bc). The dissimilarity compared with steady-state experiment is attributed to the different loading mode, as will be discussed later chapter.

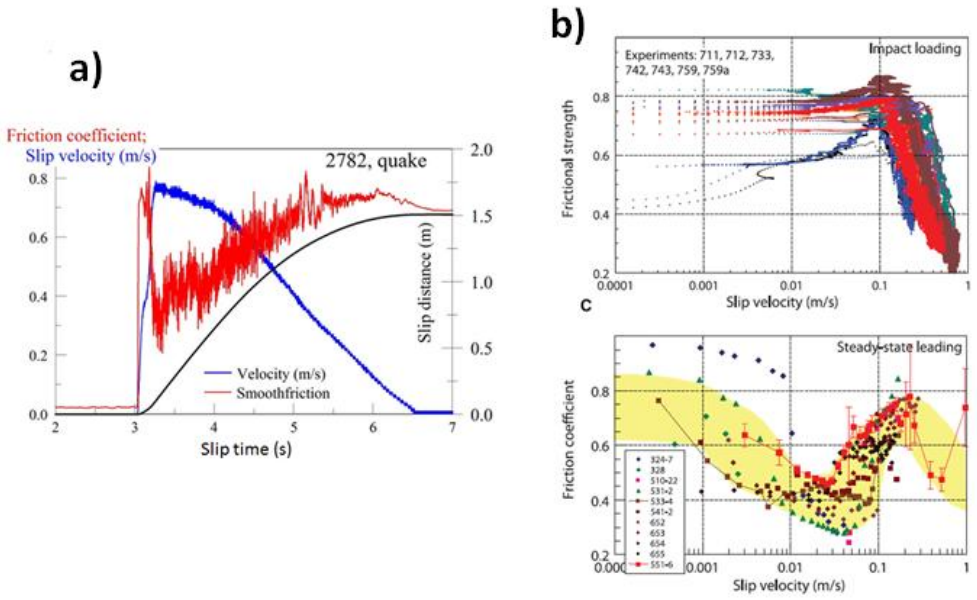


**Figure 18. a) The evolution of frictional strength in ELSE experiments (#2782) with respect to slip distance; b) the friction vs velocity for ELSE experiments (after Chang et al., 2012); and (c) the friction vs velocity for the steady-state experiments (after Reches and Lockner, 2010).**

## Mechanisms of dynamic weakening

Several mechanisms have been proposed to explain dynamic weakening during earthquakes. Anooshehpoor and Brune (1999) proposed normal interface vibrations while most of other mechanisms indicate that the critical problem for earthquake is shear-stress drop. The early experiments, e.g., RSF, attribute the dynamic behavior of friction to the complexity of contact asperities. The stress drop is commonly generalized as linear slip weakening which will be discussed in the model section. However, the mechanism for explaining the weakening characterized by Dc remains controversial. Marone and Kilgore (1993) suggest that Dc is controlled by the thickness of the gouge layer between fault surfaces as well as the roughness. Ohnaka and Shen (1999) proposed a strong scaling relation between Dc and the wavelength of the surface roughness. Moreover, the geometric irregularity of the rupturing surface (Ohnaka and

Shen, 1999), the heterogeneity of the stress, and material contrast could also cast their influences on Dc.

Currently, there is great improvement in laboratory experiments for studying simulated faults. The abundance of observations provides an opportunity to look into the intrinsic mechanisms rather the outsider parameters (e.g., geometric irregularity). Such occurrence of dynamic weakening features and the high temperature recorded on the sliding surface are not observed at low slip rates before. There is a converging understanding that most of the current observations and theories indicate that shear-stress drop dominate the fault propagation during fast coseismic slip. Most of the new mechanisms are proposed regarding only to the experiments at high slip velocity. I introduce here some representative mechanisms, including shear melting (Tsutsumi and shimamoto, 1997; Goldsby and Tullis, 2011), pore fluid pressurization (Lachenbruch, 1980), thermal decompositions (Han et al., 2007), elastohydrodynamic lubrication (Brodsky and Kanamori, 2001), power lubrications (Reches and Lockner, 2010) and nanoparticle smoothing (Chen et al., 2013). However, these mechanisms are not applied to numerical simulation yet due to the controversial complexity of the theories.

### *Flash melting*

Rice (2006) examined the primary weakening mechanisms for shallow earthquakes due to a thermal origin. The involved processes include thermal pressurization of pore fluid by frictional heating which reduces the fault strength and flash heating at highly-stressed micro-contacts at high slip rates reduces the friction. Goldsby and Tullis (2011) present laboratory experiments at fast seismic slip rates and

propose a mechanism of flash heating of microscopic asperity contacts to explain the observed reduction of shear strengths. The high-velocity experiments result in seismic slip velocities up to 0.4 m/s (Fig.19) with slip distances up to 45 mm. Compared with low velocity experiments (e.g., RSF), the experiments of high rates allow insufficient time for frictional heat to diffuse away, resulting in increased temperature and decreased contact strength. If the temperature is high enough, even melting could occur consistent with extreme weakening observations. Such observations are also supported by the work of Di Toro et al. (2004) and Sone and Shimamoto (2009). Flash heating likely dominates the strength of the fault during the initial stages. Other stages of the earthquakes, however, should be attributed to other dynamic mechanisms.

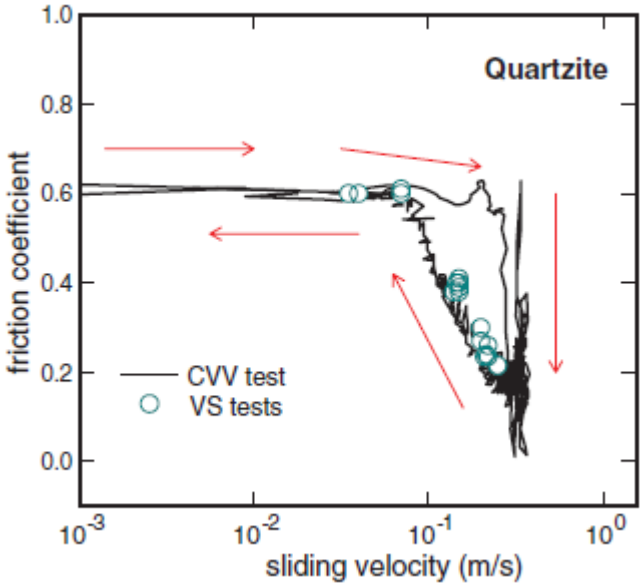


**Figure 19. Friction coefficient vs. sliding velocity on several high rates tests on the same quartzite sample (after Goldsby and Tullis, 2011). CVV: Continuously various velocity; VS: Velocity stepping.**

*Pore fluid pressurization*

Lachenbruch (1980) proposed the expansion of pore fluid caused by frictional heating during instable sliding of faults could have an important effect to reduce the

frictional strength. Fig. 20 presents the theoretical contours maps of increasing pore fluid pressure in relation with temperature. The pressure could increase rapidly (≥10 bars/℃) if confined water is heated. However, the production of such thermal pressurization is constraint by several processes: 1) the increase of temperature due to friction; 2) the appreciable fluid pressure rise due to the temperature rise; 3) presence of continuous fluid phase. Thus the uncertainty in the controlling parameters of the in-situ conditions will lead to various fault behavior. This theory indicates the possible of faulting or strengthening due to the combined thermal effects with dilatational strain of a few percent of pore volume.

The study of Chi-chi earthquake (M=7.6, 1999) in Taiwan, indicated that the low-permeability shale could result the enhanced long-period motion in the north (Andrews, 2005). The thermal pressurization due to frictional heating operates in a Coulomb solid, which reduces effective pressure and so reduces shear stress resisting slip. Theoretically, the stress drop could be complete if the diffusion of pressurized fluid away from the fault is sufficiently limited when slip is 4-8 times the pressurized thickness. Dynamic simulations of the Chi-chi earthquake have been implemented and it presents plausible overall results, while the prediction is still highly uncertain due to the complexity of the process within fault zone.

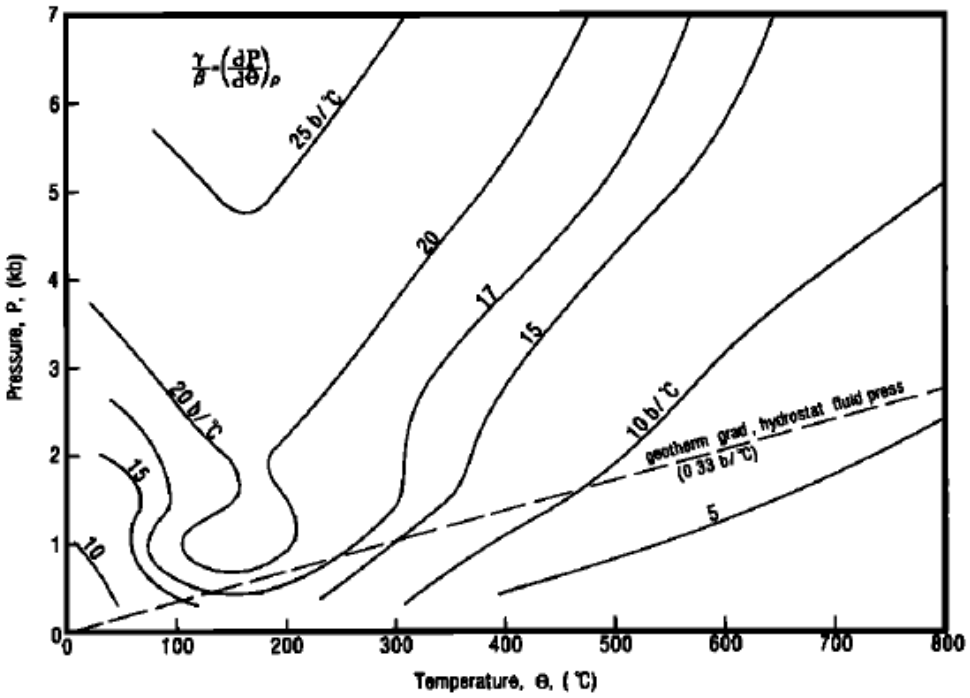


**Figure 20. The increase in pressure P with temperature at constant density for water under upper crustal conditions. Dashed line shows conditions for a geothermal gradient of 30 ℃/km and for fluid pressure in an unconfined water column with unite specific gravity (after Lachenbruch, 1980)**

*Thermal decomposition and degassing*

Han et al. (2007) conducted experiments on Carrara marble at slip rates up to 1.3 m/s and a mechanism of thermal decomposition of calcite is proposed to explain the fault weakening. Fig. 21 shows the friction drop from 0.6 to 0.04 at rate of 1.17 m/s under a normal stress of 12.2 MPa. The two sensors determine the emission of $CO_2$ and the concentration increase roughly agrees with the expected and estimated emission of $CO_2$ from the volume of decomposed calcite. Thus the observations shows pronounced slip weakening while undergoing calcite decomposition at high slip rates, which means that a fault could lost its strength as a result of release of high-pressure gas. The

dehydration reaction requires temperature of 800 ℃ for carbonates and 150-200 ℃ for phyllosilicates.

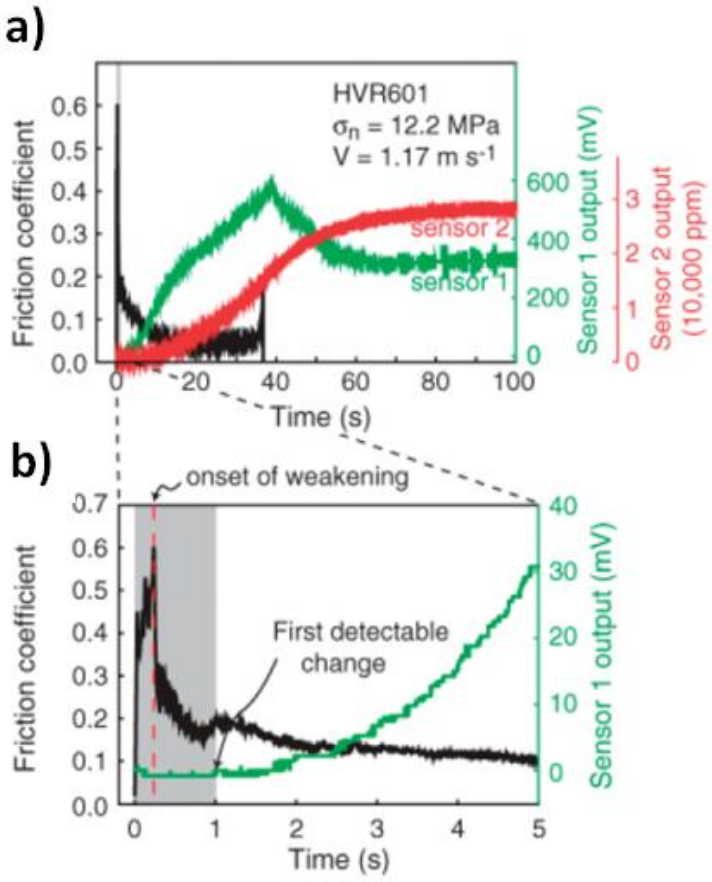


**Figure 21. Monitoring of friction coefficient and $CO_2$ gas emission against time. Sensor 1 is a quick –response sensor for detecting the onset of $CO_2$ emission, and sensor 2 is a slow response sensor for monitoring the amount of emitted $CO_2$.**

*Elastohydrodynamic lubrication*

Brodsky and Kanamori (2001) considered a previously undiscussed contribution by a viscous fluid rather than the elevated pressures due to friction heating (Lachenbruch, 1980). The fault is proposed in a way analogous to lubricated bearings. Initially, as the two uneven solid surfaces slide past each other with viscous fluid in between, the fault is under solid-solid friction stage with high friction coefficient. The

finite viscosity of the fluid resists the motion and thus forming a high pressure gradient. Then the fault goes to a "mixed" stage that is lubricated partially by solid-solid and partially by a continuous film and lubrication pressure. More importantly, the pore pressure keeps increasing and reduced the effective stress on the solid-solid interfaces and the fault goes to hydrodynamic lubrication stage in which the friction is determined by the viscous stress. All three types of behavior are schematically presented in Fig. 22.

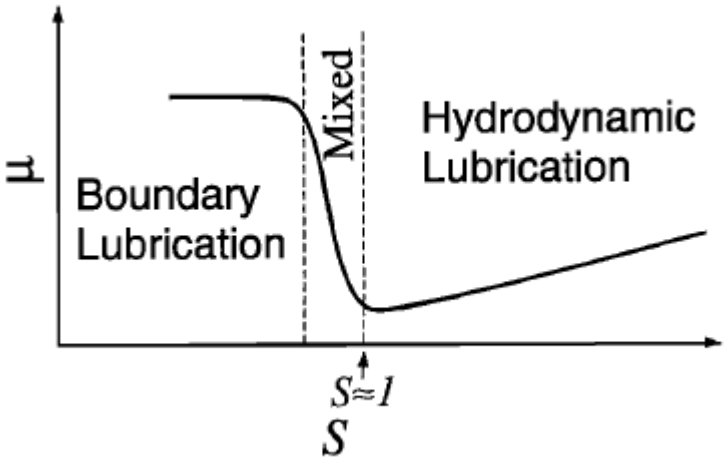


**Figure 22 The Stribeck curve schematically shows the variation of the coefficient of friction m with the dimensionless Sommerfeld number, S. In the region labeled "boundary lubrication", solid-solid friction predominates. Between the dashed lines is the mixed regime where solid-solid friction is reduced by the lubrication pressure. In the "hydrodynamic lubrication" region, solid-solid friction is eliminated, and the friction is determined by the viscous stress. (After Brodsky and Kanamori, 2001)**

*Nano-powder lubication*

Reches and Lockner (2010) and Sammis et al. (2011) suggested that the weakening is controlled by gouge powder lubrication due to coating of the powder grains by a thin layer of water that is 2-3 monolayers thick. In the friction experiments at rotary shear apparatus approaching 1 m/s with normal stress up to 7 MPa, a 0.1-0.4 mm thick layer of fine-grain (50-100 nm) rock powder were found between the sliding

surfaces. The observations of friction were detailed discussed in previous section, which could be identified as four regimes (Fig. 23, Sammis et al., 2011): 1), at velocity <0.001 cm/s, the friction is high in the range 0.6-0.75; 2) at velocity of 0.01-0.05 m/s, there is a dynamic weakening to 0.3; 3) at velocity of 0.1-0.2 m/s, there is a dynamic strengthening to 0.6-0.75; 4) the second round of weakening due to globally failure when velocity is close to 1 m/s. The key observation here is the dynamic strengthening in regime 3 is related to the increasing temperature above 120 ℃, and this strengthening is further attributed to the evaporation of adsorbed water from the gouge particles. Thus the friction (weakening/strengthening) response is determined by the changes in the thin film of adsorbed water, rather than an evolution in grain-size or packing structure.

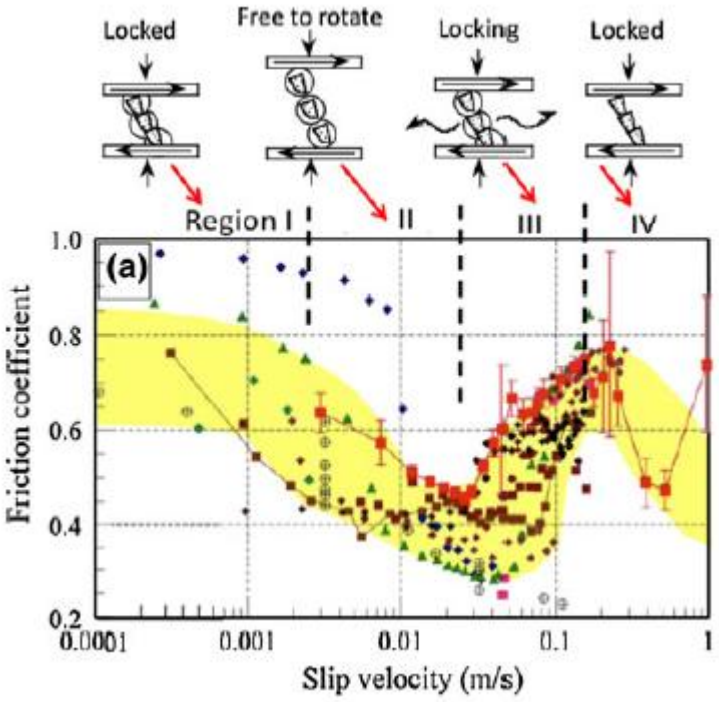


**Figure 23. The friction coefficient as a function of slip velocity for Sierra White granite at normal stress of 1-7 MPa. Four deformation regimes are identified by the schematic diagrams that indicate the physical conditions in each regime (after Sammis et al, 2011).**

*Slip smoothing*

Chen et al. (2013) analyzed the nano- to micro-scale frictional processes along experimental fautls that slipped at rates approaching 1.0 m/s. The main observations

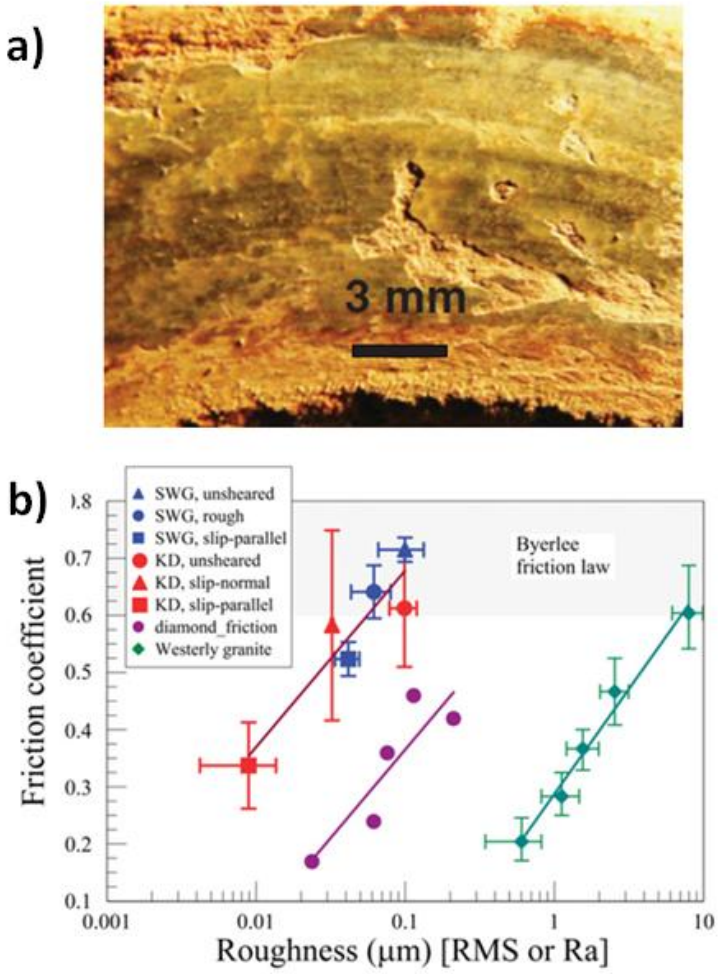


**Figure 24 (a) Experimental fault surface of Kasota dolomite (KD; Minnesota, United States) after run KD-1516 of present study. (b) Roughness-friction relation at micron scale. Shown are room-dry FC and the AFM roughness of KDand Sierra White granite (SWG; California, United States) surfaces (roughness as RMS [root mean square] for 1 μm segments), diamond sample A (Hayward et al., 1992), and Westerly granite from Rhode Island, United States (Byerlee, 1967) (roughness as Ra [mean height differences from a center line]). The relations (solid lines) have the form: FC = a ln roughness) + b, where (a, b) are (0.13, 0.99) for KD-SWG combined, (0.13, 0.67) for diamond A, and (0.16, 0.29) for Westerly granite. (after Chen et al., 2013).**

include intense dynamic weakening at high slip velocity and formation of a hard and shining surface (Fig. 24a) with a smoother axis along the slip direction. The dynamic weakening is attributed to the friction-roughness relation and the analysis showed that the smoother surface have lower friction (Byerlee, 1967; Hayward et al, 1992). According to the roughness of the fault surfaces (Fig. 24b) as a function of the micron-scale root mean square (RMS), the surfaces with RMS values of <100 nm shows weakening while no weakening on rougher surfaces. These processes are only observed at high velocity (V>Vc~0.08 m/s), Chen et al. (2013) proposed that slip smoothing can be an effective mechanism for dynamic weakening during high slip velocity.

### *Evaluation of experimental friction analysis*

Fault weakening mechanism is still an enigmatic frontier, and our main motivation is to construct a realistic the friction model for earthquake weakening. Table 1 present a general comparison between the conditions of experimental friction analyses, and I discuss below the strong and weak points the various experimental procedures.

#### *Low velocity and low distance*

Most commonly used friction model are slip weakening (Ida 1972; Andrews, 1976; Day and Dalguer, 2005) and RSF (Dieterich, 1979; Ruina, 1983; Lapusta et al., 2000; Ampuero and Ben-Zion, 2008). These models, which were derived from low velocity and low slip distance experiments, illustrate profound stress drop that was attributed to weakening and area modification at contacting asperities. These models, however, lack detailed explanation and direct evidence at the micro-scale. The main contributions of these models are the analogous friction behavior to what is expected

during earthquake instability. The applications of these models to seismic analyses provided useful insight and procedures for characterization of earthquake rupture. Once mature friction mechanisms appeared with an applicable friction model, it becomes convenient to integrate new constitutive relations into the fault simulation.

**Table 1. A summary of friction experiments and related friction model for rupture modeling**

| Experiments | Velocity (m/s) | Slip distance (m) | Normal stress (MPa) | Model available for simulation | Comments |
|---|---|---|---|---|---|
| Steady-state I | Constant; $1^{-6}$~1 | 1 mm ~ 4 m | <10 | Yes | Widely used; simple physics. |
| Foam rubbers | | | | Yes | Constant friction. |
| Rate and state | $1^{-8}$~$1^{-5}$ | Um | 6 | Yes | Widely used; low velocity |
| Steady-state II | $1^{-5}$-1 | M | 5-30 | No | High velocity; new physics. |
| ELSE | $1^{-4}$~1 | M | 30 | No | High velocity; impact loading |

*Steady-state and high-velocity*

In recent two decades, the rotary shear apparatuses greatly advance the laboratory experiments of earthquake simulation. The first important finding is the observed longer critical slip distance, Dc, of meters scale that better fit seismic

inversion of large earthquakes. Secondly, high temperature and associated features (e.g., flash melting, dehydration) greatly expand the insights for exploring the weakening mechanisms. Most of the friction models have been proposed after the experiments at seismic rates, including shear melting (Tsutsumi and shimamoto, 1997; Goldsby and Tullis, 2011), pore fluid pressurization (Lachenbruch, 1980), thermal decompositions (Han et al., 2007) and power lubrications (Reches and Lockner, 2010). Each mechanism explains one aspect evidenced by the laboratory data. Although they remain controversial and there is not a uniform model to explain the earthquake yet, some of them start showing some converging features. For example, the flash melting is accepted as an initial stage of weakening in quartz-rich rocks. The melting weakening for gabbro at high rates of 1-2m/s after long slip is confirmed by observations. The production of thin layer of gouges is discussed though the mechanism of interaction of the gouge is not fully explained yet. However, more features are under criticized and testing stage, including dynamic strengthening (Reches and Lockner, 2010), acceleration effects, and decomposition etc. Few of current mechanisms have been successfully transformed into numerical friction model and applied to the fault modeling.

*ELSE*

Realized that the fault is propagated in velocity of accelerating-deceleration rather than steady-state, some of the experiments tried different loading for the high rates laboratory simulations (Sone and Shimamoto, 2009; Chang et al., 2012). Sone and Shimamoto (2009) sheared an experimental fault by loading it with acceleration and deceleration stages and indicated the necessary to incorporate velocity-controlled

physical processes. This point was also recognized by Chang et al. (2012) who compared the friction-velocity relations of the same granite loaded either in constant/stepping velocity or in flywheel impacting. It provides the hint about a possibility of the impact loading that might control the friction. If it could significantly increase rock brittleness and rheology, and then by doing so would activate weakening mechanisms that do no operate at classical loading experiment. This idea is to be discussed later.

# Chapter 3:

# High-Velocity Friction Experiments

## Introduction

The dynamic weakening of a fault-zone is probably the most important property in controlling earthquake instability, associated ground motion, and the energy balance of earthquakes (e.g., Kanamori, 2004). Ideally, the fault weakening is formulated by constitutive laws, such as rate- and state- friction (RSF) (e.g., Dieterich, 1979; Marone, 1998; Scholz, 1998), or slip-weakening (e.g., Palmer and Rice, 1973; Andrews, 2005). In this chapter, I review the results of high velocity experiments and discuss their application in numerical modeling. There are three sources of the experimental data including: 1) part of the steady-state experiments on Westerly granite from Kuwano and Hatano (2011); 2) most of the steady-state experiments on Sierra White Granite (SWG) from Reches and Lockner (2010) and additional runs from Liao and Reches (2012); 3) impact loading experiments from Chang et al (2012) and additional runs from the University of Oklahoma.

Most commonly, rock friction experiments are conducted at controlled-velocity mode during which the slip velocity is controlled by the apparatus at a constant or stepping values. Experiments of high slip-velocity and long slip-distance are conducted on rotary shear machines (Beeler et al., 1996; Tsutsumi and Shimamoto, 1997; Goldsby and Tullis, 2011; DiToro et al., 2011; Reches and Lockner, 2010). This procedure allows to derive a constitutive friction law, but it does not necessarily capture the complexity of earthquake rupture. Sone and Shimamoto (2009) sheared an experimental

fault by loading it with acceleration and deceleration stages and indicated the necessary to incorporate such procedures at seismic slip rates. This point was further investigated by Chang et al. (2012) who compared the friction-velocity relations of the same granite loaded either in constant/stepping velocity or in flywheel impacting. The impact loading induces high strain-rates of ~$10^4 s^{-1}$ that significantly increase rock brittleness and rheology, and by doing so would activate weakening mechanisms that do no operate at classical loading experiment. As both sets of experiments were conducted on the same rock samples, the dissimilarity is attributed solely to the different loading mode, as already suggested by Sone and Shimamoto (2009).

## Steady-state experiments at the University of Oklahoma

### *Experiment setup*

The first part of this work (steady-state experiments) is from Liao and Reches (2012). The analyzed experiments were conducted on the ROGA in University of Oklahoma. The following description of the apparatus is taken from Reches and Lockner (2010) and related lab proposals. The ROGA system (Rotary Gouge Apparatus, Fig. 1) satisfies the following conditions: (1) normal stress of tens to hundreds of MPa; (2) slip velocity of ~1 m/s; (3) rise-time of less than 1 s; and (4) unlimited slip distances.

In the experiments, the fault is composed of solid blocks of Sierra White granite. Each sample includes two cylindrical blocks, diameter = 101.6 mm, height = 50.8 mm. For ~uniform velocity, the upper block has a raised ring with ID = 63.2 mm and OD = 82.3 mm; the blocks are pressed across this raised ring. Thermocouples are cemented into holes drilled 3 mm and 6 mm away from the sliding surfaces (Fig. 1c). Each pair of

blocks wore to form gouge in between at different slip velocities of 0.001-1 m/s. A large set of experiments will be executed and a large quantity of data will be collected by LabView at frequency of ~100-1000 Hz.

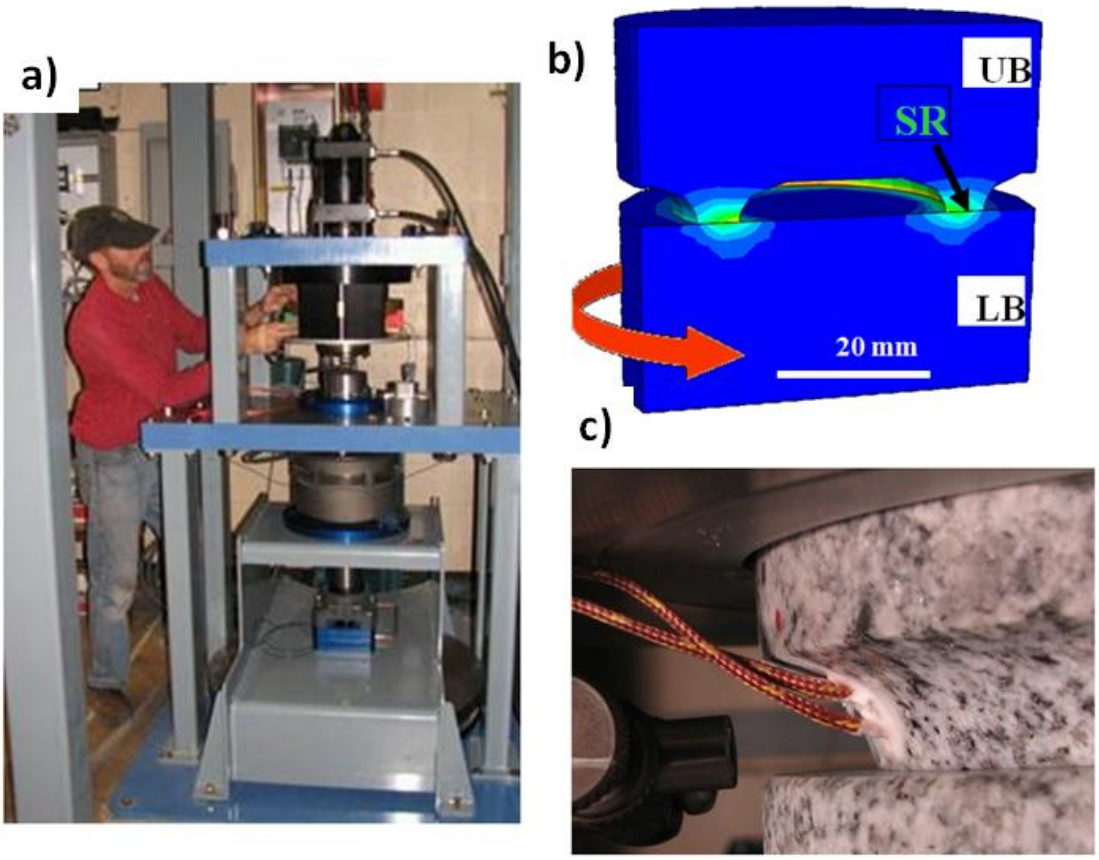


**Figure 1. a)The Rotary Shear Apparatus with builder Joel Young. b) The numerical model of the shearing samples for temperature simulation and c) The sample block assembled in the loading frame (after Reches and Lockner (2010)Experimental observations**

## *Results*

### *Steady-state observations*

The experiments were conducted with a rotary shear apparatus and cylindrical rock samples (above) (Reches and Lockner, 2010; Chang et al., 2012). The experimentally monitored parameters include slip distance, slip velocity, fault-normal displacement (dilation), shear stress and normal stress. Sample temperature was measured by thermocouples that are embdded ~3mm away from the slip surfaces. The normal load was maintained constant during a given experiment, and the experiments were performed at room conditions. Fault strength is represented by the friction coefficient, $\mu = \tau/\sigma_N$ (where $\tau$ is shear stress and $\sigma_N$ the normal stress). The slip velocity was either maintained constant, or increased or decreased in steps. I present results of tests with samples of Sierra White granite (SWG) (after Reches and Lockner, 2010), and new results for samples of Blue quartzite, St. Cloud diorite, Fredricksburg syenite, and Karoo gabbro. The tests with SWG samples were run under the widest range of conditions and the numeric model was derived only for this rock.

Reches and Lockner (2010) determined the friction-velocity relations of granite for a velocity range of .0003-1 m/s and normal stress up to 7 MPa. Their results revealed three general regimes of friction-velocity relations (Fig. 2a):

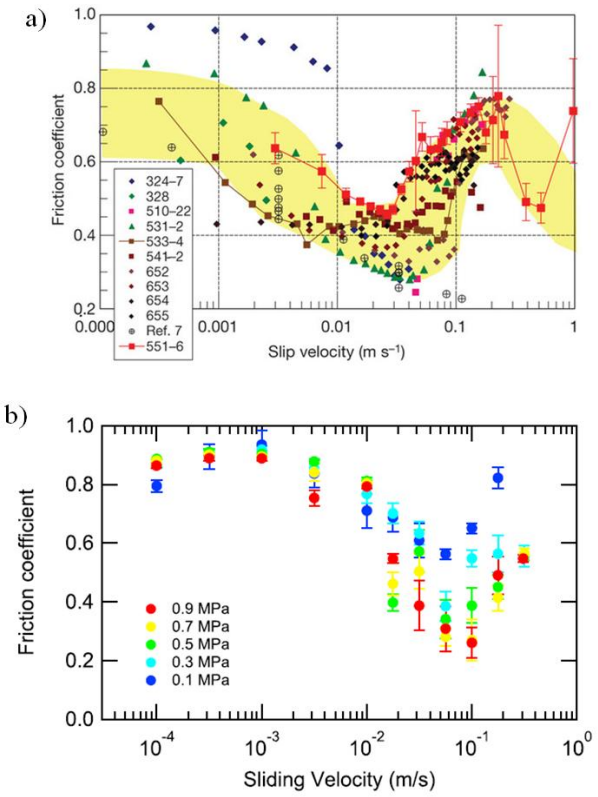


**Figure 2. Experimental friction-velocity relations in (a) Sierra White granite (after Reches and Lockner, 2010) and (b) Westerly ganite (after Kuwano and Hatano, 2011).**

(I) Dynamic-weakening (drop of 20-60% of static strength) as slip velocity increased from ~0.0003 m/s to a critical velocity of $V_c$ ~ 0.03 m/s, during which the friction coefficient was 0.3-0.45.

(II) Transition to dynamic-strengthening regime in the velocity range of V = 0.06-0.2 m/s, during which the fault strength almost regained its static strength; and

(III) Quasi-constant strength for V > 0.2 m/s, with possible further drops as velocity approaches ~1 m/s. Only few experiments were conducted in this range due to sample failure by thermal fracturing.

Similar pattern of weakening-strengthening of Westerly granite samples was recently observed by Kuwano and Hatano (2011) (Fig. 2b). They showed that the friction coefficient dropped in the velocity range of 0.001-0.06 m/s, and rose in the velocity range of 0.06-0.2 m/s (Fig. 1b). Earlier work of Tsutsumi and Shimamoto (1997) also indicated temporal periods of strengthening, in which the friction sharply increased, and visible melting was observed at the strength peak when the slip rate was increased from 0.55 to 0.73 m/s.

To further explore the occurrence of dynamic-strengthening, I tested four other rocks under conditions similar to Reches and Lockner (2010) tests. The new experiments were conducted on samples made of Blue quartzite (Fig. 3a), St. Cloud diorite (Fig. 3b), Fredricksburg syenite (Fig. 3c), and Karoo gabbro (Fig. 3d). The diorite (Fig. 3b) and syenite (Fig. 3c) samples displayed a distinct transition into dynamic-strengthening regime (red arrows). The critical transition velocity, $V_C$, depends on the sample lithology; it is ~0.02 m/s and ~0.01 m/s for the diorite and syenite, respectively. The Blue quartzite tests displayed only negligible weakening and

strengthening (Fig. 3a).

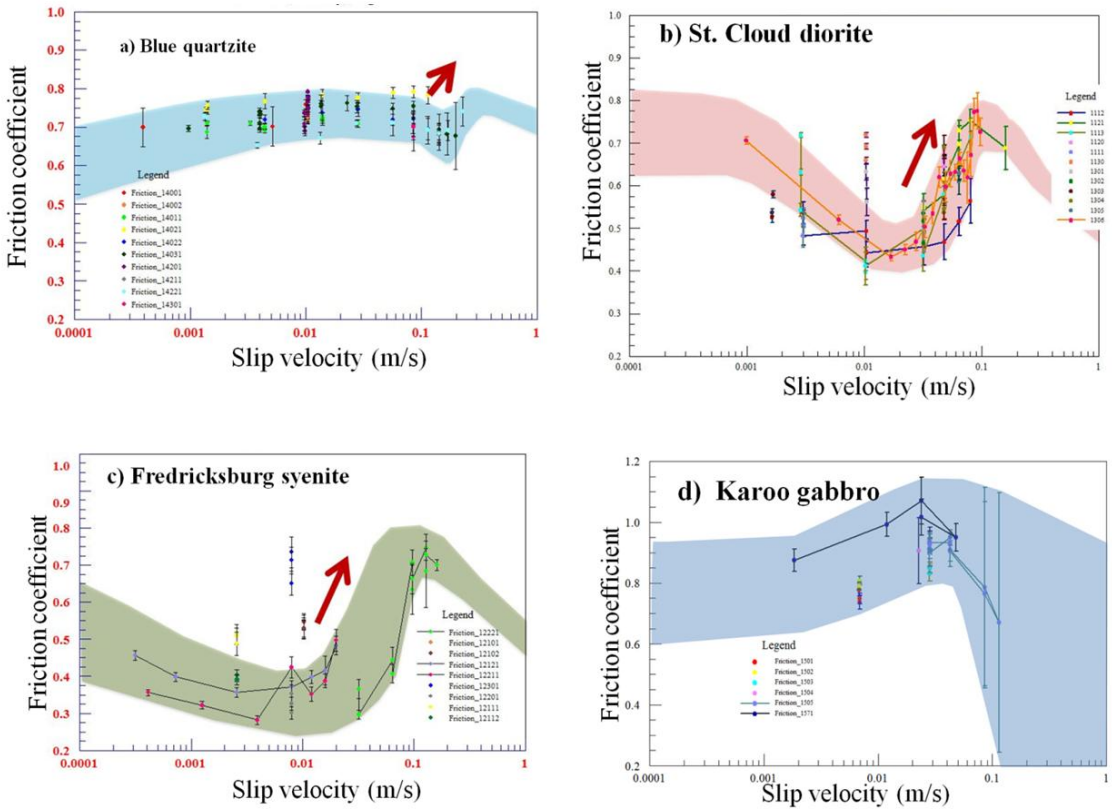


**Figure 3. Friction-velocity relations in shear experiements of Blue quartzite (a), St. Cloud diorite (b), Fredricksburg syenite (c), and Karoo gabbro (d). Connected lines indicated data from step-velocities experiments. Unconnected dots indicate single velocity experiments.Note velocity-weakening and velocity-strengthening stages (marked by red arrows) in (a)-(c) and no velocity-strengthening in (d).**

*Constitutive friction relations for quartz bearing igneous rocks*

The most striking feature of the relations between the friction coefficient and slip-velocity for the above experiments is the systematic transition from weakening under low velocity to strengthening at higher velocities (Figs. 2, 3). We refer to this feature of **WE**akening-**ST**rengthening as the **WEST** mode, and developed a numerical model to describe its character. The model is based on two central assumptions. First, the friction coefficients, in both weakening and strengthening regimes, can be presented

as dependent of the slip distance, and slip velocity. This assumption was employed in many previous models (Dieterich, 1979; Beeler et al, 1994; Tsutsumi and Shimamoto, 1997; Reches and Lockner, 2010; DiToro et al., 2011). Second, the weakening-strengthening mode reflects a transition between different frictional mechanisms. Reches and Lockner (2010) and Sammis et al. (2011) suggested that the weakening is controlled by gouge powder lubrication due to coating of the powder grains by a thin layer of water that is 2-3 monolayers thick. The dehydration of this layer at elevated temperature under high slip velocity leads to strengthening. It is thus assumed that the weakening and strengthening regimes have different parametric relation between friction and velocity.

### *Dynamic-weakening regime*

The experimental data set has large data scatter at low velocities (Fig.2; Reches and Lockner, 2010). For the range of V < 0.03 m/s (Fig. 4), I found the following relations of $\mu_K$ and slip velocity,

$$\mu_K(V) = 0.742 - \frac{0.375V}{0.00183 + V}, \text{for } V \leq 0.03 \text{ m/s} \quad (1)$$

The RMS (root mean square) of this solution is 0.83 while the correlation coefficient is 0.73. This simple solution provides reasonable fit to the scattered friction data (Fig. 4).

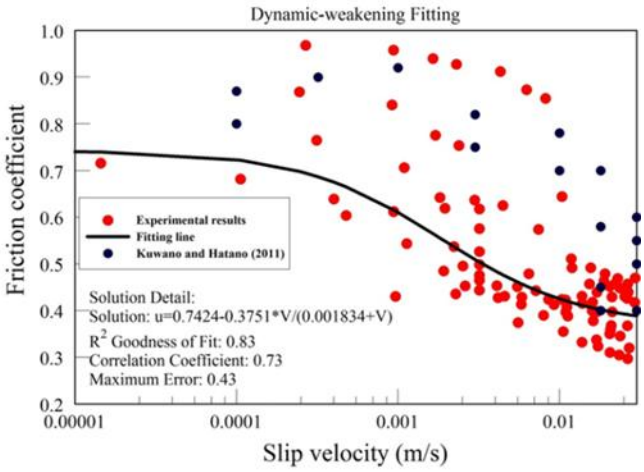


**Figure 4. The selected solution (red curve) for dynamic-weakening of kinetic friction coefficient of SWG for V = 0.0003-0.03m/s by Eureqa. Data for V < 0.003 m/s are from Reches and Lockner (2010) and Kuwano and Hatano (2011).**

### *Dynamic-strengthening regime*

In the strengthening regime of 0.03 m/s < V < 1.0 m/s (Fig. 5), the selected solution for velocity-controlled friction coefficient is

$$\mu_K(V) = 0.824 \exp\left(-\frac{0.0275}{V}\right), \quad \text{for } V > 0.03 m/s \tag{2}$$

The RMS of this solution is 0.91 and the correlation coefficient is 0.74. The trend of this exponential relation provide good fit for SWG (Reches and Lockner, 2010) in the strengthening trend (Fig. 5), and this trend generally fit the experimental results of Kuwano and Hatano (2011). Note: Friction during 0.305-0.4 m has been locally adjusted to comply with Fig. 4.

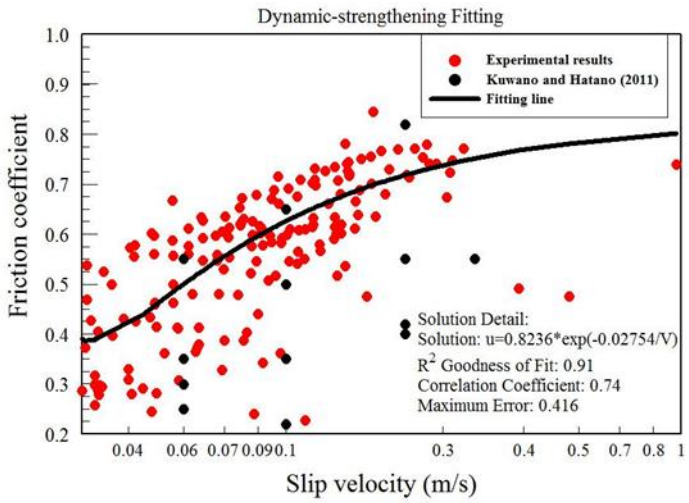


**Figure 5. a) The selected solution (red curve) for dynamic-strengthening of SWG for V = 0.03-0.3m/s by Eureqa. Data for V > 0.003 m/s are from Reches and Lockner (2010) and Kuwano and Hatano (2011).**

### *Slip-weakening relations*

For the ten experimental results (Fig. 6), I selected the slip-weakening function as,

$$\mu = \mu(D) = 0.2663\ (\pm 0.1)\exp(-D) + 0.4061(\pm 0.15) \qquad (3)$$

For D=0, which is slip initiation, the calculated $\mu = \mu_S = 0.6724$. For D > Dc (e.g., 3.0 m), the calculated $\mu = \mu_K = 0.41$.

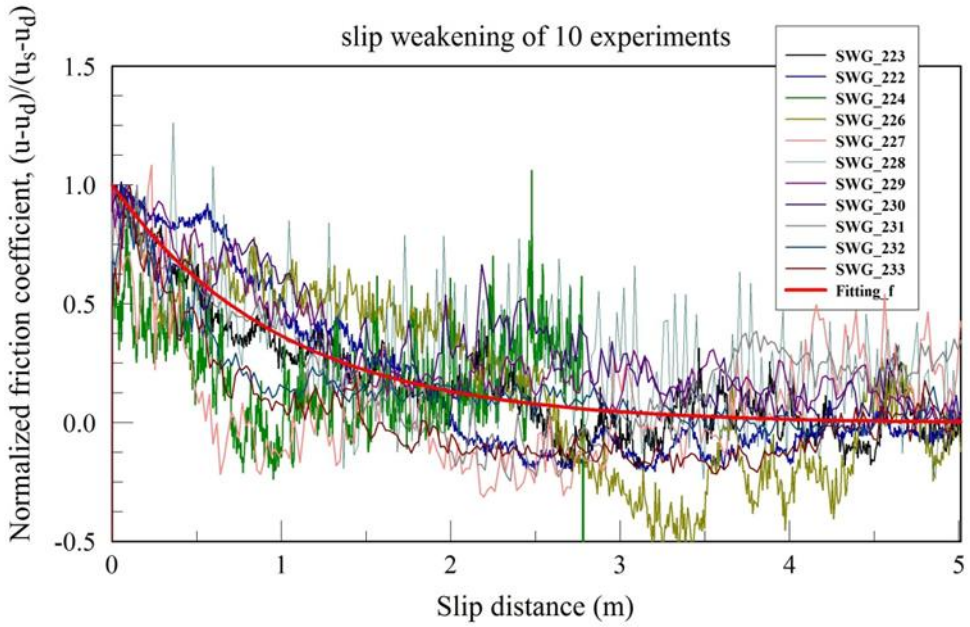


**Figure 6. a) The best fit solution (red curve) for slip distance weakening in ten experiments. SWG 222, 223, 224 were run at velocity 0.024 m/s; SWG 226-232 were run at 0.072 m/s; $\sigma_N$ = 1.1 MPa. The solution is $\mu$= 0.2663(±0.1) exp (-D) +0.4061(±0.15). The constants can be adjusted for specific case.**

### *Model synthesis*

By substitute the 0.4061 (Eq. 3) by Eq. (2), Eq. (3) is generalized into,

$$\mu(D, V) = 0.2663 \cdot \exp(-D) + \mu_K(V) \quad (9)$$

This simple exponential function characterized the weakening process with relating small deviation of the data.

### *An example of application to the experiment*

Fig. 7 displays the friction evolution in two experiments with wide velocity range. Fig. 7a displays a slide-hold-slide run under $\sigma_N$ = 1.1 MPa and hold times of 10 s between the multiple velocity steps. Under this short hold time, the friction coefficient

curve displays quasi-continuous trend. There is a marked weakening as the velocity was increased to ~ 0.04 m/s, followed by a gentle strengthening at higher velocities. The modeling results were lower at beginning than expected and strengthening occurred earlier. Fig. 7b displays two major features: an initial gradual weakening in the slip velocity range of ~0.0003 m/s to a critical velocity of ~0.03 m/s, and a fast strengthening at velocities from ~0.03 m/s to 0.2 m/s. In the final stage, the friction reaches ~0.8. The modeling simulates the weakening-strengthening pattern, but it fails to follow the experimental results in the region faster than the critical velocity. In the experiment, the friction coefficient remained relatively low from ~3 m to ~11 m, where the simulated results predicted earlier strengthening. Also, an abrupt friction rise was observed in the experiment (at ~ 11 m) whereas the model indicated smooth and continuous strengthening.

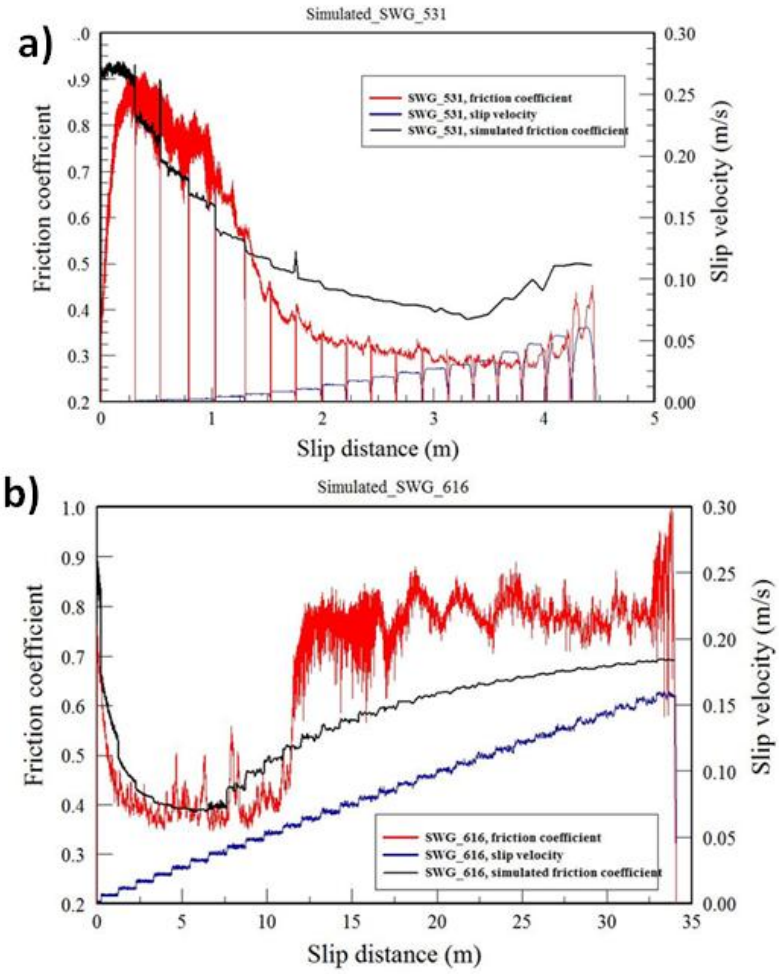


**Figure 7. WEST model simulation and experimental results for a) SWG 531, $\sigma_N$ = 1.1 MPa, and b) SWG 616, $\sigma_N$ =5.0 MPa. Friction coefficient is shown for a full-velocity continuously in sliding distance together with a best fit modeling result.**

## Is steady-state data relevant to earthquake slip behavior?

### *Background*

The common difference between 'static' friction and 'dynamic' friction has been known even before Coulomb's days. In geophysics, the weakening associated with the transition from static to dynamic friction is the central controlling parameter of earthquake instability. For example, Gilbert stated after the 1872 Owens Valley earthquake: "…strain increases until it is sufficient to overcome the starting friction

along the fracture." Following this concept, major experimental effort was devoted to study rock-friction and the transition from static to dynamic behavior. Most of these experiments however, were conducted under steady-state conditions of steady slip velocity, and the empirical results were applied to earthquake modeling, for example through the rate- and state- friction law (RSF) (Scholz, 1998). It is argued here that as steady-state conditions are not likely to materialize during earthquakes, the rock frictional properties that were determined in steady-state experiments may be irrelevant for modeling of earthquake rupture.

Experimentally, steady-state friction is determined by forcing two blocks of rocks to slip against each other under a constant velocity. For most rocks, the frictional resistance drops from its initial (static) value to a constant, steady-state level after slipping for a weakening distance, which is frequently termed the 'critical distance', Dc. The later depends on the normal stress, slip velocity and gouge thickness, and it varies between tens to hundreds of microns under slip velocities of ~ 1 μm/s to meters during large earthquakes. In a classical friction experiment, the slip velocity is carefully controlled to achieve steady-state conditions of stable sliding. Three lines of argument suggest that friction data obtained in this experimental approach are probably immaterial to rock friction during earthquakes.

First, earthquakes are not a steady-state process. They initiate at a small nucleation area and grow by a propagating rupture front that activates numerous fault-patches. Once the rupture front hits a patch, it undergoes intense, transient deformation with abrupt acceleration, weakening, deceleration and healing (Heaton, 1990). This evolution of mutually dependent strength, velocity and energy dissipation occurs during

a fraction of a second to a few seconds (rise-time). Thus, steady-state conditions are not likely to develop.

Second, during its slip, the fault-patch dissipates a finite amount of elastic energy that was stored in the surrounding crust during the interseismic period. It is thus anticipated that frictional behavior would change as the available energy diminished. Yet, in steady-state tests, the energy supply is maintained until steady-state is achieved, and in this respect the energy supply is 'unlimited'.

The third argument was clearly expressed (Di Toro et al., 2011) who wrote that the steady-state experiments of rate-and-state friction "… were performed at slip rates and displacements orders of magnitude smaller than those typical of earthquakes…. Given the low slip rates, these experiments lack a primary aspect of natural seismic slip: a large mechanical work-rate … [that] can be so large as to grind and mill the rock…., trigger mechanically and thermally activated chemical reactions, and, eventually, melt the rock… Work rate (not work alone) is the key parameter, as a given amount of work exchanged at a slow rate is buffered by dissipative processes and hence produces limited reactions."

Not all rock-friction experiments employ steady-state conditions. In the stick-slip design, an experimental fault-patch is loaded by slowly increasing normal and shear stresses until the fault spontaneously fails in an abrupt slip event (Ohnaka and Yamashita, 1989). The evolution of acceleration/deceleration, fast weakening, and healing during stick-slip events (Fig. 8a) occurs under a finite amount of elastic energy, and strongly resemble earthquake behavior. However, these experiments are limited to low slip velocity and tiny displacements (5-100 μm) that are orders of magnitude less

than the equivalents of large earthquake. To experimentally simulate large earthquakes, a finite amount of energy was delivered to an experimental fault-patch by impacting it with a massive flywheel (Chang et al., 2012). This impact loading profoundly affects the patch frictional response and yielded friction-velocity relations (Fig. 8b) that strikingly differ from those of steady-state experiments (Fig. 8c) for the same samples. Other recent studies with intense acceleration revealed rich and non-trivial friction evolution that cannot be understood in terms of steady-state conditions (Fig. 8d).

I thus propose that earthquake rupture processes should be modeled via friction laws that are relevant to the complex transients expected during earthquakes. These laws can be derived by synthesis of pertinent experimental results (e.g., Fig. 8) with friction theories.

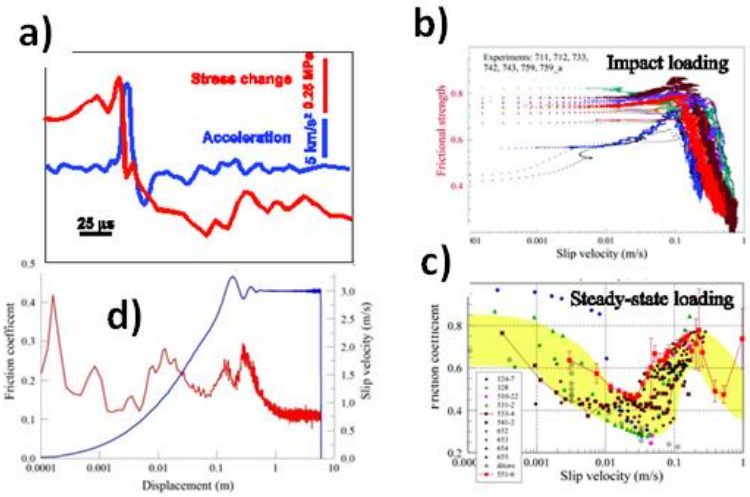


**Figure 8. Friction, acceleration and velocity during experimental attempt to simulate fault behavior during high-velocity slip. a). Stick-slip event along an experimental granite fault; b). Frictional strength vs slip velocity on the same granite samples under impact loading and c) steady-state loading; note the fundamental difference for earthquake velocity > 0.1 m/s. d). Strength and velocity during the slip acceleration stage along a gabbro sample (Niemeijer et al., 2010).**

## *Testing the impact loading hypothesis*

### *Approach*

I conducted high-velocity (up to 1.0 m/s) rotary shear experiments using siliceous rock samples under high normal stresses ( up to 30 MPa), to investigate the fault friction behavior under various modes of loading (Fig. 9a): (1) steady-state with granite samples; (2) quake-mode with Sierra White Granite (SWG; the rise time of fault slip is much shorter than total slip duration); (3) and ramp-mode with SWG (the rise time of fault slip is approximately the same as decelerated time). Figure 9b shows results from three loading modes at velocities ranging from 0.0001 m/s to 1.0 m/s.

### *Experimental observations*

In experiments of steady-state, I recognize three major friction-velocity regimes (Fig. 9b): (1) for V<0.008 m/s, friction values are relatively stable at a high range $\mu$=0.6-0.8; (2) for V=0.008-0.02 m/s, the frictions are decreased to $\mu$=0.3-0.4; (3) for V=0.02-1.0 m/s, the friction rapidly rises up to m=0.7-0.8. This kind of dynamic-weakening followed by quick dynamic-strengthening was previously observed (Reches and Lockner, 2010; Kuwano and Hatano, 2011).

In quake-mode, the results illustrate: (1) for V<0.1 m/s, there is a stage of slightly hardening for friction at range of 0.7-0.85; (2) for V=0.1-1.0 m/s, high initial shear stress decreases fast of 0.1 to 0.3 per 0.1 m/s accelerated; (3) after the strength reaches lowest value, the patch is re-strengthened as velocity decelerated from 1.0 m/s

back to 0.1 m/s. We refer this feature as “earthquake-like slip event” (ELSE) -based weakening and strength recovery (Chang et al., 2012).

The ramp-mode results shows: (1) for V<0.1 m/s, the friction stays at high value of ~0.8; (2) for V=0.1-0.5 m/s, shear stress decreases fast, approaching the lowest value of ~0.45; (3) for V=0.5-1.0 m/s, the shear stress increases from 0.45 to ~1; (4) after the strength reaches highest value, the patch is weakening to 0.8 as velocity decelerated. The strengthening in range (3) is attributed to the accumulation of temperature due to the long slip, and also possibly the rheology reasons. The mechanism remains to be discussed.

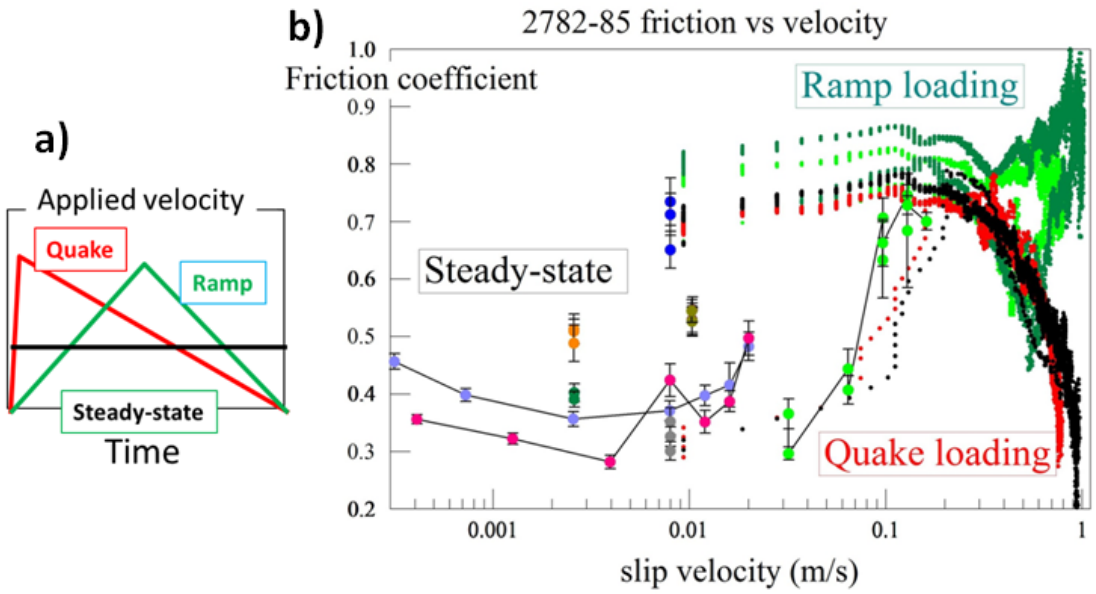


**Figure 9. Frictional strength and slip velocity on a fault patch of granite under three different loading modes. (a) Three loading modes for earthquake experiments, including steady-state, quake loading, and ramp loading. (b) Friction-velocity relations under aforementioned loading modes; note re-strengthening at ~0.02 m/s after weakening in steady-state, fast weakening at V>0.1 m/s with friction drop of 0.1 to 0.3 per 0.1 m/s for SWG samples under quake loading, and the strengthening of syenite at 0.5-1.0 m/s at ramp loading.**

*Discussion*

The rather identical and complex friction behavior in our impact loading fault experiments could lead to several important implications. The various friction-velocity relations suggest friction is a phenomena much more controlled by fault loading constraints than others. The inversions from seismograms support the fault ruptures propagate in stick-slip, or slip-pulse mode, which best simulated by quake-mode experiments (Sone and Shimamoto, 2009). Additionally, the experimental results comply with the early hypothesis (Brune, 1970; Heaton, 1990; Zheng and Rice, 1998; Sone and Shimamoto, 2009) that "a pulse may exist if the fault strength is low immediately behind the rupture front and builds up quickly at finite distance from the front". This idea of earthquake mechanism was postulated decades ago (Brune, 1970; Heaton, 1990) as an intrinsic fault property that will finally favor a new pulse-like mode of rupture propagation. Figure 10a shows such a schematic snapshot of strength, velocity, and slip at rupture tip (Heaton, 1990) based on seismic inversions. Figure 10b illustrates similar experimental observations by various runs of quake-mode, typically for run #2782 as an example: the patch strength weakens fast at d=0.01 m with friction dropping from 0.8 to a minimum value of ~0.2, then is followed by strength recovery at d=~1.5 m. Generalizing from 42 experiments on granite, I postulate an ELSE-based friction law that I think is more representative of earthquake (Fig. 10c). This friction law has a small initial hardening that prevents easy generation of large earthquakes, fast weakening approaching seismic rates (1.0 m/s), and a strength recovery after peak velocity with an adjustable Dc and a total slip distance, Dt.

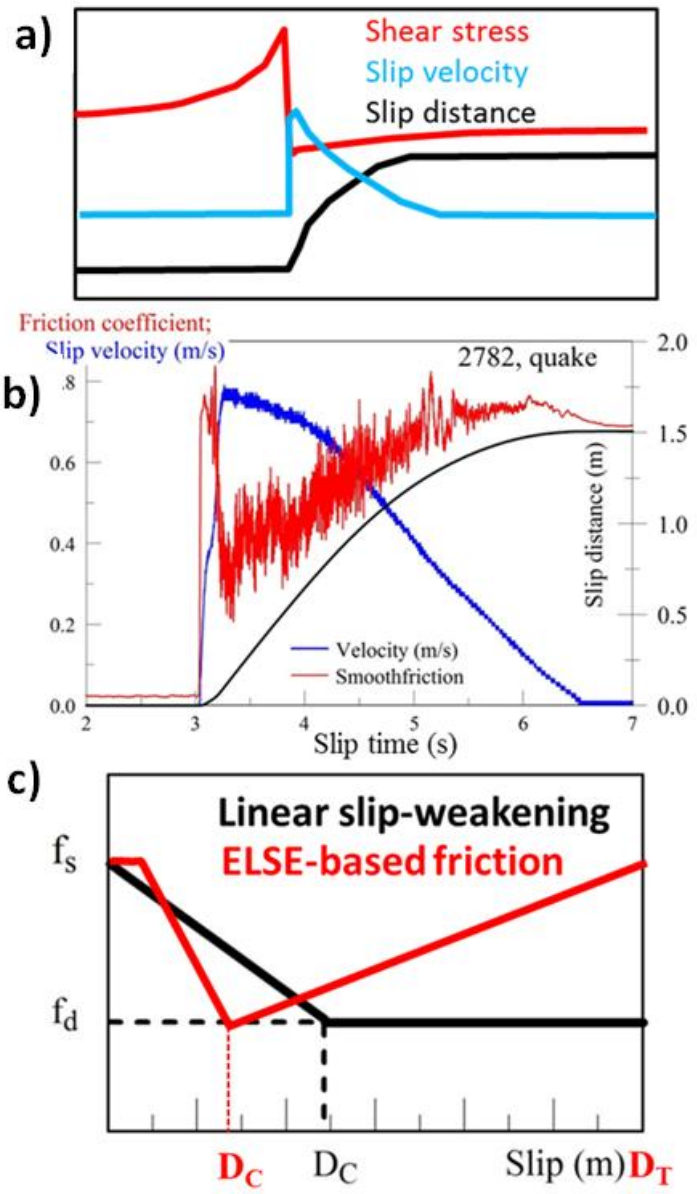


**Figure 10. Earthquake models during fault slipping at a specific point on the fault. (A) Shear stress and slip velocity and slip during a pulse-like earthquake event (adapted from Heaton, 1990). (B) The evolution of frictional stress, slip velocity, and displacement in ELSE experiments under quake loading. (C) New friction law generalized from experiments, ELSE-based Slip and linear slip weakening (LSW).**

## Conclusions

Steady-states experiments were conducted on granite at high slip velocity (up to ~1.0 m/s) and with normal stress of ~1-7MPa. To avoid the limitation of controlled

velocity in steady-state experiments, I tested and compared three sets of experiments at different loading modes and they were conducted at high velocity (~1 m/s) and high normal stress (up to ~30 MPa) on the same rock samples.

1) The evaluation of the steady-state experiments shows that steady-state experiments could help understand the weakening mechanism, however, friction data obtained in this experimental approach is immaterial to rock friction during earthquakes, simply because earthquakes are not a steady-state process.
2) The dissimilarity of friction behavior is attributed solely to the different loading mode, as presented by Fig. 9, yet the physical mechanisms remain to be further explored.
3) I think among the three loading loads, the earthquake-like loading experiments can be better than the others (steady-state and ramp loading) for realistic modeling of earthquake rupture. It presents the fast-accelerated and slow-decelerated behavior of slip velocity, and the weakening-strengthening of shear stress (Fig.10), which better capture the character of earthquake rupture models and comply with the earthquake models.
4) The main advantages of the earthquake-like loading experiments are its analogous to the stick-slip earthquakes with various velocities rather than a controlled steady velocity. I select to focus on the potential of constructing constitutive friction laws from earthquake-like experiments instead of steady-state experiments in later research. I proposed an ELSE-based friction law with further simulation of granite fault presented in Chapter 5.

# Chapter 4:

# Mechanics of Dynamic Shear Rupture

A central objective of my study is the simulation of the dynamic rupture during earthquakes. I emphasize the need to use frictions laws that were derived at high-velocity experiments and particularly, the ELSE experiments (Chapter 1). In this chapter, I outline the formulations of dynamic shear rupturing that were derived and used for earthquake simulations, the previous results, and the present approach.

## Formulation of dynamic shear fracture

This study aims to numerically simulate dynamic ruptures along anti-plane fault (mode III; Fig. 1) by applying high-velocity experimental data. I followed the steps leading to the spectral solution for rupture problem of Geubelle and Rice (1995). The fault is assumed to be unbounded, homogeneous within a linear elastic body of shear modulus μ and shear wave $c_s$. For the coordinate system shown, the governing scalar wave equation is:

$$c_s^2\left(\mu_{z,xx} + \mu_{z,yy}\right) = \mu_{z,tt}$$

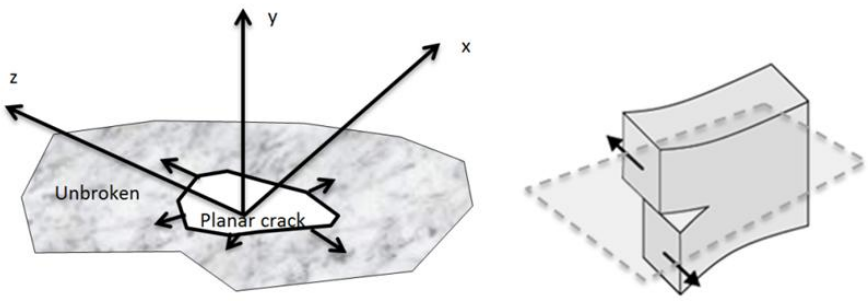


**Figure 1. A schematic presentation of a) planar rupture in Cartesian coordinates and b) anti-plane rupture.**

During anti-plane ruptures, the spectral component of $\mu_z$:

$$\mu_z(x, y, t) = e^{ikx}\Omega(y, t; k)$$

A bounded solution of the wave equation for the upper plane (y>0) have the form:

$$\hat{\mu}_z(x, y, p) = e^{ikx}\widehat{\Omega}_0(p; k)e^{-|k|\alpha_s y}$$

Using the anti-symmetry of the displacement solution with respect to fracture plane, the displacement discontinuity is:

$$\delta(x, t) = \mu_z(x, y = 0^+, t) - \mu_z(x, y = 0^-, t) = 2\mu_z(x, y = 0^+, t)$$

If turning to displacements and tractions on the fracture plane, by defining the displacement Fourier coefficients and application of the linear elastic stress-strain equations, the traction is linked with displacement Fourier coefficients. Through several Fourier transforms, the final elastodynamic relations are yielded between tractions and displacement discontinuities along the fracture plane

$$\dot{\delta}(x,t) = \left(\tau^0(x,t) + f(x,t) - \tau(x,t)\right)/(\frac{\mu}{2c_s})$$

$\tau^0(x,t)$ is the externally generated traction, e.g., incoming stress waves, and f(x, t) is convolution over past history.

The implementation of the spectral formulation begins with domain discretization of the fracture plane. The computation conversion between the spectral and real domains is performed efficiently through the fast Fourier transform (FFT) algorithm. The evolution of each element is completed by a time-stepping scheme. The response function of a single spatial mode is examined to dissociate the imprecisions with the time convolution and time-stepping scheme from the FFT solutions (Morrissey and Geubelle, 1997). Then, a careful investigation of the precision and efficiency of the implementation is conducted to avoid the too large computation load for time-integration and convolution schemes. The procedures for this numerical simulation are shown in the flow-chart (Fig. 2). I followed the implementation of this approach by following the studies of Morrissey and Geubelle (1997), Lapusta et al. (2000) and Ampuero et al. (2002).

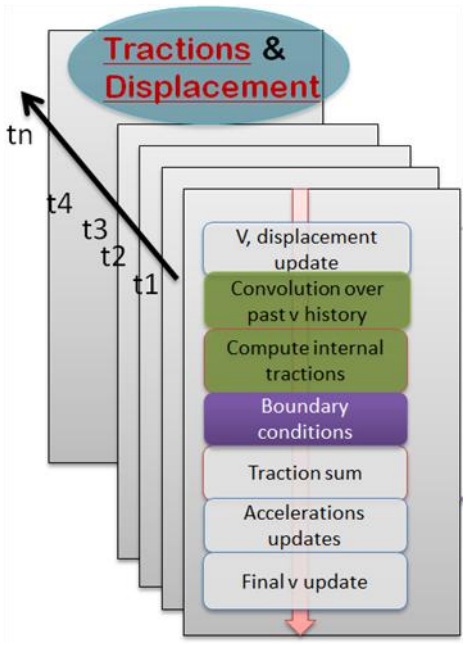


**Figure 2. A flow-chart shows the procedures for solving rupture propagation by spectral method.**

*Friction models for rupture simulations*

A few sets of experimental observations were effectively applied to numerical simulations, and the two most commonly used are slip weakening and RSF as described below.

*Linear slip weakening model*

In the slip-weakening model which was used Ida (1972), the friction coefficient drops from static value, $\mu_S$, to $\mu_K$ after a critical displacement, $D_C$, and then stays constant for unlimited slip distance (Fig. 3a). The friction coefficient, $\mu$, is expressed as:

$$\mu(D) = \begin{cases} \mu_S - \dfrac{(\mu_S - \mu_K) \cdot D}{D_C}, D < D_C \\ \mu_K, D > D_C \end{cases}$$

Slip-weakening model makes the numerical rupture calculation stable while eliminating the singularity in the fracture solution. However, this model ignores the effects of slip rate and state variables (Dieterich, 1979).

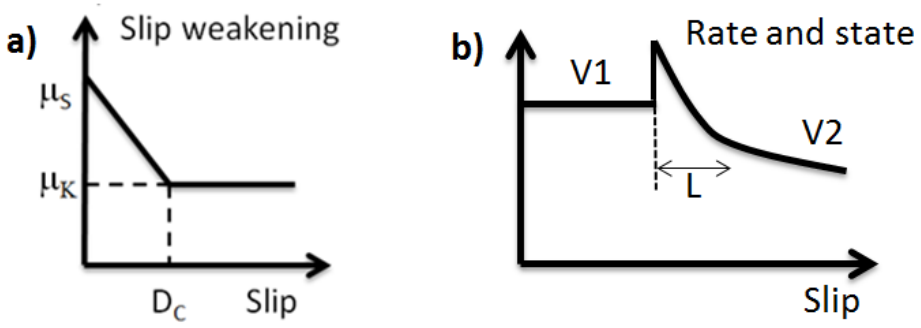


**Figure 3. a) In the slip weakening friction model, friction drops from $\mu_s$ to $\mu_k$ instantly after a slip $D_C$; b) Change in friction due to a sudden increase in sliding velocity in rate- and state- friction model.**

*Rate- and state- friction*

The rate- and state-dependent friction (RSF) law was developed following experimental observations (Dieterich, 1979; Ruina 1983 and followers). Several formulations of this law were developed later and successfully used to ruptures at a shallow fault region (Fig. 3b; Lapusta et al., 2000; Kaneko et al., 2008). RSF with the aging law as the state evolution was formulated by Dieterich (1979) and Ruina (1983) as

$$\mu = \mu_0 + a\, ln\left(\frac{v}{v_0}\right) + b \ln\left(\frac{\theta}{\theta_0}\right)$$

$$\frac{d\theta}{dt} = 1 - v\theta/L$$

where a, b and L are empirical constitutive parameters and θ is a state variable describing the transition between different velocities (steady-state). These relations were generally related to the physics of friction by

1). $a\ ln\left(\frac{v}{v_0}\right)$ represents a resistance similar to viscosity generated by deforming asperities on the sliding surface; and

2). $b \ln\left(\frac{\theta}{\theta_0}\right)$ describes the adhesion (e.g., chemical) between surfaces that is assumed to increase with contac time (aging effect).

Typically, the experimental analyses that led to RSF parameters were conducted in bi-axial direct shear with low slip velocity (up to 0.001 m/s) and limited slip distance (~10mm) (Dieterich, 1979; Marone 1993; Scholz 1998). These values are smaller by orders of magnitude than the equivalent values for in-situ earthquakes (0.1-10 m/s and up to 5 m, respectively).

## Simulation results

In presentation below of previous rupture models focuses of rupture style of crack-mode versus slip-pulse-mode (Fig. 9, Ch. 2), and only briefly refers to other features of the simulations. This focus is an introduction for the results of the present simulations in Ch. 5.

### *Slip-weakening model*

The shear rupture along a vertical fault is commonly selected model for simulation of earthquake rupture along a strike-slip fault, e.g., San Andreas Fault (Day and Dalguer, 2005; SCEC benchmark projects). The rupture propagates spontaneously

under the influence of assumed initial stresses and slides under a specified friction (e.g. slip-weakening) along a fault embedded in a linearly elastic continuum. In these simulations, the friction drops during a breakdown process and then stays at dynamic steady-state (Fig. 3a). The typical initial and boundary conditions (Day and Dalguer, 2005) for the simulations include (Fig. 4):

1) A vertical fault of finite length in the vertical direction and infinitely long along its strike, thus, the simulation is for 2D rupture propagation in an antiplane configuration.
2) A friction law is selected, e.g., linear slip weakening or RSF (Fig. 3).
3) The shear stresses are below the static frictional strength and the central 3 km is pre-set with initial shear stress slightly higher than the static strength to initiate the rupture.
4) Zones of high strength are set to "stop" the rupture.

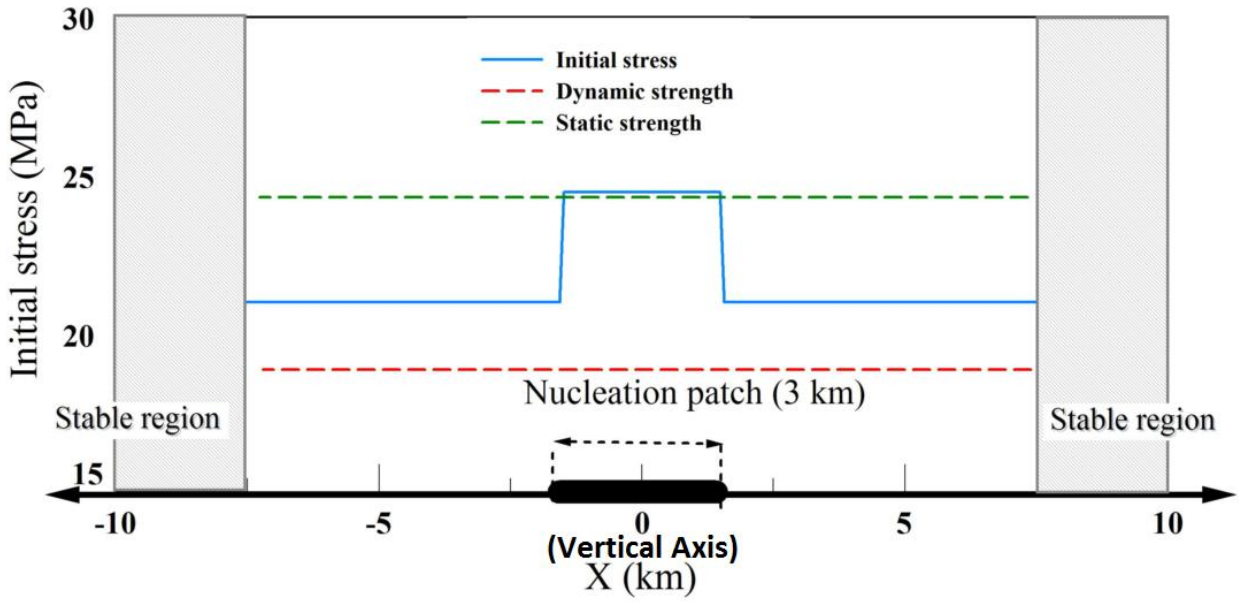


**Figure 4. Profile of stress setting for simulated antiplane fault. The green dash line represents an approximately defined stress above which slip will initiate.**

The fault keeps slipping where slip velocity is above zero until it reaches the boundary after ~8 s (Fig. 5a). Typically, this kind of non-stop rupture propagation at all points along the fault is termed as a crack-like style. In contrast, a slip-pulse exist if the fault strength is low immediately behind the rupture front where slip velocity quickly drops to zero when the strength builds up at finite distance from the front. The cohesive zone, in which the breakdown occurs, is the portion of the fault plane behind the crack tip where the shear stress drops from the static value to the dynamic steady value. The cohesive zone of the anti-plane is a narrow growing trend (Fig. 5b). In this simulation, the slip stops by an artificial barrier introduced by the simulator (e.g., Rojas et al., 2008).

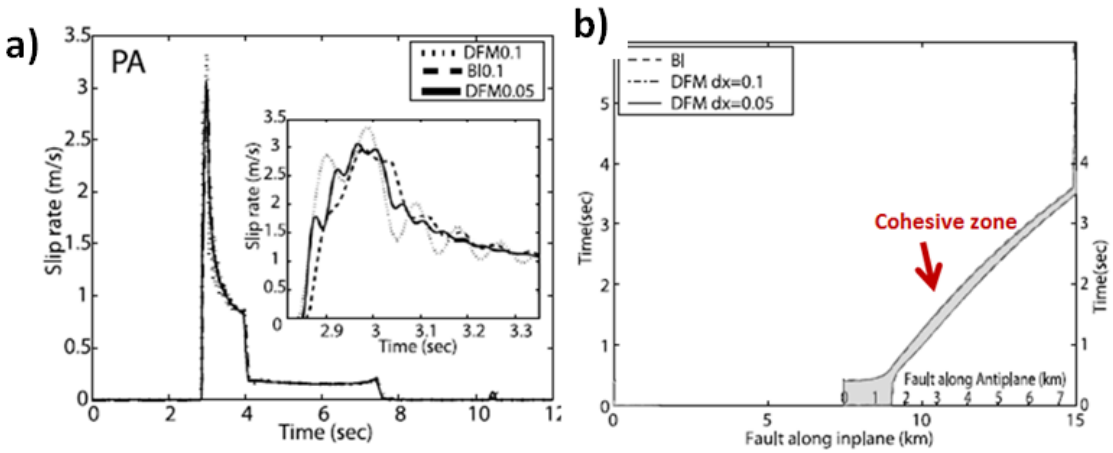


**Figure 5. a) Slip velocity vs slip time at 6 km away from the nucleation center in the antiplane direction; b) cohesive zone along antiplane (adapted from Day and Dalguer, 2005).**

*Rate-based models*

Simulation that led to pulse-like style were derived by Cochard and Madariaga (1994), Perrin et al., (1995), Beeler and Tullis (1996), and again effects, e.g. Okubo (1989) and Ben-Zion and Rice (1997). They used velocity dependent friction to simulate dynamic slip of mode III under uniformly pre-stressed at background loading, $\tau_0^b$, with homogeneous material. The friction constitutive properties are taken as uniform by using rate and state along the fault interface.

Zheng and Rice (1998) systematically discuss the determination of rupture modes. To generate a pulse mode rupturing, they used a condition of under-stressing in which the background loading $\tau_0^b$ is less than the critical stress. The critical stress level, $\tau_{pulse}$, is determined as the maximum value of $\tau_0^b$ that satisfies:

$$\tau_0^b - \frac{\mu}{2c} V \leq \tau_{ss}(V) \qquad \text{for } V \geq 0$$

The rupture solution in the form of self-healing pulse exists only in the low stress range, when $\tau_0^b \leq \tau_{\text{pulse}}$ or $\tau_0^b$ is only slightly greater than$\tau_{\text{pulse}}$. In the other case, a crack rupture mode develops when $\tau_0^b > \tau_{\text{pulse}}$ (Fig. 6). The results indicate that a steadily propagating slip-pulse can exist only for re-strengthening of the fault, e.g., Perrin et al. (1995). Moreover, the relation between velocity-weakening friction (e.g., rate and state dependence) and slip-pulses has been investigated theoretically on an unbounded fault. If natural faults are indeed velocity weakening at seismic slip rates, their analyses suggest that pulse slip indicates conditions of understressed crust (Fig. 6).

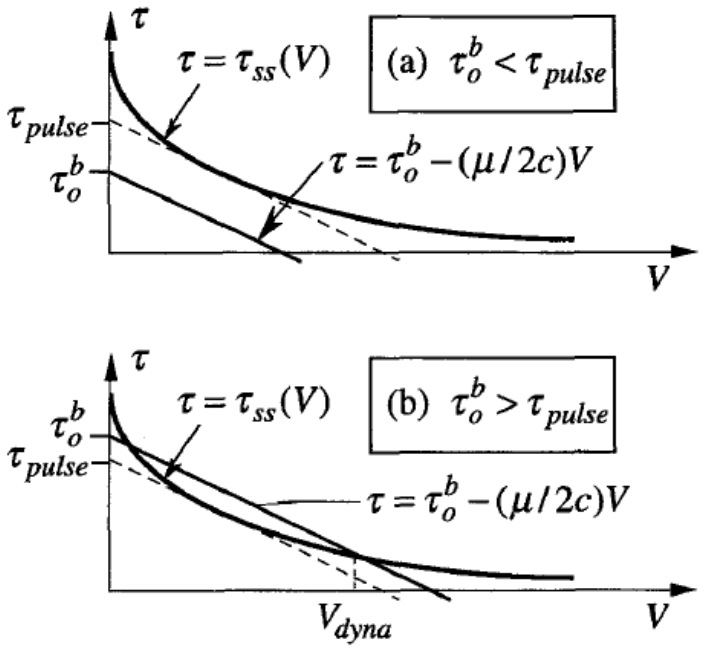


**Figure 6. a) Relative position of the radiation damping line $\tau = \tau_0^b - \frac{\mu}{2c}V$ and the steady-state friction $\tau = \tau_{ss}(V)$for the understressing condition, $\tau_0^b \leq \tau_{pulse}$. (b) Relative position for $\tau_0^b > \tau_{pulse}$ (after Zheng and Rice, 1997).**

*Wrinkle pulse*

Weertman (1980) presented analysis of unstable slippage without requiring for a dislocation propagating between two mechanically dissimilar blocks. The slip occurred with tensile change of normal stress in the slip direction within the more compliant material. Such slippage due to reduced normal stress in the compliant material is analogous to a net shear displacement of a wrinkle in a carpet. The maximum propagation speed could reach the generalized Rayleigh speed. Andrews and Ben-Zion (1997) successfully performed finite different calculations of such wrinkle pulse using a constant coefficient of friction on a fault with different elastic materials of 20% difference in wave speeds. The production of self-sustaining and sharpening wrinkle pulse (Fig. 7 ab) along the more compliant material confirmed the prediction by Weertman (1980) and provides a new way to understand the rupture propagation on mature faults juxtapose different rock bodies; see also (Ben-Zion and Andrews, 1998; Ben-Zion and Shi, 2005).

Anooshehpoor and Brune (1999) experimentally showed the existence of the wrinkle pulse in a pre-stressed fault between two blocks of foam rubber (Fig. 7cd). The particle motions and properties of the observed velocity pules are in agreement with the calculations of Andrews and Ben-Zion (1997). It showed that the self-sustaining pulse propagates in the direction of the slower block and does not die out from radiation damping.

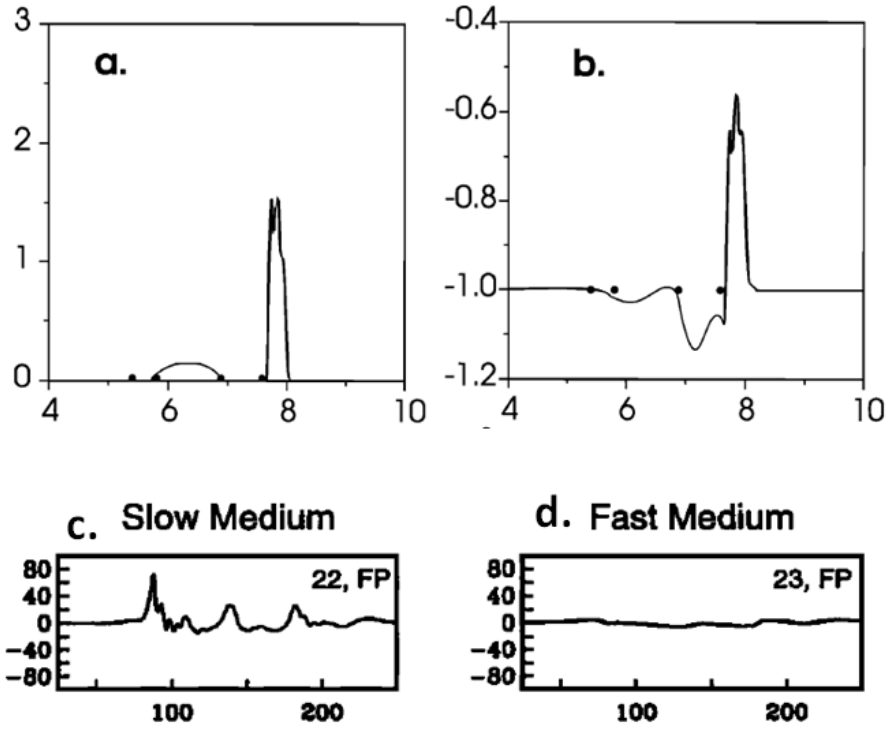


**Figure 7. a) Example of time histories of slip velocity and b) normal traction at x=6 on the fault from the regularized calculation of self-sustaining wrinkle pulse (after Andrews and Ben-Zion, 1997). Dots mark phase arrivals of faster P, slower P, faster S, slower S from an arbitrary chosen point within the initiation region; time histories of particle slip velocity observed in c) slow medium and d) fast medium for a stick-slip event in the foam rubber experiments (after Anooshehpoor and Brune, 1999).**

While bringing a slip weakening instead of constant friction into a dynamic model of heterogeneous initial stress, Andrews and Harris (2005) found that the wrinkle pulse is only a small contributor to the whole rupture propagation. Material contrast may not favor a particular propagation direction in more compliant block for a natural earthquake. Due to the complexity of the parameter-space study of large faults, and the lack of experimental support, the material contrast remains enigmatic. Later, a comprehensive systematic parameter-space study (Shi and Ben-Zion, 2006) of mode II rupture indicated that material contrast with friction drop does result a favored

propagation direction of earthquakes. Although the associated work with broad parameter space can exhibit a diversity of phenomena, some observed features of San Andreas system (Rubin and Gillard, 2000) were related the wrinkle pulse. Extending from this issue, further work has been initiated to characterize the properties of wrinkle pulse, e.g., Ben-Zion and Shi (2005) showed the stabilizing effect by the off-fault yielding, and Xu and Ben-Zion (2012a, b) explains the shapes and patterns of the yield zones. Another effort has been devoted to the simulation of biomaterial fault governed by a more complicated friction, e.g., velocity-weakening (Ampuero and Ben-Zion, 2008). It characterized the range of velocity-weakening scales and initiation conditions that determined several symmetry properties of the ruptures.

*Other pulse mechanisms*

Day (1982) and Johnson (1992) presented slip-pulse behavior in numerical elastodynamic rupture simulations with constant friction drop and at the presence of long narrow region of unbreakable barriers to confine the rupture process. Without these barriers, the formulation would lead to a crack mode of rupturing. They deduced that the two slip-pulses as the result of effectively relock of the fault behind the rupture front by the barriers. Perrin et al. (1995) also illustrated such barrier-based mechanism of pulses in a case that otherwise would result in crack rupture. As explained in Zheng and Rice (1998), other mechanisms of self-healing pulse could exist and involve friction properties, geometric setting of faults, as well as dissimilarity of elastic properties of the material. It is important to learn more about the characteristics of each.

## Evaluations of rupture simulations

Aforementioned analyses investigated relevant aspects of slip-pulse, e.g., properties of pulse, mechanism of pulse, and importance of pulse during earthquakes. The studies of winkle pulse (e.g., Andrew and Ben-Zion, 1997; Ben-Zion and Shi, 2005) well characterize the existence and properties of winkle pulse in biomaterial faults. As indicated by Andrews and Harris (2005), however, the wrinkle pulse appears as only a part of the predominantly crack solution. Instead of the argument "Is the winkle-like slip-pulse important in earthquake simulation" by Andrew and Harris (2005), it turns out more proper to identify the role of winkle pulse during the earthquake. The comprehensive systematic parameter-space study (Ben-Zion and Shi, 2005; Shi and Ben-Zion, 2006; Ampuero and Ben-Zion, 2008) indicates clearly the material contrast with friction drop could produce favored propagation direction of earthquakes in the more compliant material during mode II rupturing. Results also show that the winkle pulse tends to evolve with propagation distance etc., while still several issues remain to explore:

I. Is there is a dominant rupture mode in addition to the directivity by winkle pulse?
II. Could the pulse rupture occur within the homogeneous elastic material?
III. What is the rupture process of natural earthquakes in conditions of friction drop rather than tensile change of normal stress?

Zheng and Rice (1998) and Ampuero and Ben-Zion (2008) simulated faults governed by a more complicated friction, e.g., velocity-weakening and determined several important aspect of the occurrence of pulse ruptures. Ampuero and Ben-Zion (2008) emphasized the effect of material contrast while Zheng and Rice (1998)

analyzed for more basically the intrinsic reason determined by friction law. The understressed condition has been well proposed to produce a dominate slip-pulse within homogeneous media with a preassumed velocity weakening model (Zheng and Rice, 1998) and this answers the questions II and III. Some conditions have been discussed by Cochard and Madariaga (1994), Perrin et al. (1995), and Zheng and Rice (1998) in which slip pulses can be captured, however, with either unrealistic parameters selection for friction or friction laws from too low-speed experiments. Overall the theoretical work further indicated and confirmed the importance of considering the dynamic friction behavior on the interface of faults that might control the rupture modes of natural earthquake.

# Chapter 5:

# Shear rupture along a fault with an experimentally- determined frictional strength

I simulate the dynamic shear rupture along a vertical, strike-slip fault in an elastic half-space. The fault has the frictional strength properties that were determined experimentally on Sierra White granite samples that were loaded by a massive flywheel. This loading style closely simulates the loading of a fault patch during an earthquake, and it was termed Earthquake-Like-Slip Event (ELSE) by Chang et al. (2012). Their experiments revealed systematic alteration between slip-weakening and slip-strengthening that resemble the expected behavior during slip-pulse propagation. Based on slip distances, Chang et al. (2012) considered their experimental results as proxies of fault-patch behavior during earthquakes of magnitude M = 4 - 8. I used the friction-distance relations of these experiments to form an empirical slip-dependent friction model, referred to as ELSE-model. For the dynamic rupture simulation, I used a 2D spectral boundary integral element method that was designed for anti-plane (mode III) shear fracture problems (Ampuero, 2002). To facilitate comparison of ELSE-model results with published models, the calculations were conducted for a crust with mechanical properties and stress state of Version 3 benchmark of SCEC (Harris et al., 2004).

The rupture simulations with a fault of ELSE-model friction law revealed a few significant features: (1) Rupture propagation in a slip-pulse style in which the slip velocity with the cessation of slip behind the slip-pulse; (2) Systematic decrease of slip

distance away from the nucleation zone; and (3) Spontaneous arrest of the dynamic rupture without requiring artificial insertion of a barrier. These features together suggest a rupture of a self-healing slip-pulse mode. These results differ from the rupture model calculated for a fault with linear slip-weakening friction (Rojas et al., 2008) that generates a crack-like rupture that does not arrest spontaneously. I deduce that the slip-pulse in our simulation results from the fast recovery of shear strength as observed in ELSE experiments, and argue that incorporating this experimental-based friction model to rupture modeling produces realistic propagation of earthquake rupture.

## Introduction

The spontaneously propagating shear rupture in a stressed crust is an effective idealization of natural earthquakes (Day and Dalguer, 2005). The rupture simulation requires accurate and efficient numerical procedures that accounts for constitutive laws on the discontinuity surface embedded within a linear, elastic continuum (Kaneko et al., 2008). Various numerical schemes have been developed and validated for such dynamic ruptures, including finite difference, boundary integral method, and spectral elements method (Andrews, 1976; Geubelle and Rice, 1995; Madariaga et al., 1998; Lapusta et al., 2000; Day and Dalguer, 2005; Ben-Zion and Shi, 2005; Ampuero et al., 2008; Kaneko et al., 2008). Typically, the solutions are given in terms of the slip and evolving stress over a fault as the rupture progresses, which depend upon numerical solvers for the elastic motion in the continuum and frictional laws along the fault plane (Rojas et al., 2008). The basic friction law of the rupturing fault is a linear slip-weakening model for the breakdown process, during which the friction drops from a static value at the

initiation of slip to a kinetic value when slip displacement exceeds a critical value, Dc (Ida, 1972; Andrews, 1976; Day and Dalguer, 2005). This slip-weakening model yield stable rupture calculation, however, it ignores the significant effects of dynamic friction that shows dependence on slip rate and various state variables, e.g., temperature (Dieterich 1979).

The rate- and state-dependent friction (RSF) laws were developed to address these dynamic effects following experimental observations (Dieterich, 1979; Ruina 1983). In some cases the RSF laws have been successfully applied to simulate rupturing of shallow faults (Lapusta et al., 2000; Kaneko et al., 2008). A central difficulty with RSF friction laws is that its empirical parameters were derived in experiments conducted in bi-axial direct shear with low slip velocity ($10^{-7}$ to $10^{-3}$ m/s) and limited slip distance ($10^{-5}$ – $10^{-2}$ m) (Dieterich, 1979) that are significantly small than those of typical earthquakes (velocity of 0.1-10 m/s,  and slip distances of meters).

The central contribution here is the application of an experimentally-based constitutive friction model that was determined at earthquake-like conditions (Ch. 3). The experimental analyses were conducted in rotary shear apparatus, simulating "earthquake-like slip event" (ELSE), at slip velocity (up to 1.0 m/s) and normal stresses of up to 30 MPa (Chang et al., 2012). These slip velocities and displacements approach those of typical earthquakes (0.1-10m/s and up to 5 m, respectively). The experimental observations revealed a systematic dynamic-weakening (Fig. 1, Chang et al., 2012), which was attributed to powder lubrication at elevated velocities (Reches and Lockner, 2010; Sammis et al., 2011).

I define the frictional relations of ELSE experiments (Chang et. al., 2012) as ELSE-model, and apply this model to 2D rupture propagation. I compare the solutions of two friction models, the Linear Slip-weakening and ELSE-based Slip for insight of the rupture process. A spectral boundary integral element method (SBIEM) has been used to investigate spontaneous propagation of ruptures in elastic media. The formulation is based on an exact spectral representation of the elastodynamic relations including tractions, slip velocity, and displacement discontinuities along the fault plane (Geubelle and Rice, 1995; Morrissey and Geubelle, 1997).

## Friction models

The slip-weakening model (Fig. 2) was extensively applied in rupture simulation since Ida (1972). The model assumes that the friction coefficient, $\mu$ (D), is a function of slip distance, and it drops from static value, $\mu_S$, to $\mu_K$ after a critical distance, $D_C$, and then remains constant,

$$\mu(D) = \begin{cases} \mu_S - \frac{(\mu_S - \mu_K)\cdot D}{D_C}, D < D_C \\ \mu_K, D > D_C \end{cases} \quad (1)$$

As discussed in Ch. 3, the ELSE-based Slip model was developed from Sierra White granite experiments at impact loading of velocity up to 1 m/s and under normal stress up to 32 MPa (Chang et al., 2012; Ch. 3). The most significant observation of the ELSE experiments is the fast weakening at d=~0.0045-0.001 m with friction drop (Fig. 1), followed by strengthening after a certain amount of slip. For example, in the typical run #733 (Fig. 1d), there is a briefly drop of patch strength from 0.69 to a minimum value of ~0.35, and then a strength recovery after a slip distance of 0.1 m. Similar patterns of strength evolution were observed for ELSE-based experiments (Fig. 1abc): 1)

High initial shear stress decreases as slip initiated; 2) After the strength reaches lowest value, the patch were re-strengthened. I refer this feature as ELSE-based weakening-strengthening and a numerical model has been developed to describe this character. The numerical relations are based on an assumption that the friction coefficients can be presented as dependent of the slip distance (Ida, 1972; Andrews, 1976; Day and Dalguer, 2005); 2), There could be different physical mechanisms controlling the stage of fast weakening mode before critical slip distance $D_C$, and the stage of strengthening after $D_C$. These mechanisms remain enigmatic though the features are observed and confirmed by Sone and Shimamoto (2009) and Chang et al. (2012).

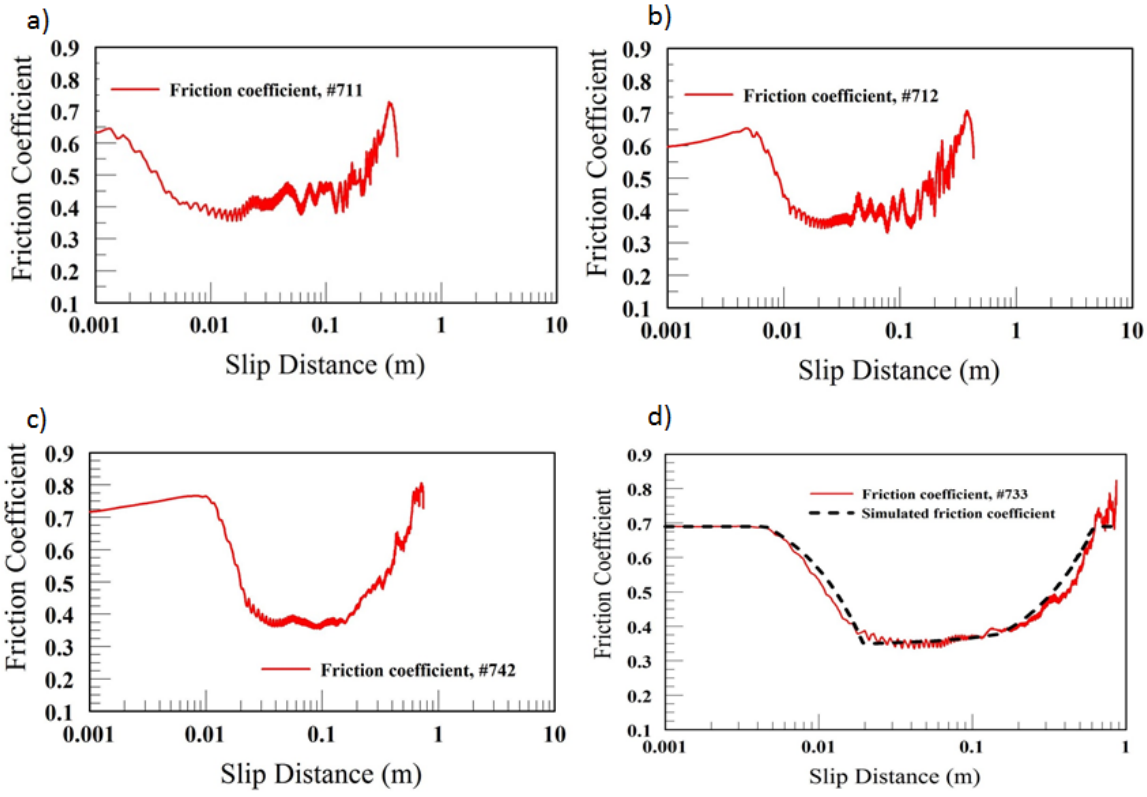


**Figure 1. The evolution of frictional strength in ELSE experiments with respect to slip distance a) experiment #711; b) experiment #712; c) experiment #742; d) the selected experiment #733 for rupture simulation with a black dash fitting line. Note all are in log plot.**

Following the above assumptions, the simplified form of the ELSE-model friction coefficient, $\mu_e$ (D), is,

$$\mu_e(D) = \begin{cases} 0.69, \ D \leq 0.0045 \\ 0.69 - \frac{0.34}{D_C - 0.0045} * (D - 0.0045), \ 0.0045 < D \leq D_C \\ 0.35 + \frac{0.34}{D_T - D_C} * (D - D_C), \ D_C < D \leq D_T \\ 0.69, 0.65 < D_T \end{cases} \quad (2)$$

This formulation linearizes the actual experimental results (Fig. 1) for simple relations that capture the main features of experimental results: (1) initial hardening (D= 0.0045-0.001 m), replaced by a constant friction value; (2) short weakening stage (Dc = 0.005-0.02 m); and (3) strengthening stage to the final stop at $D_T$. By adapting the experimental based relation to a more applicable formulation, the governing equation of friction coefficient is expressed as (Fig. 2):

$$\mu_e(D) = \frac{\mu_e(D) - 0.35}{0.34} \left(\mu_S - \mu_K\right) + \mu_K \quad (3)$$

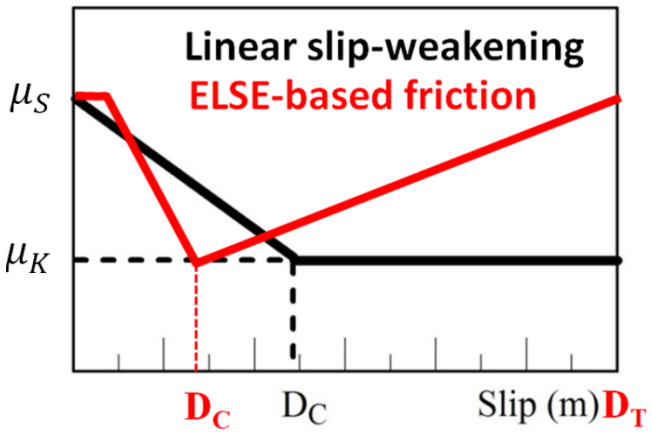


**Figure 2. A schematic presentation of linear slip-weakening (black) and ELSE-based Slip model (red).**

## Numerical calculations

Following Morrissey and Geubelle (1997), I consider a homogeneous, linear elastic continuum with a Cartesian co-ordinate system *y=0*, the elastodynamic relations between tractions and displacement discontinuities on the fault plane, can be expressed as:

$$\tau(x,t) = \tau^0(x,t) - \frac{\mu}{2c}V(x,t) + f(x,t) \quad (4)$$

In which $\tau(x,t)$ is the stress on the fault plane, $\tau^0(x,t)$ is the externally incoming stress, μ is the shear modulus, *c* is the shear wave speed, $V(x,t)$ is the slip velocity, and $f(x,t)$ is the single convolutional function of elastodynamic response. The details of the solution procedure are given in Morrissey and Geubelle (1997). The numerical implementation of boundary integral method has been widely used to investigate spontaneous ruptures in elastic continuum (e.g., Andrews, 1985; Geubelle and Rice, 1995; Lapusta et al., 2000). In this paper, a 2-D mode III elastodynamic spectral formulation is selected to simulate the anti-plane shear ruptures in an infinite body. The main idea of the simulation is to confine the slip and evolving stress on the fault plane as the rupture progresses, expressing the elastodynamic response of the elastic continuum in terms of integral relationships of displacement and tractions (Day and Dalguer, 2005). The convolutions kernel in space and time is provided and validated to eliminate the necessity to simulate the wave propagation through elastic continuum by assuming an infinite, uniform elastic solid (Morrissey and Geubelle, 1997). In advance of this numerical scheme, the rupture problem becomes computationally intensive, precise and flexible. Recently this method has been used and

discussed to simulate crack propagations using slip-weakening or rate- and state-dependent friction laws (e.g., Lapusta et al., 2000).

In this research, I use the SBIEM to apply the ELSE-based Slip for spontaneous propagation of rupture problem. The fault is assumed to be embedded in a homogeneous and infinite medium. The parameters of the test case correspond to Version 3 of the Southern California Earthquake Center (SCEC) benchmark problem proposed by Harris et al. (2004). The P wave velocity is 6 km/s, shear wave velocity is 3.464 km/s, and the density is 2,670 kg/$m^3$. The rupture geometry is shown schematically by the 2-D fault model (Fig. 3), and it allows the rupture propagating within 15 km in the x direction with several monitoring points. The selected initial stress state and frictional properties are listed in Table 1. I present two basic cases computed a SBIEM solution. In case 1, I integrated ELSE-based Slip, and compared the results with a SBIEM solution with Linear Slip-weakening, while keeping all other parameters the same. In case 2, in order to make the SBIEM compatible with longer seismic slip ($D_C$=0.5m and $D_T$=1.5 m), I increase the critical slip for both friction models while keeping other parameters the same as in case 1.

**Table 1. Stress and friction parameters for two test problems**

| Parameters | Nucleation patch | Outside nucleation | Outside fault |
|---|---|---|---|
| Initial shear stress $\tau_{0,}$ MPa | 81.6 | 70.0 | 70.0 |
| Initial normal stress $-\sigma_{n,}$ MPa | 120.0 | 120.0 | 120.0 |
| Static friction coefficient $\mu_s$ | 0.677 | 0.677 | Infinite |
| Dynamic friction coefficient $\mu_K$ | 0.525 | 0.525 | 0.525 |
| Static yielding stress $\tau_s=-\mu_s\sigma_n$, MPa | 81.24 | 81.24 | Infinite |
| Dynamic yielding stress $\tau_d=-\mu_K\sigma_n$, MPa | 63.0 | 63.0 | 63.0 |
| Dynamic stress drop $\Delta\tau=\tau_0-\tau_K$, MPa | 18.6 | 7.0 | 7.0 |
| Strength excess $\tau_s-\tau_0$, MPa | -0.36 | 11.24 | Infinite |
| Critical slip distance $D_C$, m | 0.0195 (case 1)<br>0.5 (case 2) | 0.0195 (case 1)<br>0.5 (case 2) | 0.0195(case 1)<br>0.5 (case 2) |

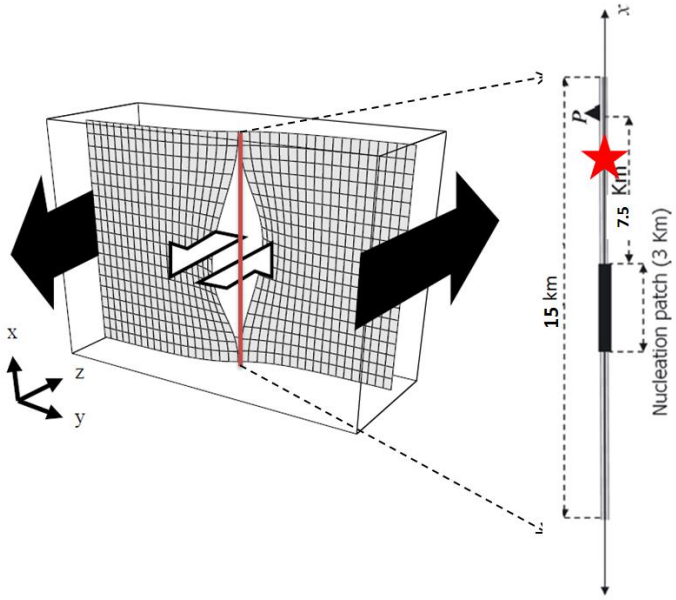


**Figure 3. A homogeneous and infinite elastic medium for anti-plane faulting (after Ampuero et al., 2000) and a 2-D fault model for testing spontaneous rupture propagation with monitoring points marked as red stars.**

## Results

The results of two cases are presented. Andrews (2004) pointed out that the laboratory evidence shows "$D_C$ scales with the wavelength of geometric irregularities of the rupture surface (Ohnaka and Shen, 1999; Ohnaka, 2003). Therefore $D_C$ is expected to be larger for larger ruptures, as longer-wave-length irregularities become important." Case 1 is for SBIEM calculations with short critical slip distance as input for Linear Slip-weakening and ELSE-based Slip. Case 2 is for longer critical slip distance for investigation of larger earthquakes. The time histories of slip velocity, slip and shear stress for two friction models (linear and ELSE) are compared and analyzed.

*Case 1: Short critical slip distance*

The time histories of case 1 (Figs 4) correspond to the simulation results at a point 6.0 km away from the center of the nucleation patch (Fig. 3). The results are the direct outputs without filtering. The time histories in Fig. 4a displays the initiation, evolution and stopping of the shear stress, slip velocity, and the slip distance for rupture along a fault with Linear Slip-weakening (the same model as in Rojas et al., 2008; Day and Dalguer, 2005). In comparison, the ELSE-based Slip (Fig. 4b) with the same setting (Table 1) shows later arrival time of the rupture, the peak slip velocity is slightly lower, and the shear stress is lower (~2MPa). Further, the velocity in ELSE model drops fast in the end due to recovery of strength after ~1.5 s, resulting in a shorter slip distance. Most importantly, the ELSE model shows much shorter travel time for velocity than the Linear Slip-weakening model.

Fig. 5 presents the calculated slip velocity histories for five monitoring points along the fault away from the nucleation center. Fig. 5a displays the increasing peak velocity for Linear Slip-weakening model, while Fig. 5b shows similar trend with slightly higher peak velocities inside the nucleation patch and slightly lower peak velocity outside. The ELSE-based Slip shows slightly later rupture arrivals. As some critical slip distances of earthquakes are exceeding the experimental slip limitation, I further explore the rupture propagation at a longer critical slip distance in case 2 below.

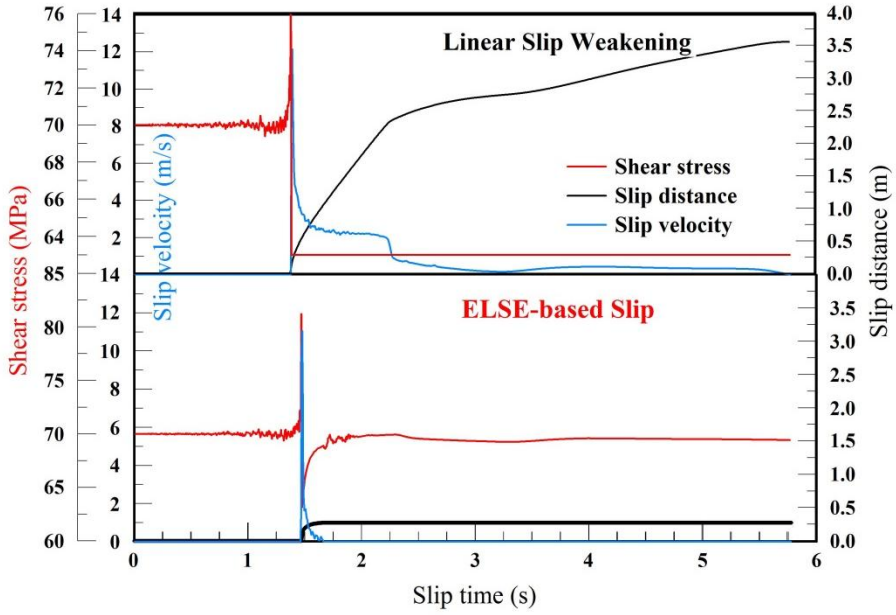


**Figure 4. Time histories of slip velocity, slip distance, and shear stress at the fault plane (6.0 km). Solutions are for SBIEM by a) Linear Slip-weakening and b) ELSE-based Slip, case 1.**

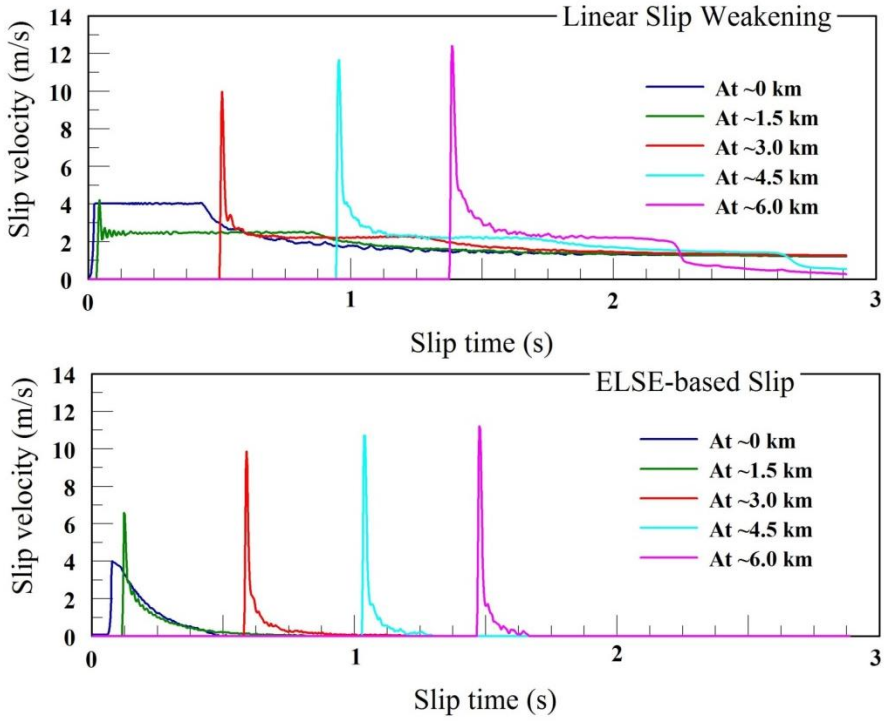


**Figure 5. Time series of slip velocities at various points at the fault plane. a), Solutions by Linear Slip-weakening compared with b) ELSE-based Slip results, case 1.**

*Case 2: Long critical slip distance*

Chang et al. (2012) illustrates the importance of critical slip distance as a parameter in scaling the mechanism of cohesive-zone of earthquake. In light of investigating larger earthquakes, I propose a longer critical slip distance that better fit seismic observations. Values of $D_C$=0.5m, and $D_T$=1.5m, which are similar to the values suggested by Tinti et al. (2005), were used for case 2. The results are the direct outputs from Linear Slip-weakening based SBIEM and ELSE-based without filtering for the same monitoring point at 6.0 km (Fig. 6).

In case 2, both the Linear Slip-weakening and ELSE-based Slip produces different slip patterns. Compared with Linear Slip-weakening based results from case 1 (Fig. 4a), time histories of case 2 (Fig. 6a) has the same general slip pattern but with later arrival time, lower peak slip velocity, and lower shear stress. The final slip distances are the same in two Dc cases for linear slip weakening model. For ELSE-based results, Fig. 7 presents a much smother process of slipping than the one in Case 1. At the point 6.0 km, the frictional strength gets increasing and then weakening much slower after rupture arrives. During the initiation, the slip velocity behaves as a smooth pulse rather than a spike and then decrease gently along with the strength recovery. A longer slip distance is illustrated compared with Case 1 (Fig. 4b).

More results are presented for the histories of slip velocity at various monitoring points by Fig. 7. The most striking features of the comparison between slip-weakening based and ELSE-based results are 1) the systematically occurrence of slip-pulses and 2) the decreasing trend of peak slip velocity in ELSE-based results. Further discussion of implication of such typical features is in next section.

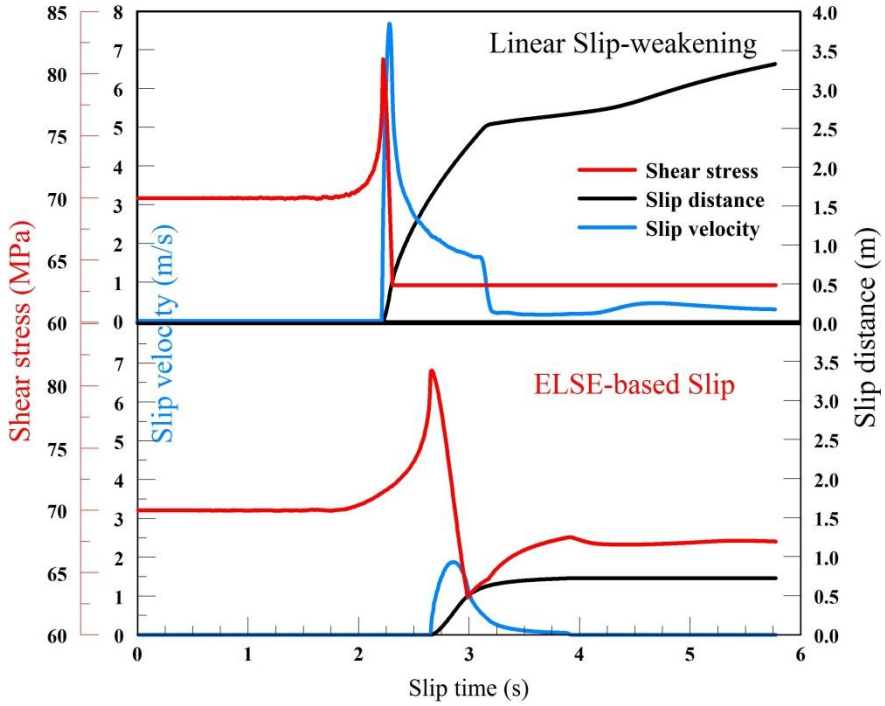


**Figure 6. Time histories of slip velocity, slip distance, and shear stress at the fault plane (6.0 km). Solutions are for SBIEM by a) Linear Slip-weakening and b)ELSE-based Slip, case 2.**

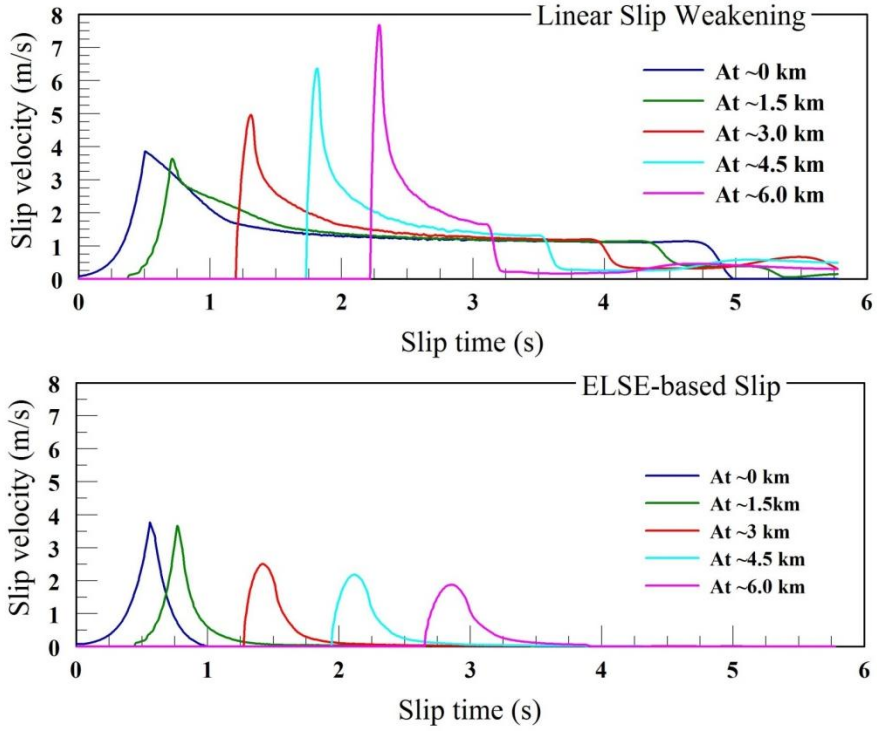


**Figure 7. Time series of slip velocities at various points at the fault plane. a), Solutions by linear slip-weakening compared with b) ELSE-based Slip results, case 2.**

*Summary of the results*

As shown above, the spectral element method has been successfully incorporated with the experimentally determined friction model of ELSE. This implementation reveals two main important observations. First, as the ELSE-based Slip includes both slip-weakening and slip-strengthening (Chang et al., 2012), it naturally simulate a slip-pulse rupture mode (Fig. 6b). Secondly, for this friction model it is not necessary to arbitrarily impose strong barriers to stop the slip. The decay of slip velocity and slip distance away from the nucleation area (Fig. 7) suggests spontaneous stop of the rupture.

I interpret the agreements and differences between applying Linear Slip-weakening and ELSE-based Slip for rupture propagation, specifically studying the evolutions of slip velocity, slip distance, and shear stress. The important features illustrated by ELSE-based friction model can be summarized as: 1) Later rupture arrivals; 2) Fast drop of slip velocity and recovery of shear strength; 3) pulse-pattern of slip velocity; and 4) decreasing trend of peak slip velocity in case of long DC. All these features occur throughout the fault plane. By comparing the responses with linear slip weakening model, it allows to find the effects of dynamic-friction on the rupture propagation. Slightly longer initiation in ELSE-based slip delays the stress drop, thus resulting later rupturing (Fig. 4b). The slip velocity drops quickly due to the recovery of shear strength, which is possibly an effect of slip strengthening. Additionally, the drop of velocity produces the shorter slip distance.

## Discussion

### *Crack or pulse*

I consider the simulation results of rise-drop of slip velocity as important characteristics for slip-pulse relatively to the crack mode produced by linear slip weakening friction laws. By comparing Figs. 6a and 6b, with shear rupture initiated the shear stress for ELSE-based is recovered approaching the initial state while in Linear Slip-weakening, the stress is keeping at very low value. This response is expected to occur in cases of friction model with a transition between weakening and strengthening. As shown in Figs. 5 and 7, I verified that the histories of velocity show pulse-like response as ELSE-based results suggested. This conclusion is consistent with the

observations that the pulse mode of rupture occurs in nature (Heaton, 1990) and the hypothesis by Zheng and Rice (1998) that "a pulse may exist if the fault strength is low immediately behind the rupture front and builds up quickly at finite distance from the front". I extrapolated the slip distribution along the fault upon variable values of Dc for both friction laws, and found slip-pulse with gradually diminishing amount of slip (ELSE-based results) and crack mode with large and fast decreasing slip distribution (Fig. 8). I consider the diminishing amount of pulse-alike slip as a result of weakening followed by strength recovery. The strength recovery heals the fault behind the outward transmitting slipping pulses.

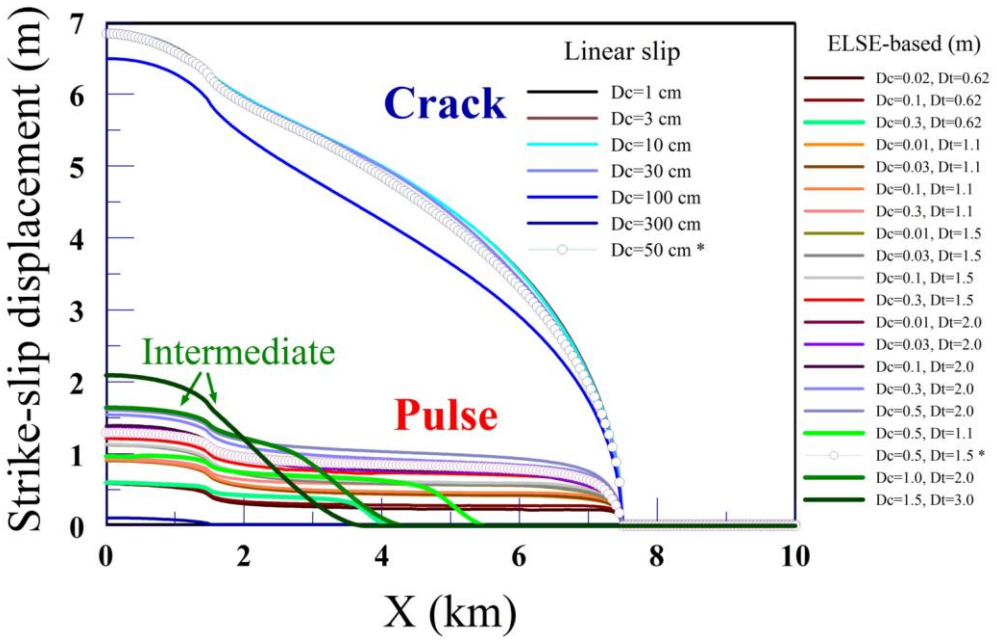


**Figure 8. Slip histories of a) peak slip distance and b) peak velocity along a fault under a uniform setting with short critical slip distance for Linear Slip-weakening; Slip histories of c) peak slip distance and d) peak velocity along a fault under a uniform setting with short critical slip distance for ELSE-based Slip.**

*Discretization and stability*

The stability of steady-state frictional sliding is generically investigated by a critical length scale as discussed by Ampuero (2002). The instability involves a critical size, h*, which can be obtained (personal communication) by,

$$h^* \approx \frac{\pi \mu D_C}{\tau_n(\mu_s - \mu_d)} \tag{5}$$

$$\Delta t = \beta \Delta x / c \tag{6}$$

In which μ is shear modulus, $\tau_n(\mu_s - \mu_d)$is an expression restricted to the stress drop, and $D_C$ is regarded as critical slip distance. This method is to make the element size h smaller than the critical size h*, thus to insure the perturbation on a single cell is only a part of larger space segment. I take this concept by considering a maximum solution of h* as 75 m for Dc=0.00195 and 2000 m for Dc=0.5 m. The cell size is selected as 13.5m in this study and the model produces stable results. Our computation shows that the histories of velocity converge to each other through changing the grid sizes qualitatively. For the time resolution, I use $\beta_{min}$=0.5 and the time step, $\Delta t$, is determined by Eq. 6. The time step is 0.0113 s is selected so that slip in a time step does not exceed a fraction of the characteristic slip distance determined by ELSE-based critical slip distance Dc. The exact critical size at extreme cases has been computed and discussed in Dascalu et al. (2000).

## Conclusions

A spectral element numerical scheme (SBIEM) has been integrated with two friction models, Linear Slip-weakening and ELSE-based Slip, to solve the SCEC test problem of spontaneous rupture. Our results demonstrate:

1) The ELSE-based Slip from the earthquake-alike friction experiments over the range of observed natural seismic slip rates has been successfully applied to simulations of earthquake ruptures. This friction law could reveal fault-patch behavior during earthquakes of magnitude M = 4 – 8 (Chang et al., 2012).
2) The rupture simulations with a fault of ELSE-model friction law revealed a slip-pulse mode of rupture propagation. These results differ from the rupture model calculated for a fault with linear slip-weakening friction (Rojas et al., 2008) that generates a crack-like rupture.
3) A few significant features from ELSE-based simulation support the hypothesis of slip-pulse is by Zheng and Rice (1998) that "a pulse may exist if the fault strength is low immediately behind the rupture front and builds up quickly at finite distance from the front".
4) Spontaneous arrest of the dynamic rupture presents the possibility of the fault to stop without requiring artificial insertion of barriers.

As an approach tending to incorporate experimentally-based friction, this study captures qualitative results and provides a link between experimental work and numerical simulation. I argue that incorporating this experimental-based friction model to rupture modeling produces realistic propagation of earthquake rupture. However, accounting for the rich behavior at different critical slip distances, further interpret work with real earthquake can be crucial to the success of reasonable and rational outcomes. The limitations of the scheme and simplified implementation require future work to consider more explicitly the dynamic response of frictional sliding to the strength recovery.

# Chapter 6:

# Seismic and experimental analyses of fault structure and associated fractures, Anadarko basin, Oklahoma

Sub-seismic fractures critically control gas production in the Woodford Shale unit, Anadarko basin, Oklahoma. To determine these fractures, I analyze the fault/fracture system within the Woodford Shale by integrating seismic attributes analyses and an analog laboratory model. The study area is covered by a 3D seismic survey provided by CGG, with 360 $mi^2$ in size, in central-west of Oklahoma. The analysis focuses on a 20 mi long, north-south fault that is interpreted as a large, strike slip fault.

I used wet clay experiments to identify and analyze the evolution of the associated structures with a strike slip fault, including Riedel shears, splay shears and P shears. The geometry of these secondary faults are used as proxies for the in-situ fault in the 3D seismic survey volume. I applied three attributes (coherence, dip-azimuth, and curvature) to illuminate the fault system, and identify two types of associated structures with high intensity of fractures for potential horizontal drilling: (1) fault systems that are similar to the clay experiments that were revealed in coherence maps; and (2) anticlinal folds that were detected in curvature maps. I conclude that combining attribute analysis and experimental observations strengthens the identification of this striking slip fault-zone in Woodford Shale.

## Introduction

The unconventional reservoirs of the Devonian Woodford Shale in Central-West Oklahoma (Fig.1), has produced dry gas, condensate, and oil within a thickness of ~200 ft (Cardott and Lambert, 1982; Comer, 2008). While hydraulic fracturing along with horizontal drilling, have revolutionized development of Woodford Shale plays (Abousleiman et al., 2007; Waters et al., 2009; Brada, 2011), the natural fracture systems strongly affect the production efficiency in such reservoirs. Indeed, many operators believe hydraulic fracturing reactivates previously cemented natural fractures or otherwise sealed zones of weakness. For this reason, characterization of these natural fractures is of particular interest for the ongoing exploration and drilling design.

The Woodford Shale exhibits heterogeneous lithological features and complex structure (Portas-Arroyal, 2009). In this study, I characterize a fault/fracture system by application of seismic attributes (Marfurt and Rich, 2010) and clay modeling (Reches, 1988) to understand the relations between stratigraphy and mesostructures (Busetti, 2009). I focus on a specific strike slip fault that displays a complex pattern of secondary faults and folds. Although the complexity of strike slip faults was previously studied in mechanical and experimental analyses (Naylor et al, 1986; Reches, 1988), the recent availability of seismic observations provides a new opportunity to interpret such fault-zones in the subsurface.

The main objective is to investigate the major features of a subsurface strike slip fault, to better understand fault structure within the Woodford Shale, and to identify potential area of high intensity of fractures for horizontal drilling and design of hydrofracturing.

## Study area

The Devonian Woodford Shale was deposited in the Anadarko-Arkoma-Ardmore Basins, central USA (Cardott, 2008; Paxton et. al., 2006) covered by an epeiric sea during global sea-level transgression (Lambert, 1993; Johnson, 1988). The study area is in Central-West Oklahoma (Fig. 1). Core analyses indicate that the Woodford Shale is a laminated, organic-rich shale with alternating brittle and ductile layers (Slatt et al., 2010). The brittle layers, which are rich in quartz and calcite, typically fail by jointing that are predominantly perpendicular to bedding. The ductile layers, which are rich in clay and organic carbon, typically fail by shear flow under high stresses.

Fig. 2a shows a time structure through the seismic coherence volume at the Woodford Shale level. Red lines indicate faults along an irregular unconformity surface as recognized from amplitude map co-rendered with coherence. I focus on the north-south fault on the eastern side of the area with our field name of "El-Reno" fault. A vertical EW slice (Figure 2b), normal to El-Reno fault through the 3D seismic amplitude volume shows top and base of the Woodford interval. The El-Reno fault cuts the top of the Hunton Limestone (green horizon) and continues into the Woodford Shale (pink horizon), and giving rise to small throws and rotated layers. The small vertical throw is in contrast to the large dimensions of the El-Reno fault which exceeds 20 mi (Fig. 2b) and with a vertical extent of at least 3000 ft (Fig. 2b).

Several features indicate that the El-Reno fault may be a strike-slip fault. First, it is a vertical fault with several sub-parallel vertical segments (Fig. 2b), typical of strike-slip faults (Dieterich and Smith, 2009; Powers and Jordan, 2010). Second, the small

vertical throw (Fig. 2b) with respect to its large vertical and horizontal dimensions (Fig. 2) strongly suggests that the predominant displacement was in the horizontal direction. Third, the sense of vertical throw varies between different stratigraphic levels. For example, in Fig. 2b at point B the west side is thrown down, whereas at point B' the east block is thrown down. On the other hand, flower structures were not observed along the El-Reno fault. To test the hypothesis that El-Reno fault is a strike-slip fault system, I analyzed the structural features of a strike-slip fault in a clay cake model, and compared the experimental morphology to the 3D seismic attributes maps.




**Figure 1. Geological map and study area (red star) within the Anadarko basin, Oklahoma (Credit: OGS).**

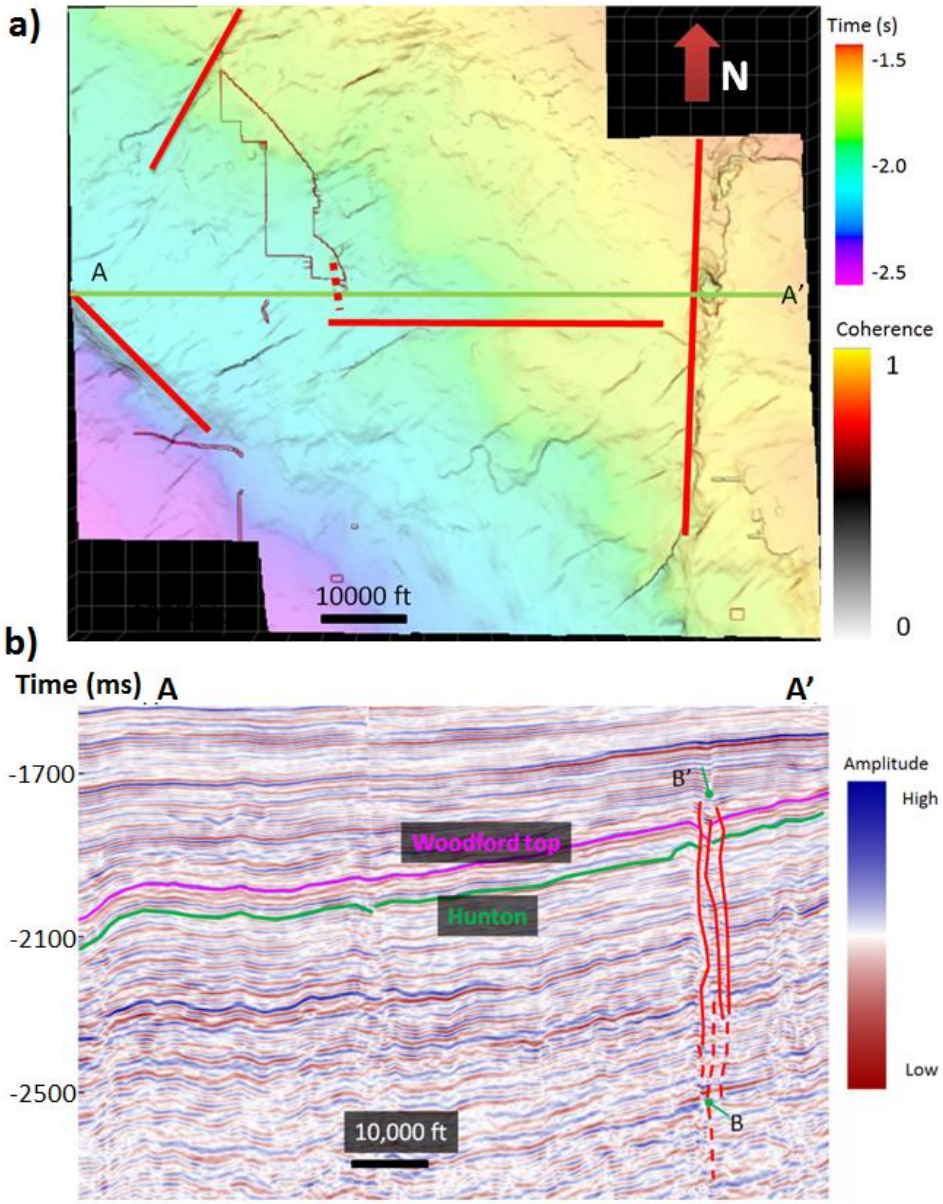


**Figure 2. (a)Time structure of top Woodford co-rendered with horizon slice through coherence. Red lines represent major faults. (b)Vertical slice along AA' through the seismic amplitude volume showing a north-south trending fault zone (in red lines).**

### Strike-slip fault in clay experiments

Clay-cake models have been widely used to study strike-slip faulting (e.g., Riedel, 1929; Freund, 1974; Reches, 1988; Naylor et al., 1986; McClay and Bonora,

2001; Atmaoui et al., 2006). Experimental strike-slip fault zones display a few distinct pattern of subsidiary strike-slip faults (Figure 3a): 1) Synthetic Riedel shears (R) that are small strike-slip fault trending ~15 °relatively to the basement fault; 2) Antithetic Riedel shears (R') striking at ~75 °-90 °to the basement fault with an opposite sense of shear to the R shears; 3) Short-lived splay faults near the tips of Riedel shears; and 4) P shear faults connecting the discontinuous Riedel shears. Additional associated structures are folds (Fig. 3b) and thrust faults (Fig. 3c) oriented ~ 45 °with respect to the main fault, and normal faults oriented ~ 135 °with respect to the main fault (Fig. 3d).

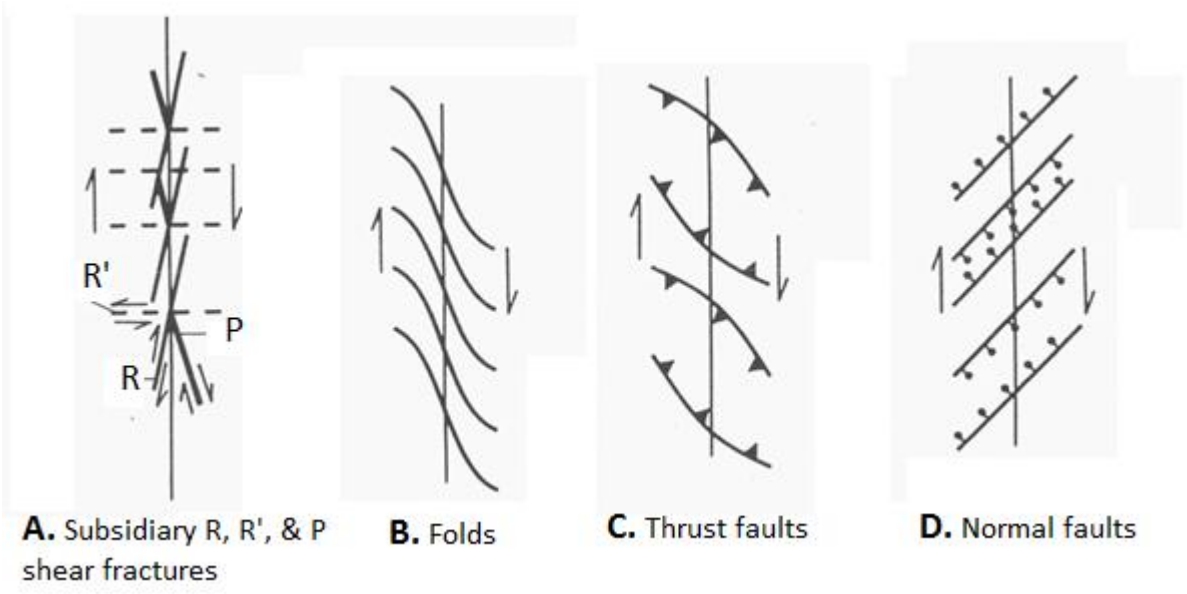


**Figure 3. Mechanical basis for faults/folds/fractures associated with a major strike-slip fault: (a) R and R' faults that developed as Coulomb slip planes; (b) folds along the strike slip fault, which could also be (c) the potential thrust faults; (d) Normal faults developed from Riedel shears (adapted from Naylor et al., 1996; and Reches 1988).**

I do not attempt to run a scale model of El-Reno fault, but rather use the clay model to illustrate the associate structures (Fig. 3) and to monitor their evolution. In the

experiment, the wet clay cake was placed on top of two wooden plates that were moved laterally with respect to each other at a constant slip rate of 0.001 cm/s resulting in total slip of ~1.4 cm (Fig. 4) after 24 minutes. In the experiment of Figure 4a, the clay density was 1.22 g/cm$^3$ (76.2 lb/ft$^3$), the model measured ~ 15 cm long by 15 cm wide (5.9 in) by 5 cm (1.97 in) thick. The cake deformation and its fractures were mapped on photographs, taken every 30 seconds. Figures 4b and c indicates that our experiment generated fault patterns similar to the classical case with dominance of strong secondary Riedel, splay, and P faults (Fig. 3a). I will utilize these results to assist in the seismic interpretation of El-Reno fault.

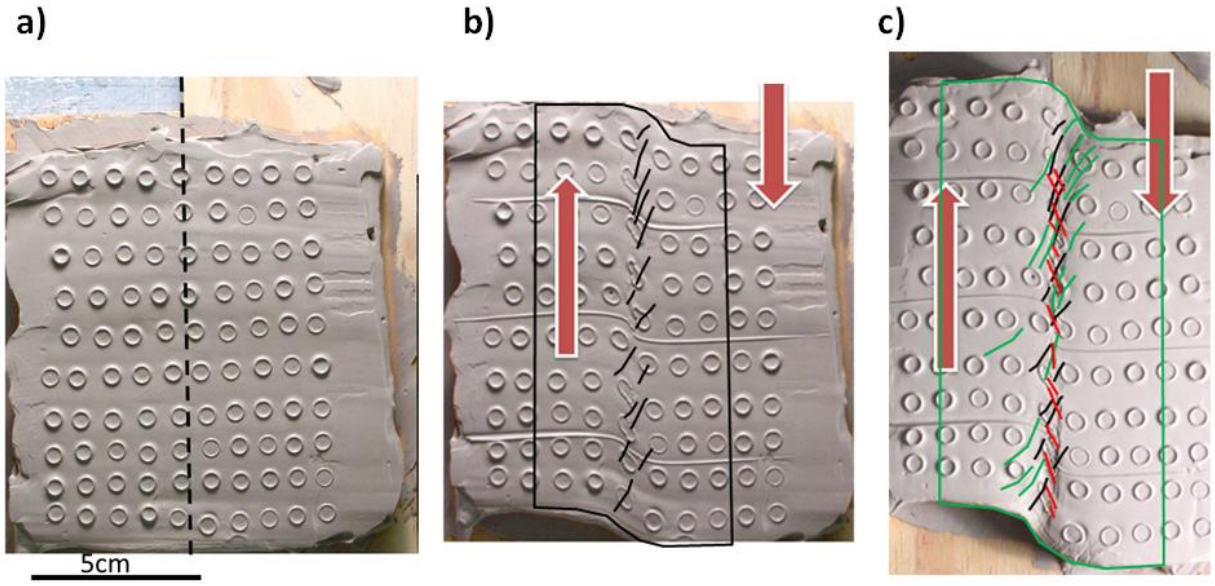


**Figure 4. a) Vertical view of the strike-slip clay experiment. Circles on the undeformed model provide a means of mapping movement and strain. (b) Photograph after 12 min demonstrating initial Riedel shear faults on the top during right-lateral strike-slip with digitized image. (c) Photograph at 24 min demonstrating fault Riedel shears (black lines), splay shears (green lines) and P shears (red lines) on top of the deformed clay.**

## Attribute-based Seismic analyses

In the study area, the Woodford Shale gently dip (<2 ⁰) towards southwest with palaeo-shoreline in the northeast corner and a basin depocenter (Gupta, 2012). The two major faults trend approximately perpendicular to each other (Fig. 1b). I used the 3D seismic survey of the area to prepare coherence, curvature and dip-azimuth that illuminate the features of the El-Reno fault and its structure. Detailed calculation procedures were presented by Marfurt and Rich (2010).

Chopra and Marfurt (2007) define coherence as the energy of the coherent part of seismic traces divided by the average acoustic energy of the input seismic traces. Commonly, this attribute is used to identify lateral discontinuities, such as the faults in Figure 5b, where I traced the interpreted subsidiary faults of El-Reno fault-zone. Visual comparison between the clay modeling (Fig. 5a) and the coherence map (Fig. 5b), suggest a similarity of the fault patterns. Using the clay-model as a guide, I marked the subsurface faults as in Fig. 3a: Major Riedel faults are marked in black, splay faults in green, and P faults (red) connect the Riedel faults. Next, I examine the dip-azimuth pattern along the El-Reno fault; this attribute indicates the orientation of maximum downward dip (Chopra and Marfurt, 2007). In the dip-azimuth map (Fig. 6), the yellow-green bands trending NE-SW, which is sub-parallel to the Riedel faults with respect to the main El-Reno trend. I interpret the pink-red bands as fracture zones associated with P-shear, and the pink zones of dip-azimuth angle as normal faults (Fig. 3d).

Curvature values were extracted and rendered to the horizontal slice (Fig. 7) along the El-Reno fault. The most-positive (red) and most-negative (blue) curvatures exhibit anticlinal and synclinal flexures, respectively (Chopra and Marfurt, 2007). One

striking observation is that the curvature map supports the observed patterns of secondary faults (Fig. 2b) and associated folds (Fig. 2d). It is expected that the extension associated with anticlinal flexures will correlate with local, higher intensity of natural fractures (Sterns, 1978; Guo et al., 2010; Staples, 2011). The synclinal flexures remain to be studied in the future.

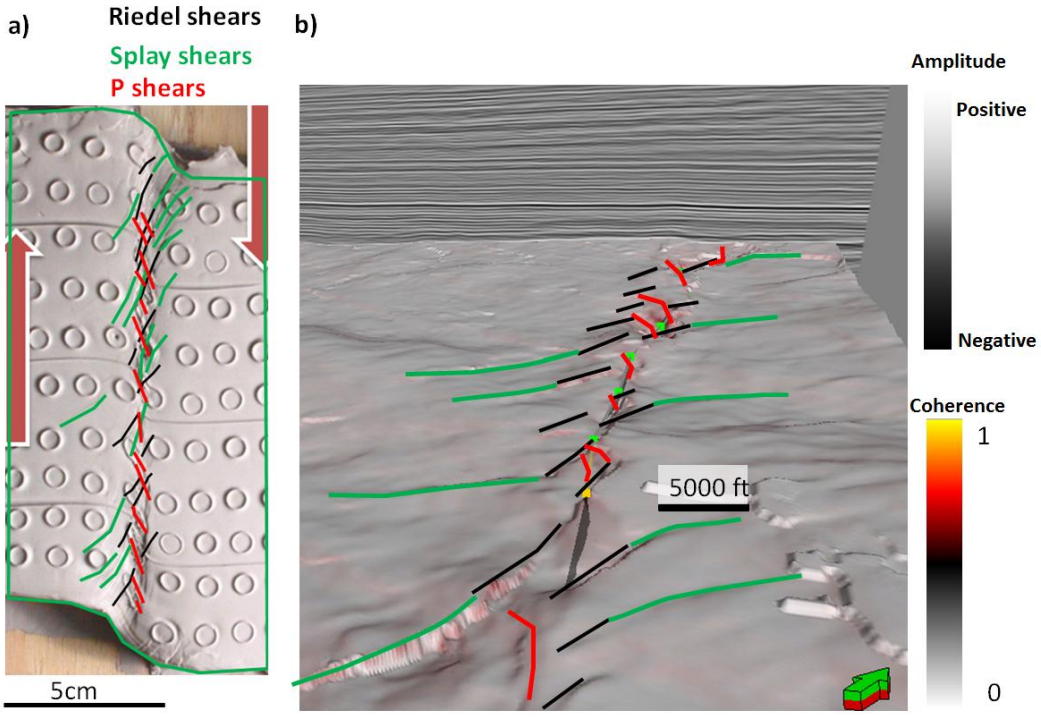


**Figure 5. (a) Photograph from experiment and (b) A display of coherence co-rendered with seismic amplitude on the top Woodford Shale. Black lines indicate potential Riedel faults, the green lines splay faults and red lines P shears.**

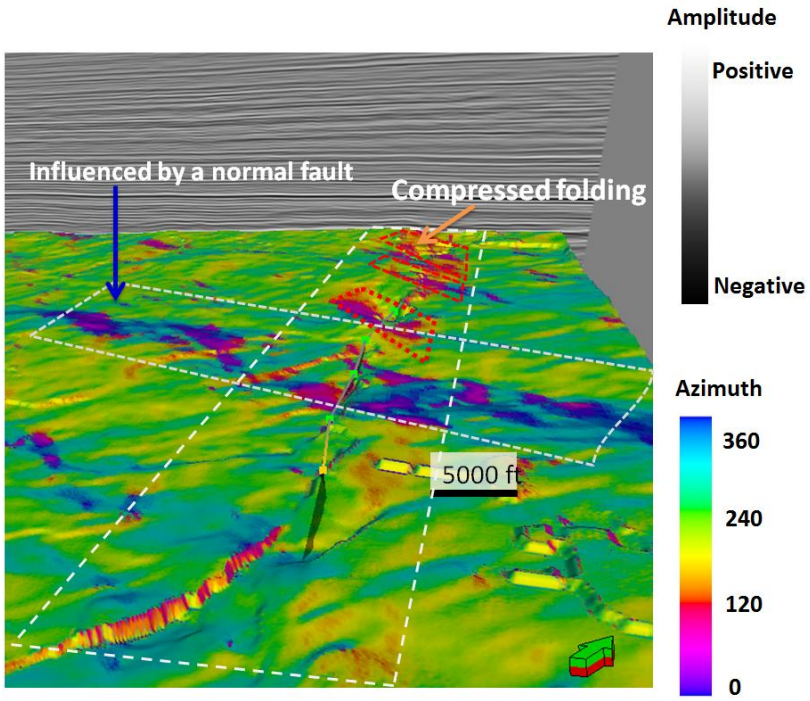


**Figure 6. Dip-azimuth map of the top Woodford. Note the bands of same color within dashed line boxes, indicating same dip-azimuth, revealing potential fracture zones that I interpret to be P shear zones with compressed folds.**

## Fault damage zone

Strike-slip faults may be highly crooked (Wesnousky, 1988) or composed of wide damage zones (Powers and Jordan, 2010). Figure 8 presents a conceptual model of a rough strike slip, such that the slip along the fault generates a heterogeneous stress field over a range comparable to the roughness scale (Fig. 8a; Dieterich and Smith, 2009; Powers and Jordan, 2010). This stress field can be lead to branching of multiple secondary faults. The dip-azimuth and curvature maps show such heterogeneous observations on the top Woodford Shale horizon. In general, the heterogeneities of the rough fault are attenuated away from the fault-zone and across the damage zone (Fig. 8b). To estimate the width of the damage zone, I present a fault-normal profile of coherence by sampling the coherence attribute 'C' with a spacing of ~1 mi along the El-

Reno fault. The amount of damage (8c) decays on the two sides of the fault to the background level (>0.9), and the zone with high 'C' values is interpreted as the damage zone with a width estimate of ~4,000 ft including the secondary faults. This interpretation may suggest that the El-Reno fault zone has a very wide damage zone suggesting large amount of strike-slip displacement.

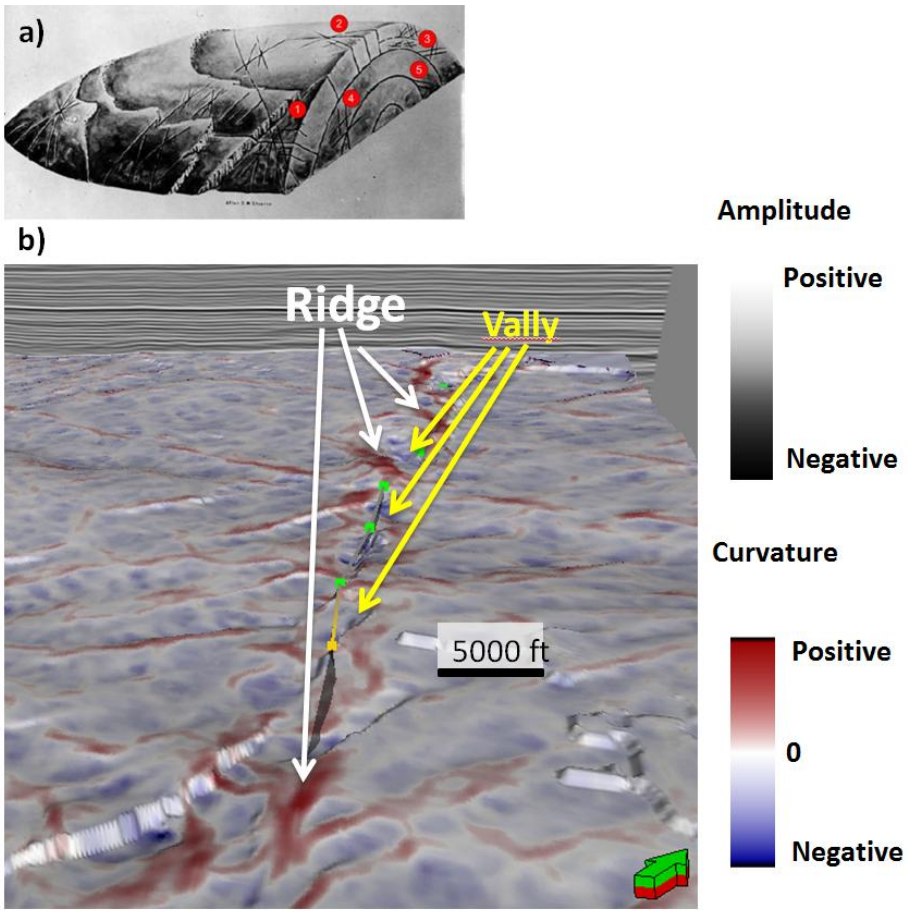


**Figure 7. (a) A schematic diagram showing an anticline folds with fracture systems (after Sterns, 1978) and (b) Curvature on the top of Woodford Shale. Areas with strong curvature (brighter red and blue) correspond to strong flexures, folds, and densely fractures.**

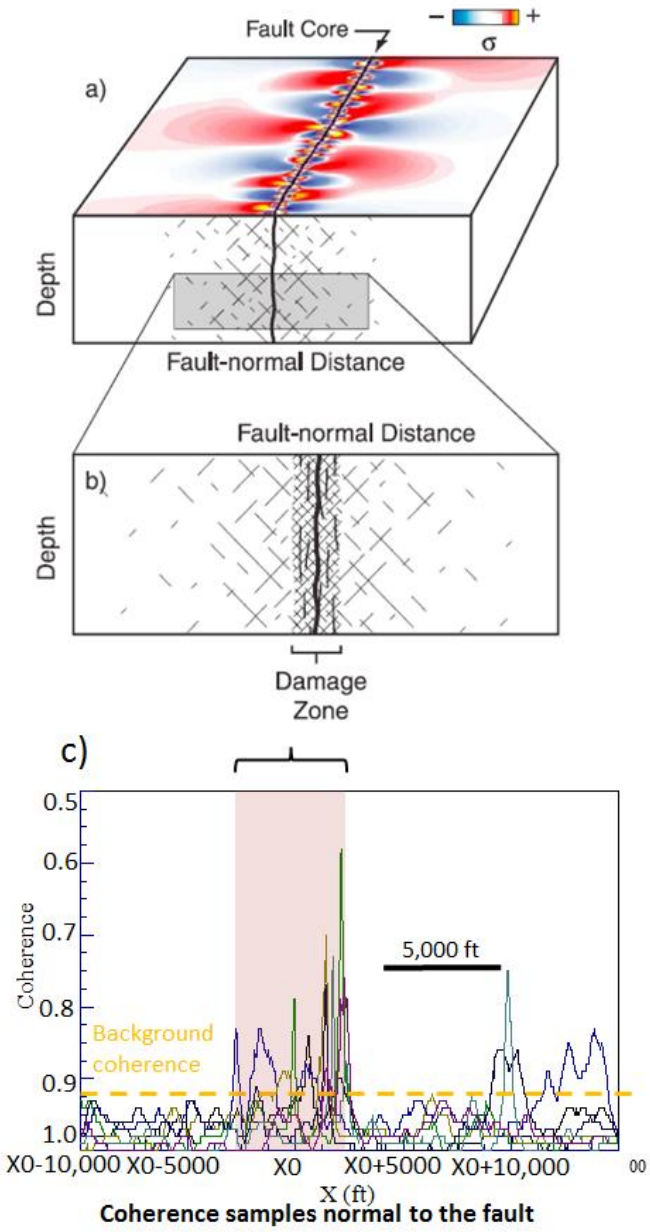


**Figure 8. Schematic representation of the fault model that explains (a) heterogeneous stress field over a scaling region (Dieterich and Smith, 2009; Powers and Jordan, 2010) and (b) damage zone. (c) The illustration of damage zone from the coherence slices perpendicular to the north-south strike slip fault. The zone of high coherence values above background coherence indicates the damage zone.**

## Conclusions

The clay experiment results show that strike slip faults begin with the development of Riedel shears. These are followed by splay shears and finally by P

shears, as well as the formation of a branched faults and folded structures. These features served as the major criteria for proxies of the El-Reno fault that crossed the Woodford Shale in West-Center Oklahoma. I used three attributes (coherence, dip-azimuth, and curvature) to illuminate the fault patterns/features of the El-Reno strike slip fault. The curvature map is found particularly effective indicator of anticlinal folds with expected high fracture intensity (Staples, 2011). I note however that the lithology also play a significant role in control fracture distribution.

While normal and reverse faults are relatively simple to recognize on seismic amplitude and attribute data, strike-slip faults are more difficult to detect because the correlation of horizons across the fault is difficult when the fault slip is large. I found that combining clay models and seismic attributes helps to characterize the structure of a subsurface strike-slip fault.

# References


Abousleiman, Y., S. Hoang, C. Bobko, A. Ortega, and F. J. Ulm (2007), Geomechanics field and laboratory characterization of Woodford shale: The next gas play, SPE Annual Technical Conference and Exibition, Doi:10.2118/110120-MS.

Ampuero, J.-P., J.-P. Vilotte, and F.-J. Sanchez-Sesma (2002), Nucleation of rupture under slip dependent friction law: simple models of fault zone, J. Geophys. Res., 107(B12), 2324, doi:10.1029/2001JB000452.

Ampuero, J.-P., and Y. Ben-Zion (2008), Cracks, pulses and macroscopic asymmetry of dynamical rupture on a biomaterial interface with velocity weakening friction, Geophys. J. Int., doi: 10.1111/j.1365-246X.2008.03736.x.

Andrews, D. J. (1976), Rupture propagation with finite stress in antiplane strain, J. Geophys. Res., 81 (20), 3575-3582.

Andrews, D. J., and Y. Ben-Zion (1997), Wrinkle-like slip pulse on a fault between different materials, J. Geophys. Res., 102, 553–571.

Andrews, D. J. (1985), Dynamic plane-strain shear rupture with a slip-weakening friction law calculated by a boundary integral method, Bull. Seismol. Soc. Am., 75(1), 1-21.

Andrews, D. J. (2004), Rupture models with dynamically-determined breakdown displacement, Seismol. Soc. Am. Bull., 94, 769-775.

Andrews, D. J. (2005), Rupture dynamics with energy loss outside the slip, J. Geophys. Res., Vol. 110, B01307, doi:10.1029/2004JB0033191.

Andrews, D. J., and R. A. Harris (2005), The wrinkle-like slip pulse is not important in earthquake dynamics, Geophys. Res. Lett., 32, L23303, doi:10.1029/2005GL023996.

Anooshehpoor, A. and J. N. Brune (1999), Wrinkle-like Weertman pulse at the interface between two blocks of foam rubber with different velocities, Geophys. Res. Lett., 26, 2025–2028.

Arroyal, R. M. P. (2009), Characterization and origin of fracture patterns in the Woodford Shale in southeastern Oklahoma for application to exploration and development, Master Thesis, The University of Oklahoma, Norman, OK.

Atmaoui, N., N. Kukowski, B. Stöckhert, and D. König (2006), Initiation and development of pull-apart basins with Riedel shear mechanism: Insights from scaled clay experiments: International Journal of Earth Sciences, v. 95, no. 2, p. 225–238, doi:10.1007/s00531-005-0030-1.

Beeler, N. M., T. E. Tullis, and J. D. Weeks (1994), The roles of time and displacement in the evolution effect in rock friction, Geophys. Res. Lett., 21, 1987-1990.

Beeler,N.M. and T.E., Tullis (1996), Self-healing slip pulses in dynamic rupture models due to velocity-dependent strength, Bull. seism. Soc. Am., 86, 1130–1148.

Beeler, N. M., T. E. Tullis, M.L. Blanpied, and J.D. Weeks (1996), Frictional behavior of large displacement experimental faults. J. Geophys. Res., 101, 8697-8715.

Ben-David, O., G. Cohen, and J. Fineberg (2010), The dynamics of the onset of frictional slip, Science, 330:211-214.

Ben-Zion, Y., and J, R. Rice (1997), Dynamic simulations of slip on a smooth fault in an elastic solid. J. Geophys. Res. 102, 17771-17784.

Ben-Zion, Y., and D. J. Andrews (1998), Properties and implications of dynamic rupture along a material interface, Bull. Seismol. Soc. Am., 88,1085–1094.

Ben-Zion, Y., and Z. Shi (2005), Dynamic rupture on a material interface with spontaneous generation of plastic strain in the bulk, Earth Planet. Sci. Lett., 236, 486–496, doi:10.1016/j.epsl.2005.03.025.

Bradra, H. (2011), Field characterization and analog modeling of natural fractures in the Woodford Sahle, southeast Oklahoma, Thesis of University of Oklahoma, Norman, OK.

Brodsky, E.E., and H. Kanamori (2001), Elastohydrodynamic lubrication of faults, J. Geophys. Res., 106(B8), 16,357-16,374.

Brune, J. (1970), Tectonic stress and the spectra of seismic shear waves from earthquakes, J. Geophys. Res, 75(26), 4997-5009.

Busetti, S. (2009), Fracturing in layered reservoir rocks, PhD thesis of University of Oklahoma, Norman, OK.

Byerlee, J.D. (1967), Theory of friction based on brittle fracture: Journal of Applied Physics, v. 38, p. 2928–2934, doi:10.1063/1.1710026.

Cardott, B. (2008), Overview of Woodford gas-shale play of Oklahoma, US: AAPG Annual Convention and Exhibition.

Cardott, B. J., and M. W. Lambert (1982), Thermal maturation by vitrinite reflectance of Woodford Shale, Anadarko basin, Oklahoma: AAPG Bulletin, v. 69, p. 1982–1998.

Chang, J. C., D. A. Lockner, and Z. Reches (2012), Rapid acceleration leads to rapid weakening in earthquake-like laboratory experiments, Science, 338(6103), 101-105.

Chen, X., M. S. Andrew, B. R. Barry, and Z. Reches (2013), Dynamic weakening by nanoscale smoothing during high velocity fault slip, Geology, doi:10.1130/G34169.1.

Chester, F. M., J. S. Chester, D. L. Kirschner, S. E. Schulz, and J. P. Evans (2004), Structure of large-displacement, strike-slip fault zones in the brittle crust, in Rheology and Deformation in the Lithosphere at Continental Margins, edited by G. D. Karner et al., pp. 223–260, Columbia Univ. Press, New York.

Chopra, S., and K. J. Marfurt (2007), Seismic attributes for prospect identification and reservoir characterization, SEG Geophysical Developments Series No. 11, SEG publisher: Houston, USA.

Chopra, S. and K. J. Marfurt (2010), Interpreting fractures through 3-D seismic discontinuity attributes and their visualization: AAPG international convention and exhibition.

Cochard, A., and R. Madariaga (1994), Dynamic faulting under rate-dependent friction, Pure Appl. Geophys., 142, 419– 445.

Comer, J. B. (1992), Potential for producing oil and gas from the Woodford Shale (Devonian-Mississippian) in the southern mid-continent, USA, Medium: X; Size: Pages: 574 p.

Dascalu, C., I. Ionescu, and M. Campillo (2000), Fault finiteness and initiation of dynamic shear instability, Earth Planet. Sci. Lett., 177, 163-176.

Day, S. M. (1982), Three-dimensional finite difference simulation of fault dynamics: rectangular faults with fixed rupture velocity, Bull. Seism. Soc. Am. 72, 705-727.

Day, S., and L. A. Dalguer (2005), Comparison of finite difference and boundary integral solutions to three-dimensional spontaneous rupture, J. Geophys. Res., 110, B12307, doi:10.1029/2005JB003813.

Di Toro, G., D. L. Goldsby, and T.E. Tullis (2004), Friction falls towards zero in quartz rock as slip velocity approaches seismic rates, Nature, 427, 436-439.

Di Toro, G., R. Han, T. Hirose, N. De Paola, S. Nielsen, K. Mizoguchi, F. Ferri, M. Cocco, and T. Shimamato (2011), Fault lubrication during earthquakes, Nature, 471:494-498, doi:10.1038/nature09838.

Dieterich, J. H. (1979), Modeling of rock friction: 1. Experimental results and constitutive equations, J. Geophys. Res., 84, 2161–2168.

Dieterich, J. H. (1981), Constitutive properties of faults with simulated gouge, Geophys. Monograph Am. Geophys. Union 24, 103 –120.

Dieterich, J. H., and D. E. Smith (2009), Nonplanar faults: Mechanics of slip and off-fault damage, Pure Appl. Geophys., 166, 1979-1815, doi:10.1007/s00024-009-0517-y.

Freund, L. B. (1979), The mechanics of dynamic shear crack propagation, J. Geophys. Res. 84, 2199-2209.

Fukuyama, E., and R. Madariaga (1995), Integral equation method for plane crack with arbitrary shape in 3D elastic medium, Bull. Seism. Soc. Am. 85, 614 –628.

Fukuyama, E., and K. Mizoguchi (2009), Constitutive parameters for earthquake rupture dynamics based on high-velocity friction tests with variable slip rate. Int. J. Fract., DOI 10.1007/s10704-009-9417-5.

Geubelle, P.H., and J. R. Rice (1995), A spectral method for three-dimensional elastodynamic fracture problem, J. Mech. Phys. Solids, 43, 1791-1824.

Goldsby, D. L., and T. E. Tullis (2002), Flash heating/melting phenomena for crustal rocks at (nearly) seismic slip rates, SCEC Annual Meeting Proceedings and Abstracts, Palm Springs, California.

Goldsby, D. L., and T. E. Tullis (2011), Flash heating leads to low friction strength of crustal rocks at earthquake slip rates, Science 334(6053), 216-218.

Guo, Y., K. Zhang, and K. J. Marfurt (2010), Seismic attribute illumination of Woodford Shale faults and fractures, Arkoma Basin, OK: 80th Annual International Meeting of the SEG, expanded abstracts 1372-1376.

Gupta, N., S. Sarkar, and K. J. Marfurt (2011), Seismic characterization of the Woodford shale in the Anadarko basin, 81st Annual International Meeting of the SEG, Expanded Abstracts, USA, 1083-1087.

Gupta, N., and K. J. Marfurt (2012), Multi-scale characterization of the Woodford Shale in west-central Oklahoma: From scanning electron microscope to 3D seismic, PhD thesis of University of Oklahoma, Norman, OK.

Harris, R. A. (2004), Numerical simulations of large earthquakes: Dynamic rupture propagation on heterogeneous faults, Pure appl. Geophys., 161, 2171-2181.

Hayward, I.P., I.L. Singer, and L. E. Seitzman (1992), Effect of roughness on the friction of diamond on CVD diamond coatings: Wear, v. 157, p. 215–227, doi:10.1016/0043-1648(92)90063-E.

Heaton, T. H. (1990), Evidence for and implications of self-healing pulses of slip in earthquake rupture, Phys. Earth Planet. Interiors 64, 1-20.

Huang, Y., and J. P. Ampuero (2011), Pulse-like ruptures induced by low-velocity fault zones, J. Geophy. Res., doi:10.1029/2011JB008684.

Ida, Y. (1972), Cohesive force across the tip of a longitudinal shear crack and Griffith's specific surface energy, J. Geophys. Res., 77, 3796-3805.

Ide, S., and M. Takeo (1997), Determination of constitutive relations of fault slip based on seismic analysis, J. Geophys. Res., 102, B12, 27379-27391.

Johnson, K. S. (1988), Geologic evolution of the Anadarko basin, in K. S. Johnson, ed., Anadarko basin Symposium: Circular 90, Oklahoma Geological Survey, p. 3-12.

Johnson, E. (1992), The influence of the lithospheric thickness on bilateral slip, Geophys. J. Int. 101, 151-160.

Kaneko, Y., N. Lapusta, and J.-P Ampuero (2008), Spectral element modeling of spontaneous earthquake rupture on rate and state faults: effect of velocity-

strengthening friction at shallow depths, J. Geophys. Res., 113, B09317, doi:10.1029/2007JB005553.

Kanamori, H. ( 2004), The diversity of the physics of earthquakes. Proc. Japan Acad. Ser. B80. 297-317.

Kanamori, H., and E. E. Brodsky (2004), The physics of earthquakes, Reports on Progress in Physics, 67, 1429 – 1496, doi: 10./1088/0034-4885/67/8/R03.

Kuwano, O., and T. Hatano (2011), Flash weakening is limited by granular dynamics, Geophysical Research Letters, Vol. 38, L17305, doi:10.1029/2011GL048530.

Lachenbruch, A. H. (1980), Frictional heating, fluid pressure, and the resistance to fault motion. J. Geophys. Res. 85, 6249–6272.

Lambert, M. W. (1993), Internal stratigraphy and organic facies of the Devonian-Mississippian Chattanooga (Woodford) Shale in Oklahoma and Kansas: Source rocks in a sequence stratigraphic framework: AAPG Studies in Geology, v. 37, p.163–176.

Lapusta, N., J. R. Rice, Y. Ben-Zion, and G. Zheng (2000), Elastodynamic analysis for slow tectonic loading with spontaneous rupture episodes on faults with rate- and state-dependent friction, J. Geophys. Res., 105: 23765-23789.

Lawn, B. (1993), Fracture of brittle solids, Cambridge, Great Britain: Cambridge University Press.

Liao, Z., and Z. Reches (2012), Modeling dynamic-weakening and dynamic-strengthening of granite fault in high-velocity slip experiments, in S. D'Amico, eds., Earthquake Research and Analysis, Rijeka, Croatia: InTech, 107-125.

Lockner, D. A., and N. M. Beeler (2003), Stress-induced anisotropic poroelasticity response in sandstone, Electronic Proc. 16th ASCE Engin. Mech. Conf., Univ. of Washington, Seattle, WA.

Madariaga, R., K. B. Olsen, and R. J. Archuleta (1998), Modeling dynamic rupture in a 3-D earthquake fault model, Bull. Seismol. Soc. Am., 88, 1182-1197.

Marfurt, K. J., and J. Rich (2010), Beyond curvature – Volumetric estimation of reflector rotation and convergence: 80th Annual International Meeting of the SEG, Expanded Abstracts, 1467-1472.

Marone, C., and B. Kilgore (1993), Scaling of the critical slip distance for seismic faulting with shear strain in fault zone, Nature, 362, 618-621.

Marone, C. (1998), Laboratory-derived friction constitutive laws and their application to seismic faulting, Annu. Rev. Earth Planet. Sci., 26, 643-696.

McClay, K., and M. Bonora (2001), Analog models of restraining stepovers in strike-slip fault Systems: AAPG Bulletin, v. 85, no. 2, p. 233–260.

Mikumo, T., K. B. Olsen, E. Fukuyama, and Y. Yagi (2002). Stress-breakdown time and slip-weakening distance inferred from slip-velocity functions on earthquake faults, Bull. Seism. Soc. Am. 93, 264–282.

Morrisey, J. W., and P. H. Geubelle (1997), A numerical schem for model III dynamic fracture problems, Int. J. Num. Meth. Eng., 43(7), 1181-1196.

Naylor, M.A., G. Mandl, and C. H. K. Supesteun (1986), Fault geometries in basement-induced wrench faulting under different initial stress states, Journal of Structural Geology, 8: 737-752.

Niemeijer, A., G. DiToro, S. Nielsen, and F. Di Felice (2010), Frictional melting of gabbro under extreme experimental conditions of normal stress, acceleration, and sliding velocity, J. Geophys. Res.116, B07404.

Ohnaka, M., Y. Kuwahara , and K. Yamamoto (1987), Constructive relations between dynamic physical parameters near a tip of the propagating slip zone during stick-slip shear failure, Tectonophysics, 144:109-125.

Ohnaka, M., and T. Yamashita (1989), A cohesive zone model for dynamic shear faulting based on experimentally inferred constitutive relation and strong motion source parameters, J. Geophys. Res. 94, 4089-4104.

Ohnaka, M., and L. Shen (1999), Scaling of the shear rupture process from nucleation to dynamic propagation: Implication of geometric irregularity of the rupture surfaces, J. Geophys. Res. 104(B1), 817-844.

Okubo, P. G. (1989), Dynamic rupture modeling with laboratory-derived constitutive relations, J. Geophys. Res. 94, 12321-12335.

Palmer, A. C., and J. R., Rice (1973), The Growth of Slip Surfaces in the Progressive Failure of Over-Consolidated Clay. Proc. Roy. Soc., Lond., A, 332, 527-548.

Perrin, G., J. R. Rice, and G. Zheng (1995), Self-healing slip pulse on a frictional surface, J. Mech. Phys. Solids, 43, 1461-1495.

Paxton, S. T., A. M. Cruse, and A. M. Krystyniak (2006), Detailed fingerprints of global sea-level change revealed in Upper Devonian / Mississippian Woodford Shale of south-central Oklahoma: AAPG Annual Meeting.

Powers, P. M., and T. H. Jordan (2010), Distribution of seismicity across strike-slip faults in California, J. Geophys. Res., 115, B05305, doi: 10.1029/2008JB006234.

Prakash, V. (1995), A pressure-shear plate impact experiment for investigating transient friction, Experimental Mechanics, 35(4), 329-336.

Reches, Z. (1983), Faulting of rocks in three-dimensional strain field, II, Theoretical analysis, Tectonophysics, 95: 133-156.

Reches, Z. (1988), Evolution of fault patterns in clay experiments, Tectonophysics, 145.1, 141-156.

Reches, Z., and D. A. Lockner (2010), Fault weakening and earthquake instability by powder lubrication, Nature, 467(7314), 452-455, doi:10.1038/nature09348.

Rice, J. R. (2005), Heating and weakening of faults during earthquake slip, J. Geophys. Res. 111, ID B05311.

Rice, J. R., and A. L. Ruina (1983), Stability of steady frictional slipping, J. Appl. Mech., 50, 343-349.

Rice, J. R., C. G. Sammis, and R. Parsons (2005), Off-fault secondary failure induced by a dynamic slip-pulse. Bull. Seismol. Soc. Amer., 95(1), 109-134.

Riedel, W. (1929), Zur Mechanik geologischer Brucherscheinungen. Zentralbl. Mineral. Geol. Palaeontol., 1929B: 354-368.

Rojas, O., S. Day, J. Castillo, and L. A. Dalguer (2008), Modelling of rupture propagation using high-order minetic finite differences, Geophys. J. Int., 172, 631-650.

Romina Marisa, P. A. (2009), Characterization and origin of fracture patterns in the Woodford Shale in southeastern Oklahoma for application to exploration and development, MS thesis of University of Oklahoma, Norman, OK.

Rubin, A.M., and D. Gillard (2000), Aftershock asymmetry/rupture directivity among central San Andreas fault microearthquakes, J. Geophys. Res.-solid Earth, 105, 19095–19109.

Rubinstein, S.M., G. Cohen, and J. Fineberg (2004), Detachment fronts and the onset of dynamic friction, Science, 430:1005-1009.

Ruina, A. L. (1983), Slip instability and state variable friction laws, J. Geophys. Res, 88, 10359-10370.

Sammis, C. G., D. A. Lockner, and Z. Reches (2011), The role of adsorbed water on the friction of a layer of submicron particles, Pure and Applied Geophysics, doi: 10.1007/s00024-01-0324-0.

Samuelson, J., D. Elsworth, and C. Marone (2009), Shear-induced dilatancy of fluid-saturated faults: experiment and theory, J. Geophys. Res., 114, B12404, doi: 10.1029/2008JB006273.

Scholz, C. H. (1988), The critical slip distance for seismic faulting, Nature 336, 761 – 763.

Scholz, C. H. (1998), Earthquakes and friction laws, Nature 391, 37-42.

Shimamoto, T., and J. M. Logan (1984), Laboratory friction experiments and natural earthquakes: An argument for long teren tests, Technophysics, 109, 165-175.

Shi, Z., and Y. Ben-Zion (2006), Dynamic rupture on a bimaterial interface governed by slip-weakening friction, Geophys. J. Int., 165, doi:10.1111/j.1365-246X.2006.02853.x.

Slatt., R.M., R. Portas, N. Buckner, Y. Abousleiman, N. M. O'Borien, R. Sierra,P. Philp, A. Miceli-Romero, R. Davis, and T. Wawrzyniec (2010), Outcrop/behind outcrop, multi-scale characterization of the Woodford gas shale, Oklahoma.

Sone, H., and T. Shimamoto (2009), Frictional resistance of faults during accelerating and decelerating earthquake slip, Nature Geoscience, 2, 705 - 708.

Staples, E., K. J. Marfurt, and Z. Reches (2011), Curvature-fracture relations in clay experiments, SEG Expanded Abstract, San Antonio, TX, USA, 1908-1912.

Staples, E. (2011), Subsurface and experimental analyses of fractures and curvature, MS thesis of University of Oklahoma, Norman, OK.

Sterns, D. W. (1978), Faulting and forced folding in the Rocky Mountain foreland, in Matthews, V., Ill, ed., Laramide folding associated with basement block faulting in the western United States: Geological Society of America Memoir 151, p. 1-37.

Tisato, N., G. Di Toro, N. De Rossi, M. Quaresimin, and T. Candela (2012), Experimental investigation of flash weakening in limestone, J. Structural Geology, 38, 183-199.

Tsutsumi, A., and T. Shimamoto (1997), High-velocity frictional properties of gabbro, Geophys. Res. Lett., 24(6), 699-702.

Tullis, T. E. (1996), Rock friction and its implications for earthquake pre- prediction examined via models of Parkfield earthquakes, Proc. Natl.Acad. Sci. USA 93, 3803 –3810.

Waters, G., B. Dean, R. Downie, K. Kerrihard, L. Austbo, and B. McPherson (2009), Simutaneous hydraulic fracturing of adjacent horizontal wells in the Woodford Shale, SPE Hydraulic fracturing Technology Conference, Doi: 10.2118/119635-MS.

Weertman, J. (1980), Unstable slippage across a fault that separates elastic media of different elastic constants, J. Geophys. Res., 85, 1455– 1461.

Wesnousky, S.G. (1988), Seismological and structural evolution of strike-slip faults, Nature 335.

Xu, S., Y. Ben-Zion, and J.-P. Ampuero (2012a), Properties of Inelastic Yielding Zones Generated by In-plane Dynamic Ruptures: I. Model description and basic results. J. Int., 191, 1325–1342, doi: 10.1111/j.1365-246X.2012.05679.x.

Xu, S., Y. Ben-Zion, and J.-P. Ampuero (2012b), Properties of Inelastic Yielding Zones Generated by In-plane Dynamic Ruptures: II. Detailed parameter-space study, Geophys. J. Int., 191, 1343–1360, doi: 10.1111/j.1365-246X.2012.05685.x.

Xu, S., and Y. Ben-Zion (2013), Numerical and theoretical analyses of in-plane dynamic rupture on a frictional interface and off-fault yielding patterns at different scales, Geophys. J. Int., 193, 304-320.

Yuan, F., and V. Prakash (2008), Slip weakening in rocks and analog materials at co-seismic slip rates, J Mech. Phys. Solids 56, 542-560.

Zhao, D., and H. Negishi (1998), The 1995 Kobe earthquake: Seismic image of the source zone and its implications for the rupture nucleation, J. Geophys. Res., 103(B5), 9967-9986.

Zheng, G., and J. R. Rice (1998), Conditions under which velocity-weakening friction allows a self-healing versus a crack-like mode of rupture, Bull. Seismol. Soc. Am., 88, 1466-1483.